

ABSTRACT

VISWANATH, VIDYA. Annealing Polymer Nanocomposite Fibers and Films Via Photothermal Heating: Effects On Overall Crystallinity and Morphology. (Under the direction of Dr. Russell E. Gorga and Dr. Laura I. Clarke).

Metal nanoparticles embedded within polymeric systems can act as localized heat sources, facilitating in situ polymer processing. When irradiated with light resonant with the nanoparticle's surface plasmon resonance (SPR), a non-equilibrium electron distribution is generated which rapidly transfers energy into the surrounding medium, resulting in a temperature increase in the immediate region around the particle. This work compares the utility of such photothermal heating versus traditional heating in two different polymeric media i.e. gold nanospheres/poly (ethylene oxide) (AuNP:PEO) nanocomposite films and electrospun nanofibers. Subsequently, a brief study on the usage of gold nanorods (AuNR) to anneal polymeric nanofibers and films has also been presented.

Effect of annealing by conventional and photothermal methods has been studied for AuNP:PEO films crystallized from solution and the melt, which have been annealed at average sample temperatures above the glass transition and below the melting point. For all temperatures, photothermally annealed samples reached maximum crystallinity and maximum spherulite size at shorter annealing times. Percentage crystallinity change under conventional annealing was analyzed using time-temperature superposition (TTS). Comparison of the TTS data with results from photothermal experiments enabled determination of an "effective dynamic temperature" achieved under photothermal heating which is significantly higher than the average sample temperature. Thus, the heterogeneous temperature distribution created when annealing with the plasmon-mediated photothermal

effect represents a unique tool to achieve processing outcomes that are not accessible via traditional annealing.

In addition, the effect of annealing AuNP:PEO electrospun nanofibrous composites via conventional and photothermal annealing has also been studied. From the studies, it was observed that not only is the maximum crystallinity achieved more quickly when the nanocomposite was heated photothermally, but also higher values of maximum crystallinity were obtained as compared to those achieved by conventional annealing. It is also important to note that while the increase in crystallinity in the nanocomposite systems annealed photothermally was achieved, the complex nanostructured morphology of the nanofibrous mat was maintained. Evaluation of mechanical properties of annealed samples also showed that samples annealed by photothermal heating possessed higher moduli than those annealed conventionally, clearly indicating the efficacy of photothermal annealing in improving crystal structure (crystallinity) and inter fiber bonding. Time temperature superposition analysis was carried out to study crystallinity trends for conventional and photothermal annealing data. As in nanocomposite films, effective dynamic temperature attained by photothermally annealed fibers was found to be higher than those subjected to conventional annealing.

Finally, the effect of annealing AuNR:PEO nanocomposite films and fibers with gold nanorods has also been studied. Photothermally annealed films were found to reach higher crystallinities over shorter annealing times as compared to conventionally annealed samples, although the enhancement in crystallinity was not as pronounced as that for samples

containing nanospheres. Similar trends observed in AuNR:PEO nanocomposite nanofibers have also been reported.

© Copyright 2013 Vidya Viswanath

All Rights Reserved

Annealing Polymer Nanocomposite Fibers and Films Via Photothermal Heating: Effects On
Overall Crystallinity and Morphology.

by
Vidya Viswanath

A dissertation submitted to the Graduate Faculty of
North Carolina State University
in partial fulfillment of the
requirements for the degree of
Doctor of Philosophy

Fiber and Polymer Science

Raleigh, North Carolina

2013

APPROVED BY:

Dr. Russell E. Gorga
Committee Co-Chair

Dr. Laura I. Clarke
Committee Co-Chair

Dr. Jason Bochinski
Committee Member

Dr. Saad Khan
Committee Member

DEDICATION

To the Almighty, for bestowing me with all the strength to complete this endeavor, my parents for their relentless support and love and my dearest grandmother *Paati*

BIOGRAPHY

Vidya Viswanath was born in Mumbai, India. She completed her Bachelor of Technology, in Textile Technology from Veermata Jijabai Technological Institute (V.J.T.I) , Mumbai in 2007. After completing her under graduation, she obtained professional experience as a Research Engineer at BASF India Limited, Mumbai. She came to the United States in the Fall of 2008 to pursue a Master of Science degree in Textile Engineering at North Carolina State University under the direction of Dr. Richard Kotek . Her interest in nanomaterials led her to pursue her doctoral research in the Fiber and Polymer Science department at NCSU under the direction of Dr. Russell Gorga and Dr. Laura Clarke. After her doctoral studies, Vidya plans to actively seek opportunities in the field of polymer/nanomaterials research.

ACKNOWLEDGMENTS

Firstly, I would like to thank Dr. Gorga and Dr. Clarke for giving me this opportunity to pursue this research project as a doctoral student. Dr. Gorga has been a superb mentor; positively critical while correcting my mistakes and at the same time encouraging and supporting. His style of explaining abstruse technical concepts in a simple and lucid way has clarified many of my fundamentals and I owe my interest in nanomaterials almost exclusively to him. Working with Dr. Clarke has been very inspiring and she has instilled a sense of discipline in me. During the unpredictable times of research when things do not go as per expectations, she has steadily motivated the research team and provided brilliant alternative methods, which ultimately led to success. Next, I would like to thank Dr. Bochinski for his valuable inputs and guidance during our weekly meetings. Special thanks to Dr. Saad Khan for agreeing to be on this committee.

I would like to thank Dr. Rust for his support and giving me an opportunity to assist in the teaching of graduate level courses. This project would have been incomplete without the help of Somsubhra Maity, a doctoral student with the Clarke-Bochinski team in the Physics department. I am grateful to Birgit Andersen, Judy Elson, Hai Bui, Roberto Garcia, for their help in sample characterization.

Clichéd as it might sound, the 5.5 long years at NCSU have been a roller coaster ride with many ups and downs. This journey would not have been possible without the presence of some great people. The list is endless and I am thankful to each and every person who helped

me learn and mature as an individual. However, a few guardian angels do deserve a special mention- Rupesh Nawalakhe, Dhananjay Dandekar and Mandar Dombé. They have helped me maintain my calmness during the testing times, been pillars of strength and helped bring a smile (more often a laugh!) on my face. Special thanks to the “CC Gang” for the fun filled evenings of tea and wonderful conversations and outings. I have been fortunate to have some very superb roommates with whom I share a very special bonding. Namrata, Shruti and Apurva, I do owe some very good moments of my life to you. I am forever grateful for the yummy dinners that have awaited me on days when I have drearily walked back home late and the wonderful dinner conversations that have cheered me up. Special thanks to Zubin and Rohit, who have accompanied me on contemplative walks around campus and my dear friend Georgy who has always lifted my spirits with his wonderful musical notes and his cheerful and caring personality.

I am indebted to my parents for their constant support and motivation, encouraging me to excel. My mom has been the source of my strength and has struggled to make me the person I am today. My dad has been a great friend, mentor and a guide who has taught me to be bold and ambitious. Thanks to my uncles “RKK” and S. Sriram, cousin Sharada and aunty Suguna for their unconditional love and support. And finally, a big thank you to my dearest granny “Paati” - a tough, no-nonsense, intelligent, tech savvy lady who has been a great source of inspiration. More than anything, she has pampered me the most, sided me in my pranks and I dedicate this doctoral dissertation to her, in memory of the wonderful days I have spent with her listening to her stories and the many more days of anecdote narrations to come!

TABLE OF CONTENTS

LIST OF FIGURES	xi
LIST OF TABLES	x
CHAPTER 1: INTRODUCTION	1
CHAPTER 2: BACKGROUND	6
2. 1. <i>STRUCTURAL AND MECHANICAL PROPERTIES OF FIBROUS STRUCTURES:</i>	7
2.1. 1. CONVENTIONAL FIBROUS STRUCTURES.....	7
2.1.1. 1. <i>Introduction</i>	7
2.1.1. 2. <i>Structural models for fiber</i>	7
2.1.1. 3. <i>Effect of fiber structure on mechanical properties</i>	15
2.1. 2 ELECTROSPUN NANOFIBROUS STRUCTURES	20
2.1.2. 1. <i>Introduction</i>	20
2.1.2. 2 <i>Electrospinning process</i>	21
2.1.2. 3 <i>Morphology of electrospun nanofibers</i>	23
2.1.2. 4 <i>Structural properties of nanofibers and their effects on mechanical properties</i>	27
2. 2 <i>NANOCOMPOSITE MATERIALS</i>	31
2.2. 1 Introduction.....	31
2.2. 2 Different types of nanoparticles.....	32

2.2. 3 Structural properties of nanocomposites: Role of nanofillers.....	34
2.2. 4 Effect of structural properties of nanocomposites on mechanical properties	37
2. 3 <i>POST PROCESSING: CONVENTIONAL ANNEALING</i>	43
2.3. 1 Annealing effects on crystallinity in bulk polymers	43
2.3. 2 Effect of annealing on conventional structures	44
2.3. 3 Effect of annealing on electrospun structures	49
2. 4 <i>POST PROCESSING PHOTOTHERMAL ANNEALING</i>	56
2.4. 1 Surface Plasmon Resonance (SPR) mediated photothermal annealing.....	56
2.4. 2 Previous work involving the photothermal effect of gold nanoparticles.....	60
CHAPTER 3: RESEARCH OBJECTIVES.....	68
CHAPTER 4: THERMAL ANNEALING OF POLYMER NANOCOMPOSITES VIA PHOTOTHERMAL HEATING: EFFECTS ON CRYSTALLINITY AND SPHERULITE MORPHOLOGY	72
4. 1 Introduction	74
4. 2 Experimental	78
4.2. 1 <i>Polymer nanocomposite fabrication</i>	78
4.2. 2 <i>Annealing methods and temperature measurement</i>	80
4.2. 3 <i>Sample characterization</i>	85
4. 3 Results and discussion.....	87
4.3. 1 <i>Effect of presence of nanoparticles and a brief background</i>	87
4.3. 2 <i>Annealing of solution crystallized films</i>	89

4.3. 3 Annealing of melt-crystallized films	98
4.3. 4 <i>Time temperature superposition</i>	103
4. 4 Conclusion.....	111

CHAPTER 5 : ENHANCED MAXIMUM CRYSTALLINITY AND MECHANICAL
MODULUS OF POLYMER NANOFIBERS WITHOUT LOSS OF NANOFIBROUS

MORPHOLOGY VIA HETEROGENEOUS PHOTOTHERMAL ANNEALING	113
5. 1 Introduction	114
5. 2 Experimental	118
5.2. 1 Metal nanoparticle synthesis.....	118
5.2. 2 Nanocomposite mat fabrication	118
5.2. 3 Annealing methods and temperature measurement	119
5.2. 4 Sample characterization.....	121
5. 3 Results and Discussion.....	123
5.3. 1 Increased crystallinity without compromising nanofibrous morphology	123
5.3. 2. Crystal structure and morphology.....	128
5.3. 3 Mechanical properties.....	130
5.3. 4 Time-temperature superposition	132
5.3. 5 Annealing in nanocomposite films vs. nanofibers.....	137

CHAPTER 6 : ANNEALING OF POLYMER NANOCOMPOSITE FILMS AND FIBERS
BY PHOTOTHERMAL HEATING OF GOLD NANORODS

6. 1: AuNR:PEO nanocomposite films:.....	142
--	-----

6. 2 : AuNR: PEO nanofibrous composites:	150
CHAPTER 7 : CONCLUSIONS AND RECOMMENDATIONS FOR FUTURE WORK	155
7. 1: Conclusions:	156
7. 2 : Recommendations for future work:.....	157

LIST OF TABLES

Table 2. 1 Effect of various parameters on electrospun fiber morphology	26
Table 4. 1 Annealing time to maximum crystallinity and to obtain largest spherulites (minimum spherulite density) in solution cast films for different annealing temperatures using conventional or photothermal annealing	98
Table 4. 2 Annealing time to maximum crystallinity and to obtain largest spherulites (minimum spherulite density) in films crystallized from the melt at different annealing temperatures using conventional and photothermal annealing.....	102
Table 5. 1 Average crystal size and FWHM from WAXD Patterns of As-Spun and annealed AuNP:PEO nanofibers at 40 and 60°C for 180 and 30 minutes respectively	130
Table 5. 2 Effective activation energy (average barrier height) in fibers and films annealed under conventional and photothermal heating conditions.....	139

LIST OF FIGURES

Figure 1.1: Annealing by photothermal heating	2
Figure 2. 1: Structural models for a fiber	10
Figure 2. 2: Electron micrograph of a spherulite.	11
Figure 2. 3: Schematic for (a) Peterlin model, (b) Barham and Arridge model	13
Figure 2. 4: Effect of molecular weight on mechanical strength of a polymer	16
Figure 2. 5: Schematic of a typical electrospinning set up; inset random morphology of an electrospun nanofiber mat	22
Figure 2. 6: AFM phase images showing the surface morphologies of PCL nanofibers with a diameter of (a) 150 nm and (b) 450 nm.	28
Figure 2. 7: Stress–strain curves obtained from tensile tests performed on electrospun PCL and non-spun PCL samples	30
Figure 2. 8: Schematic illustration of mechanical deformation processes of the electrospun PMMA nanocomposite with 10 weight % of SiO ₂ under uniaxial tensile load	38
Figure 2. 9: Relative modulus (E/E _m) vs. filler content for PU reinforced with pristine SWNT , functionalised SWNT and organoclay nanoparticles. ¹⁵¹	41
Figure 2. 10: Polarizing optical micrographs of a PET film of 100 μm thickness, melt- crystallized at 1 Kmin ⁻¹ (top, left), or quenched in ice water (top, right). The bottom images show the structure after additional annealing at 473 K for 60 min. The scaling bar represents a distance of 20 μm ¹⁶⁷	46
Figure 2. 11: Stress-strain curves for samples heat set for 1 min at 100 o C, 160 o C, and 200°C and for control sample (FA, free-annealed; TA, taut-annealed) ¹⁶⁵	48

Figure 2. 12: Phase image of electrospun PLLA nanofiber (as-spun nanofiber) and (b) annealed nanofiber ¹⁷²	51
Figure 2. 13: Scanning electron microscopy (SEM) images of electrospun PEI nanofibers after thermal treatment at (a) 80 °C, (b) 150 °C, (c) 220 °C, (d) 240 °C ¹⁶⁸	52
Figure 2. 14: Mechanical property comparison between the as-prepared electrospun PLA10GA90 membrane with that annealed at 90 °C for 20 min under a strain of 450%. ¹⁷³	54
Figure 2. 15: Schematic of plasmon oscillation for a sphere, showing the displacement of the conduction electron charge cloud relative to the nuclei. ¹⁸⁸	57
Figure 2. 16: Size, shape, and composition dependence of the surface Plasmon absorption spectrum of plasmonic gold nanostructures. (a) Nanospheres of different sizes; (b) nanorods of different aspect ratios ¹⁹²	59
Figure 2. 17: The antibody-functionalized polymer capsule (a) binds to the target (Micrococcus lysodeikticus), and application of laser light causes the gold nanoparticles in the shell of the capsule to heat up (b), bursting the container and releasing the therapeutic ²⁰⁵	62
Figure 2. 18: Optically triggered shape recovery of an AuNP-loaded XbOCL film at room temperature (laser at 532 nm, 1.1 W cm ²): photographs showing a fast untwisting upon scanning of the laser spot (3 mm) along the film. ⁴	64
Figure 2. 19: SEM images of the effect of continuous 532 nm light irradiation on AuN1 þ PEO nanofibrous mats (0.15% volume fraction AuN1 batch #1). ¹	66

Figure 4. 1:(a) Extinction spectrum of the nanocomposite film (left axis) and the gold nanoparticles (13 wt %) in aqueous solution (right axis), where the broad peak is the spectral location of the surface plasmon resonance (SPR). The vertical dotted line indicates wavelength of the photothermal heating laser. (b) TEM image of neat gold nanoparticles. 79

Figure 4. 2: Schematic of (a) conventional and (b) photothermal annealing methods. Magnified diagrams of the nanocomposite sample are shown, schematically showing with a gold nanoparticle remaining inactive in conventionally annealed, uniformly heated samples, and a acting as nanoscale-heaters due to SPR-resonant laser exposure in the photothermally annealed samples. 81

Figure 4. 3: Identical heating and cooling curves (measured via perylene thermometry) for the samples during photothermal or conventional annealing for 15 minute anneal at a temperature of 50 °C..... 83

Figure 4. 4: Full emission spectrum of embedded perylene at 25 °C; vertical dashed lines indicate spectral locations of the peak and trough used for temperature measurement. Inset: Ratio of perylene emission intensity under conventional heating enables calibration of the fluorescence-temperature relationship. 84

Figure 4. 5: Sample crystallinity measured by DSC as a function of annealing time at 50 °C (i.e., at $\sim T_m - 15$ °C) for films of PEO doped with 1.6 wt % of gold nanospheres annealed via photothermal (open diamonds) or conventional (grey squares) methods. The control is an untreated sample as fabricated. (b) Spherulite

density (number of spherulites per unit volume) as a function of annealing time.	90
Figure 4. 6: Cross-polarized optical images of (a) as spun AuNP:PEO films; after conventional annealing for (b) 22 and (c) 75 minutes; and after photothermal annealing for (d) 22 and (e) 75 minutes at 50 °C.	91
Figure 4. 7:(a) Crystallinity and (b) spherulite density as a function of annealing duration for AuNP:PEO films post-processed via conventional and photothermal heating at 60 °C.....	93
Figure 4. 8: Cross-polarized optical images of the AuNP:PEO films after annealing at 60 °C for 4, 8, and 30 minutes conventionally (a), (b), (c) and photothermally (d), (e), (f), respectively.	94
Figure 4. 9: Cross-polarized optical images of the AuNP:PEO films after photothermal annealing at 60 °C for (a) 8 minutes, (b) 22 minutes, and (c) 30 minutes reveal the transition from spherulitic to hedritic morphology.	96
Figure 4. 10:Cross-polarized optical images of (a) melt-crystallized AuNP:PEO film after conventional annealing at 60 °C for 4, 8, and 30 minutes conventionally (b), (c), (d) and photothermally (e), (f), (g), respectively.....	99
Figure 4. 11: Crystallinity and (b) Spherulite density as a function of annealing time for AuNP: PEO melt-crystallized films annealed by conventional and photothermal heating at 60 °C. Quantitative analysis was not performed for conditions where spherulite boundaries were not discernible due to morphology changes (e.g., such as the transformation to a hedritic structure) (see Figure 10g).	101

Figure 4. 12: Logarithm of shift factor as a function of reciprocal temperature for films crystallized from (a) solution and (b) the melt for conventional or photothermal annealing. The solid lines show a linear regression through the conventional annealing data..... 106

Figure 4. 13: Effective dynamic temperature for AuNP: PEO films crystallized from either solution or melt and annealed at the average temperature. 107

Figure 4. 14: Time to reach the maximum crystallinity (t_{max}) as a function of average annealing temperature as determined by DSC for each annealing time at each temperature. 110

Figure 5. 1. SEM images images of (a) untreated AuNR:PEO nanofibers; and at a crystallinity percent of ~70% after annealing at 50 °C for (b) 90 minutes conventionally, (c) 30 minutes by photothermal annealing (fan cooled) , (d) 8 minutes by photothermal annealing with natural cooling ; (e) Crystallinity as a function of annealing duration (minutes) at 50 °C..... 123

Figure 5. 2 SEM images images of (a) untreated AuNR:PEO nanofibers; and at a crystallinity percent of ~70% after annealing at 60 °C for (b) 8 minutes conventionally, (c) 4 minutes by photothermal annealing (fan cooled) , (d) 2 minutes by photothermal annealing with natural cooling ; (e) Crystallinity as a function of annealing duration (minutes) at 60 °C..... 126

Figure 5. 3 SEM images images of (a) untreated AuNR:PEO nanofibers; and at a crystallinity percent of ~70% after annealing at 60 °C for (b) 600 minutes

conventionally, (c) 200 minutes by photothermal annealing (fan cooled) , (d) 75 minutes by photothermal annealing with natural cooling ; (e) Crystallinity as a function of annealing duration (minutes) at 40 °C..... 127

Figure 5. 4 AFM images of (a)untreated AuNP:PEO nanofibers, with arrow indicating row nucleated structure; (b) AuNP:PEO nanofibers annealed by photothermal annealing at 60 °C for 60 minutes with arrow indicating the annealing induced merging of adjacent lamellae.. 129

Figure 5. 5 Tensile modulus of AuNP:PEO nanofibers annealed by conventional heating, photothermal heating (fan cooled) and photothermal heating (natural cooled) at (a) 40 °C and (b)60 °C..... 132

Figure 5. 6 Logarithm of shift factor as a function of reciprocal temperature for nanofibers treated with conventional or (a)photothermal annealing with fan cooling and (b) photothermal annealing with natural cooling . The solid lines show a linear regression through the conventional annealing data. 134

Figure 5. 7 Effective dynamic temperature for AuNP: PEO nanofibers annealed at average temperature..... 136

Figure 6. 1. Extinction spectra of CTAB capped gold nanorods in water; Inset showing the gold nanorods in electrospun nanofibers. 142

Figure 6. 2 Crystallinity as a function of annealing duration for AuNR:PEO nanocomposite films post-processed via conventional and photothermal heating at 60 °C..... 144

Figure 6. 3. Cross-polarized optical images of (a) solution crystallized AuNR:PEO film after conventional annealing at 60 °C for 2, 4, 8, 15 and 30 minutes conventionally (b), (c), (d), (e), (f) and photothermally (g), (h), (i), (j), (k) respectively. 145

Figure 6. 4. Crystallinity as a function of annealing duration for AuNR:PEO nanocomposite films post-processed via conventional and photothermal heating at 50 °C. 146

Figure 6. 5. Cross-polarized optical images of (a) solution crystallized AuNR:PEO film after conventional annealing at 50 °C for 4, 15, 30, 45, 75 and 60 minutes conventionally (b), (c), (d), (e), (f) and photothermally (g), (h), (i), (j), (k) respectively. 146

Figure 6. 6. Crystallinity as a function of annealing duration for AuNR:PEO nanocomposite films post-processed via conventional and photothermal heating at 40 °C. 148

Figure 6. 7. Cross-polarized optical images of (a) solution crystallized AuNR:PEO film after conventional annealing at 40 °C conventionally and photothermally. 149

Figure 6. 8. SEM images images of (a) AuNR:PEO nanofibers; and after annealing at 60 °C for 4, 8, 15,30 and 60 minutes conventionally (b), (c), (d), (e), (f) and photothermally with fan cooling (g), (h), (i), (j) and (k)..... 152

Figure 6. 9. Crystallinity as a function of annealing duration for AuNR:PEO nanofibers post-processed via conventional and photothermal heating at 60 °C.. 153

CHAPTER 1: INTRODUCTION

1. INTRODUCTION

In this research, we investigate the use of the photothermal effect of metal nanoparticles as a tool for processing of polymeric nanofibers and films. The photothermal effect of gold nanoparticles refers to Surface Plasmon Resonance (SPR) mediated heating, wherein the incident light energy is converted to heat (phonons) as shown in Figure 1.1. The incident light absorbed by the nanoparticle generates a non-equilibrium electron distribution that decays by electron scattering ¹. Link *et al* showed that the light induced excitation of metal nanostructures resulted in the formation of a heated electron gas that cools rapidly by exchanging energy with the nanoparticle lattice ². Subsequently, phonon-phonon interactions cause the nanoparticle lattice to exchange its energy with the surrounding medium. This fast energy conversion and dissipation is responsible for the heating of the local environment.

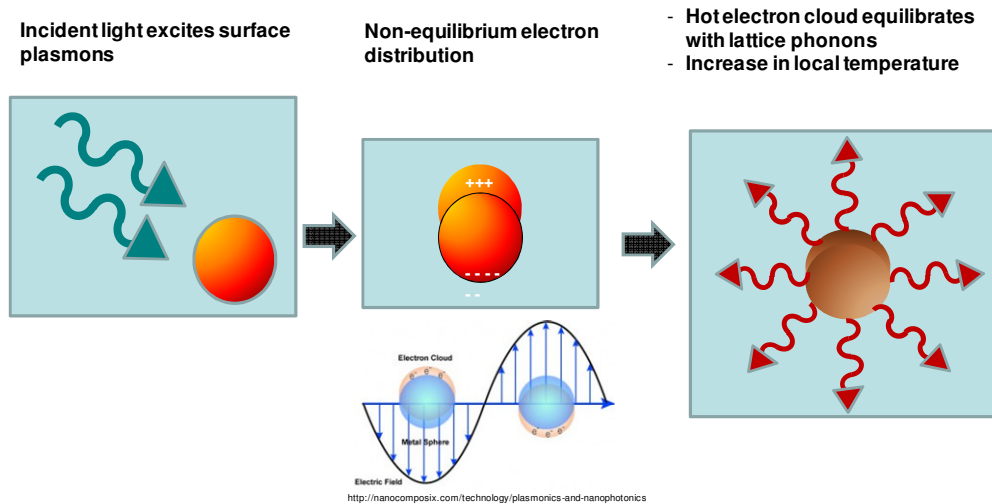


Figure 1. 1: Annealing by photothermal heating.

While this fundamental property of metal nanoparticles has been previously explored scientifically and utilized in aqueous environments for biomedical application, few reports discuss how the photothermal effect might be usefully applied to a solid medium or for materials processing. It is only recently that the application of the photothermal effect in solid materials has been explored, primarily in the field of controlled drug delivery. Studies have been carried out that exploit the photothermal effect of nanoparticles to activate shape memory polymeric (SMP) devices.^{3, 4, 5, 6}

The utilization of gold nanoparticles as heat sources within polymeric materials offers unique advantages due to their spatial and wavelength specificity. In a solid medium, relatively lower losses of phonon energy occur as compared to a liquid medium where heat losses occur in all directions by conduction and convection. The spatial specificity of the process enables heat to be generated from the inside of the polymeric medium (inside to outside approach) as opposed to conventional methods of heating where the outer surface of the sample is the first to heat (outside to inside). Thus in-situ processing of polymeric materials can take place at the nanoscale.

In the current research, we describe the effect of post processing annealing in polymer nanocomposite systems. Chapter 2 gives a brief overview of structural morphology in conventional and nanofibrous polymeric materials and the effect of post processing conventional and photothermal annealing on the morphology, crystallinity and mechanical properties of these polymer composite systems. Based on the review of pertinent literature, Chapter 3 enlists the research objectives of this study. Chapter 4 describes the polymer

nanocomposite films with gold nanoparticles have been subjected to two different types of annealing methods i.e. conventional and photothermal annealing. The effect of these two annealing methods, at different annealing temperatures and times, on the morphology and crystallinity of nanocomposite systems has been investigated. These results demonstrate that while annealing at the same average temperature, a much faster increase in crystallinity is achieved when heating photothermally than traditionally. Further, by using time-temperature superposition, the "effective dynamic" temperature of the photothermally annealed samples has been determined. The "effective dynamic" temperature achieved during photothermal annealing was found to be significantly greater than the average temperature achieved by traditional annealing. This has special significance at annealing temperatures closer to melt temperature wherein photothermal annealing was found to demonstrate effective temperatures significantly higher than the melting point, enabling high temperature dynamics within the sample (a fast increase in crystallinity) without bulk melting (which would occur in traditional annealing where the entire sample experienced this temperature).

Thus the advantages of efficient localized heating for processing nanocomposites by using gold nanoparticles as localized heat sources has been demonstrated. Further, photothermal heating can be used to enable thermal processing in other nanofibrous systems due to their spatial specificity (e.g. selective cross linking within fiber interior leaving the outer layer untreated) thereby enabling different morphologies with uniquely functional mechanical

properties to be obtained. Novel applications in the field of nano actuation can be realized by utilizing the photothermal effect to thermally actuate shape memory polymers.

CHAPTER 2: BACKGROUND

2. BACKGROUND

2.1. STRUCTURAL AND MECHANICAL PROPERTIES OF FIBROUS STRUCTURES:

This section aims to provide an overview of the structural morphology of fibrous materials, both conventional as well as nanofibrous structures. Structural morphologies will be discussed from a molecular level and the effect of morphology on macroscopic behavior, specifically mechanical properties, will be addressed.

2.1.1. CONVENTIONAL FIBROUS STRUCTURES

2.1.1.1. Introduction

For most applications that make use of fibrous structures- textiles, nonwovens, composites, etc. - the mechanical, thermal and optical properties are of paramount importance. An accurate prediction of these involves an in-depth understanding of the polymer systems that constitute these fibrous structures. Molecular conformations, chemical compositions, molecular orientations that affect the physical nature of a polymer need to be taken into consideration and understood. The first chapter of this review will thus be devoted to understanding this important structure-property relationship of fibrous systems.

2.1.1.2. Structural models for fiber

Polymeric fibers are characterized by the presence of extensive molecular symmetry and axial orientation, both of which are attributed to polymer crystallinity. Though in principle, polymers are capable of generating fibers of superior mechanical properties, the properties of

most polymeric fibers are much lesser as compared to even theoretical limits. The orientation and extension of polymeric chains has a major role to play in this. In order to have properties approaching those of individual bonds, not only do the molecules need to be well aligned, but also need to be extended along the orientation direction. For example, oriented fibers comprise lamellar crystals which are thin in the chain direction, separated by amorphous domains. In spite of possessing a high degree of axial orientation, they possess lower mechanical properties attributed to the relatively softer amorphous domains.

Hence, to understand the macroscopic properties of a fibrous system, knowledge of microscopic arrangement of the polymers that constitute it is essential. Various models have been suggested to describe the structural arrangement of polymers and subsequently link it with the structural morphology of the fiber. In the current review, a brief understanding of structural models for a polymer will be studied followed by specific models that describe the structure of drawn fibers.

Figure 2.1 highlights the various theories that have been suggested to describe the polymer morphology. The fringed micelle theory of the early 1930's suggests the presence of ordered regions of polymers (crystallites) embedded in a matrix of unordered regions (amorphous matrix). This was followed by the folded chain lamella theory of the late 1950s which was proposed when polymer single crystals in the form of lamellae were grown from polymer solutions. Folding of polymer molecules in a back and forth manner during the process of crystallization was suggested ⁷. This gave rise to 2 models; the adjacent- reentry model suggested a regular re-entry of a polymer chain at exactly the next point of the same

crystallite whereas the Switchboard model suggested by Flory in turn considered a disordered fold surface with the chains entering and leaving a crystal at random^{8,9}.

Further, the study of crystallization from polymer melts suggested an obvious lack of order, which gave rise to the concept of a “spherulite”. Spherulite refers to spherical structures which are formed by the crystallization of polymers from a melt without disturbance¹⁰. Typically showing a size scale of 100-150 μm , the process for spherulite formation begins at a single nucleation point from which a multi layered stack of lamellae grow radially outward, often circular in shape. Growth occurs by chain folding with the polymer chain axes perpendicular to the length of the crystalline lamellar fibril. This is indicated in the Figure 2.2 below, wherein fine fibrillar links can be observed spanning the gap between the radial arms of the spherulite. Outside of these crystalline lamellae are amorphous domains which may show the presence of physical entanglements⁷. The size of spherulites depends on conditions under which they are crystallized such as cooling rate, temperature of crystallization, nature of nucleating agent etc.

(a)



(b)



(c)



(d)

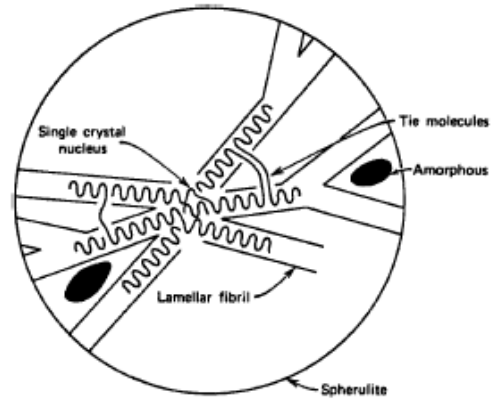


Figure 2. 1: Structural models for a fiber (a) Fringed Micelle Model, (b) Adjacent Re-entry Model, (c) Switchboard Model, (d) Spherulite.⁸

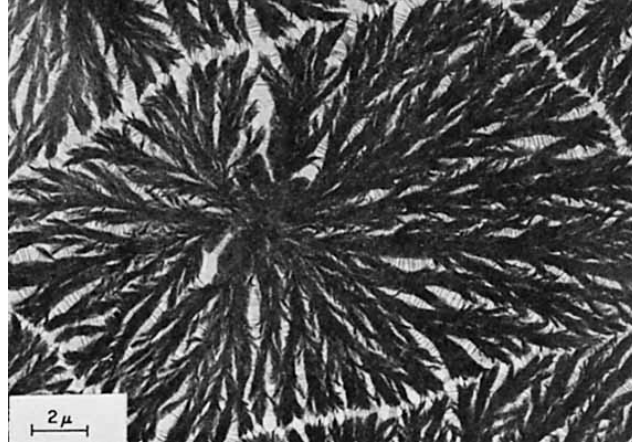


Figure 2. 2: Electron micrograph of a spherulite. The specimen was *crystallized at 90°C*.¹¹

Apart from the crystalline and amorphous domains, there are also molecules that span between crystalline lamellae which are called tie molecules. These refer to chains that exit from one crystalline lamellar region, coil in the amorphous inter-lamellar region and then re-enter another crystalline lamellar arm. This is in close conjunction with the fringed micelle theory. The tie molecules are the main component of the modern picture of semi-crystalline polymer morphology, which is a carryover from the fringed-micelle theory. The amorphous content of a semi-crystalline, melt-crystallized polymer sample consists of the defects in the chain-folding structure, tie molecules, and the material that is, because of entanglements, not included in the growing lamellar fibril⁸. The tie molecules have an important role to play in the tensile properties of a polymer. They have a direct effect on the toughness and plastic deformation of a polymer when subjected to deformation forces.

Having discussed structural arrangement in polymers from a polymer morphology standpoint, it would be pertinent to focus on models that make use of these empirical models for polymer morphology, to predict properties of macrostructural systems, specifically in case of drawn fibers. Of these, the models presented by Peterlin, Arridge and Ward deserve special mention and will be discussed below.

The earliest model correlating enhancement of mechanical properties (modulus) of uniaxially oriented fibrous structures with the crystalline and amorphous regions was provided by Takayanagi. Based on studies of crystalline morphology, Takayanagi models assumed the mechanical coupling of crystallized and amorphous systems by spherulitic structures, linking mechanical properties with the presence of tie molecules^{12, 13}. According to models developed by Takayanagi, the tensile strength of crystals along the fiber axis direction is much greater than that in the transverse direction. This implied that the major role in post yielding deformation of polymers is played by intercrystalline links formed by the association of tie molecules. These tie molecules, formed as a result of unfolding of chains during drawing were described as a connection in the axial direction of the crystalline blocks in which they were anchored.

This concept of tie molecules was further used by Peterlin, who proposed one of the most noteworthy models describing the molecular structure of drawn fibers¹⁴. A schematic of his hypothesis is provided in Figure 2.3(a) below. Based on the assumption that a polymer comprises lamella and amorphous regions (consisting of folded chains, and tie molecules), the Peterlin model claims that on drawing a fiber, microfibrils are formed which comprise

crystalline domains in series with amorphous domains, with tie molecules passing through the intermediate amorphous domains.

The Peterlin model claims that these lamellar microfibrils are grouped into fibers with the crystalline and amorphous regions of neighbouring microfibrils lined up along each other. In fact, the interconnectivity of the tie molecules between the crystalline and amorphous phases of the microfibril was suggested to affect the amorphous phase during orientation, thereby affecting the overall properties of the oriented fiber. Larger presence of tie molecules (passing through amorphous regions, interconnecting the crystalline domains) led to the formation of stronger microfibrils which was instrumental in improving the modulus of the oriented fiber.

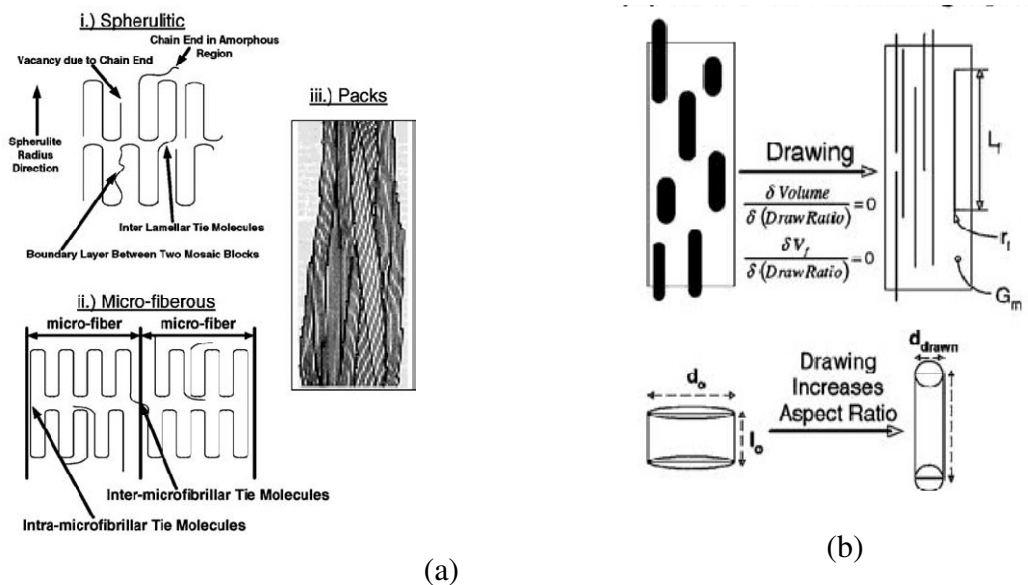


Figure 2. 3 Schematic for (a) Peterlin model, (b) Barham and Arridge model.¹⁵

In fact, the Peterlin model explicitly states that the overall improvement in mechanical properties is not due to orientation or transformation within the crystalline component but due to the better adhesion in microfibrils facilitated by stronger tie molecules. Electron Microscopy and IR dichroism was used to arrive at a conclusion that this microfibril was the basic component of the oriented fiber and axial straining and annealing of the sample led to the orientation of the amorphous region. Based on a 4 point SAXS pattern observed in oriented polyethylene fiber systems, Peterlin describes the stacking of lamellar aggregates aligned with their normal parallel to machine direction at lower draw ratios, and then tilt to a specific angle when subjected to further orientation.

Barham and Arridge used X ray diffractometry to measure crystalline strain and postulated a fiber composite model for highly drawn polyethylene fibers, based on Halpin-Tsai equations and Cox's shear lag model, to correlate the tensile modulus with the draw ratio used to orient the fibers¹⁶. Contrary to the Peterlin model (that attributes the enhancement of mechanical properties to the tightening of tie molecules in the amorphous region), Barham and Arridge suggested that the enhancement of mechanical properties in axially drawn oriented structures was due to the transformation of the crystalline phase of the polymeric system with a small aspect ratio into fibers with larger aspect ratios. For this particular model, the authors assumed that a fiber comprises cylindrical components of crystalline material and increased aspect ratios were obtained due to the orientation induced homogenous deformation of the structure. This in turn led to an increase in the reinforcing efficiency of the fibrils, thereby causing an overall increase in the tensile modulus of the fibrous structure. The schematic of

this model is indicated in Figure 2.3 (b). This model, though simple, takes into consideration only the crystalline regions and does not account for the increment in mechanical properties that might occur due to the stiffening of tie molecules of the amorphous regions.

Ward, Gibson and Davies used x-ray analysis to statistically explain the mechanical properties of oriented films of PE to the crystalline structure of the polymer¹⁷. The Ward model postulates that a fiber can be assumed to consist of parallel blocks of crystalline regions, connected by rigid tie molecules passing through the intercrystalline region. Axial orientation causes the tie molecules to become taut, leading to the formation of an oriented amorphous region. They attribute increased mechanical stiffness to the increased volume fraction of fibers, an outcome of crystalline lamellae deformation and orientation of the molecules in the amorphous region.

2.1.1. 3. Effect of fiber structure on mechanical properties

The development of useful polymeric materials necessitates a deep understanding of the morphological structure and its relation with properties. Mechanical properties of polymer are governed by many factors that include molecular weight, molecular weight distribution, polymer crystallinity, and molecular orientation and plasticization effects (such as crazing).

Notably, superior mechanical properties of polymers are attributed to their high *molecular weight* (MW). As shown in Figure 2.4, in order to obtain a significant mechanical strength there is a specific minimum molecular weight, MW (A), usually in the range of 5000-10000.

As MW is increased beyond A, a rapid increase in polymer properties is observed until a critical point B is reached beyond which mechanical properties increase less rapidly⁸. The control of molecular weight and molecular weight distribution (MWD) is often used to obtain and improve certain desired physical properties in a polymer product.

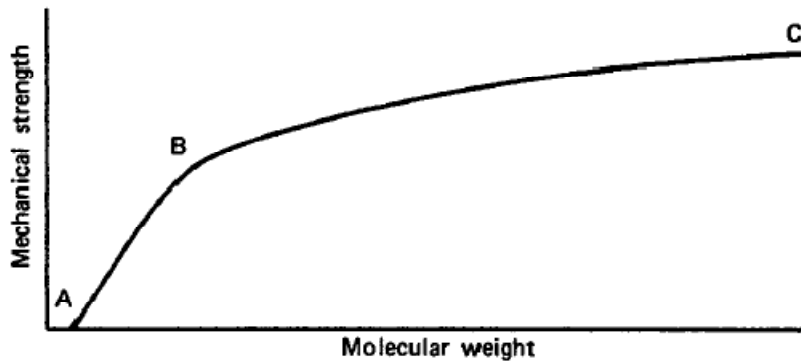


Figure 2. 4: Effect of molecular weight on mechanical strength of a polymer.⁸

Earliest studies by Perkins *et al* on the effect of MW on the mechanical properties of cold extruded HDPE indicated that the melting point, breaking strain, and tensile strength were found to increase with increasing molecular weight. This was attributed to the larger number of tie molecules present in higher molecular weight polymers.¹⁸ Similar results have been obtained by Perego *et al*, who observed that an increment in molecular weight of crystalline PLLA showed a marked effect on the tensional and flexural modulus of elasticity, impact

strength of crystalline PLLA, which seems to reach a plateau at higher molecular weights, around MW = 55,000.¹⁹

Extensive studies on natural fibers have been carried out that showed that their mechanical properties were directly related to their degree of polymerization and cellulosic content²⁰⁻²².

Gassan *et al* have studied the effect of NaOH treatment on the mechanical properties of tossa jute fibers. They observed that the alkali treatment resulted in the removal of the lower molecular weight cellulose fractions thereby resulting in better packing of cellulosic chains that resulted in a higher crystallinity. A 120 % increase in yarn tensile strength and 150 % increase in tensile modulus was observed²³.

Kreze *et al* have investigated the role of degree of polymerization (DP) and Molecular Weight (MW) in the determination of the mechanical properties of regenerated fibers Lyocell, Modal and viscose with the same chemical structure²⁴. Molar mass was determined to have the highest influence on mechanical properties with Lyocell showing higher strength than Modal and Viscose due to its longer molecules and higher DP. The higher molecular orientation in lyocell aided higher crystallinity which has also been seen as an important factor in increasing mechanical properties.

Krassig further describes the tensile behavior of various man-made fibers by Equation 1 given below²⁵. This equation shows that strength is dependent on the length of the fiber-forming (cellulose) molecules i.e., the DP, and its relation with the length of the elementary

crystallites (*LODP*), the perfection of lateral order *CrR* and on the degree of orientation *fr*.²³,

25

$$\sigma \propto \left[\frac{1}{DP} - \frac{1}{LODP} \right] CrRf_r^{2,5} \quad \text{Eqn. (1)}$$

Polymer crystallinity is yet another important determinant of the mechanical properties of a polymer, more so when it is spun as a fiber. In order to be useful as a fiber with suitable mechanical properties, the polymer must show high crystallinity and presence of strong secondary bonding⁸. However, in their as spun state, fibers do not possess mechanical properties suitable for them to be useful for application. This is because after the process of spinning, the “macromolecules in these oriented semicrystalline structures are rarely in their equilibrium state in either the crystalline regions or the amorphous regions of the fiber”²⁶.

Therefore, it is customary to introduce a process of drawing during the manufacture of fibers. During the process of drawing, the extruded filaments are made to pass over a series of godet rollers wherein the speed of the leading role is higher that of the preceding one. The process of drawing increases the molecular orientation along the fiber axis, due to mechanical stretching, thereby increasing the crystallinity of the fiber. It is important to note that this is a process carried out a temperature above the Tg of the polymer^{8, 27, 28}. Annealing, on the other hand refers to a process in which the polymer crystallinity is enhanced by heating a polymer

above its glass transition and at or below its melting temperature during its processing. The absorption of the heat by the polymer chains imparts mobility to a certain extent leading to subsequent crystallization. This increase in crystalline perfection in turn, is observed to enhance the mechanical properties of a fiber.

Heat setting is a modified annealing technique which is carried out to prevent the extreme shrinkage of PET fibers when they are cold drawn. During this process, the polymer is held in a stretched condition at its crystallization temperature. This results in improved orientation of the polymeric chains, which remain oriented even when the polymer is processed beyond its crystallization temperature due to the development of memory within the polymer. All the above mentioned treatments help to improve the mechanical properties of a fiber by improving the overall crystallinity of a polymer^{29, 30}.

The effect of *crystal orientation* has also been reviewed as this plays a critical role in the mechanical properties of high-performance fibres^{31, 32}. The change in polymer crystallinity realized by the process of improvement in molecular orientation has a profound effect on the mechanical properties of a fibrous system and has been widely studied. Young and Eichhorn in their review of deformation mechanism observed in fibrous structures have clearly stated the importance of non-crystalline orientation (amorphous orientation) in the determination of mechanical properties³². This orientation is directly related to the quantity of tie molecules present in the polymeric system of the fibrous materials. Yield strengths were observed to be higher in fibrous systems where the overall orientation was higher; Higher modulus values

on the other hand was observed to be a result of not only high orientation in the crystalline and amorphous region but also higher presence of crystalline domains^{32, 33}. Nakamae *et al* in a study of mechanical performance of Kevlar49, Vectran and PEEK (poly(ether ether ketone)) fibers, has established the co-relation between crystal moduli and mechanical properties³⁴. In high-modulus fibers all the crystals are well aligned with the chains along the fiber axis. The material stiffness is so high that the contribution of the poorly aligned or not all-trans chains can be neglected. The applied load is then equal to the sum of all the loads on the all-trans chains in a cross section³⁵. Zhang *et al* makes an important observation in his work on the crystalline morphology of lyocell fibers that for a fiber in general, the modulus of the depends on the crystallinity and crystal orientation whereas the tenacity depends on the amorphous orientation³⁶.

The complex interplay between crystallinity, overall orientation and mechanical properties is most recognized in case of PET fibers and films. An increase in tension at break and tensile strength with an increase in polymer crystallinity and molecular orientation has been noted in PP as well as PET filaments and spun bond nonwovens³¹.

2.1. 2 ELECTROSPUN NANOFIBROUS STRUCTURES

2.1.2. 1. Introduction

Electrospinning has emerged as a versatile method of producing fibers having a size scale ranging from a few nanometers to several micrometers³⁷. The process enables the efficient collection of materials with a nanofibrous structure which imparts unique properties to these,

such as high surface to volume ratio, porous morphology and most important of all diameters in the nanoscale^{38, 39}.

Electrospraying was first studied by Lord Rayleigh in the late 1880s who studied the effect of application of electric field on the surface tension of a fluid enclosed in a small capillary⁴⁰. Further, in 1934, electrospinning was patented as a valid process by Formhals for the spinning synthetic fibers using the application of electric field⁴¹. Subsequent developments have been marked by important contributions from Taylor in the 1960s who studied the process of jet formation during electrospinning and the behavior of the liquid droplet at the capillary tip when subjected to electric field⁴¹. Baumgarten in 1971 illustrated the effects of solution and process parameters on the diameters of electrospun fibers⁴². Following this, there have been many studies that illustrate the effect of process parameters on the physical properties of electrospun nanofibers.

2.1.2. 2 Electrospinning process

A typical electrospinning process is illustrated in Figure 2.5 below. Fundamentally, a horizontal electrospinning set up comprises a syringe pump that extrudes the polymer solution through capillary tube, which in turn has a small diameter needle attached to its one end; a high voltage DC power supply to charge the polymer solution and a grounded collector plate on which the nanofibers are deposited.

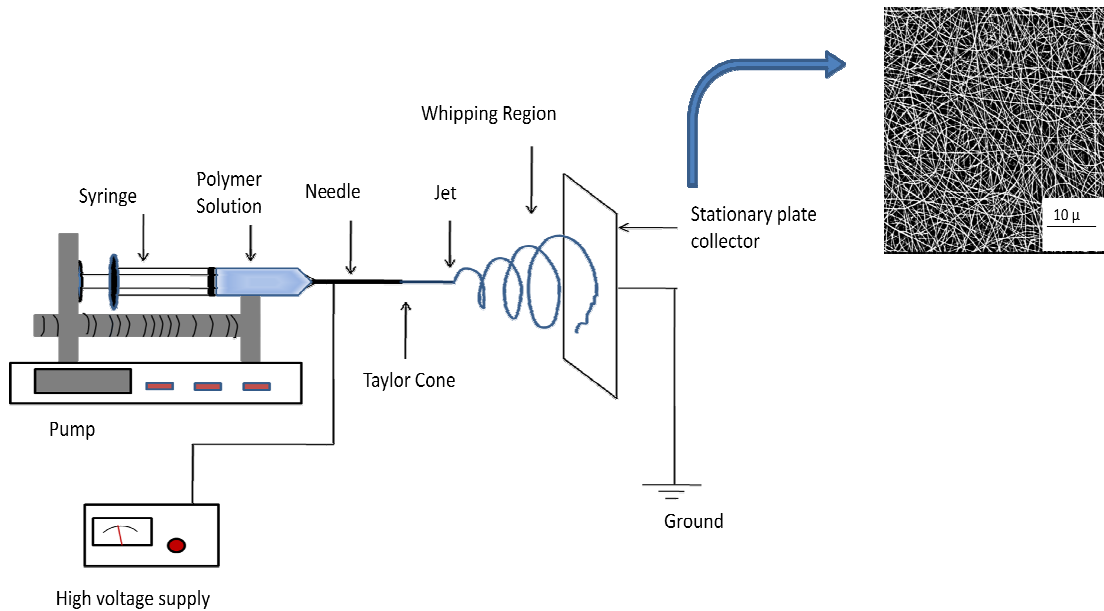


Figure 2. 5 Schematic of a typical electrospinning set up; inset random morphology of an electrospun nanofiber mat.

When an electrostatic force (high DC voltage) is applied to the polymer solution, the electric field induces a migration of ions through it, thereby charging the surface of the solution. At a particular voltage value (critical voltage), the electrostatic forces overcome the surface tension of the droplet. This causes a jet to be initiated from the conical protrusion, (which is also referred to as the Taylor cone) formed on the pendent drop of the polymer solution. The jet travels in a straight path for a finite distance (linear region) beyond which it follows a helical path in the form of a conical shape. This region in which the jet experiences multiple instabilities is referred to as the whipping region. It is in this zone that the jet diameter

decreases by various magnitudes, the solvent evaporates, leaving dried nanofibers with a random morphology on the collector surface⁴³⁻⁴⁵.

The characteristics of the electrospun nanofibers depend on many parameters that can be broadly classified into 2 categories, namely solution parameters and process parameters. Solution parameters include polymer molecular weight, solution concentration viscosity, conductivity. Extensive studies have been carried out on the effect of each of these on the properties of electrospun nanofibers⁴⁶⁻⁴⁹. Process parameters on the other hand include applied voltage, flow rate of polymer fluid, working distance, and environmental conditions (such as temperature and humidity).

2.1.2. 3 Morphology of electrospun nanofibers

Electrospun nanofibers typically exhibit a solid and smooth fibrous surface⁵⁰. When collected on a stationary plate collector, they possess a random morphology and are deposited in the form of nonwoven nanofibrous mats. However, by usage of collectors with varying geometries, different morphologies have also been obtained. These include aligned fibrous structures and other secondary structures like core-sheath, hollow fibers, and porous nanofibers. Several key morphologies are discussed below.

Aligned nanofibers were obtained by Rutledge *et al.* using parallel collector plates to obtain a uniform electric field⁵¹. They observed that alignment was enhanced when a conductive

collector frame was used as against a non-conducting one. Different methods of obtaining aligned morphologies have been studied by altering the collection mechanisms. The “air gap” method of collecting aligned nanofibers, proposed by Li *et al*, enables collection of aligned nanofibers in the gap between 2 parallel electrodes although this method had a serious drawback due to the limitation on fiber length collected between the airgaps^{52, 53}. Usage of a high speed rotating drum to collect aligned morphologies has been demonstrated by Matthews *et al*, wherein nanofiber alignment and mechanical properties increased with increasing collector speeds⁵⁴. Bundled and tubular arrays of aligned nanofibers have been obtained by Bhattarai *et al* and Sundaray *et al* by suitable modifications to the rotating cylinders in the form of auxiliary electrodes and counter electrodes respectively^{55, 56}. Aligned nanofiber yarns of Polycaprolactone (PCL) have been produced by the usage of dual collector rings by Dalton *et al*⁵⁷. This indicates that it is possible to produce not only nanofibrous structures, but also macroscopic fibrous structures like nonwoven mats and yarns with unique properties of nanofibers.

Nanofibers with a core-sheath morphology have also been obtained using a modified electrospinning technique, referred to as co-axial electrospinning. This method offers the advantage of obtaining nanofibers with the combination of properties by tailoring the specific, unique properties of the core and the sheath. First introduced by Sun *et al* in 2003, this method was further explored by Zhang *et al* to produce nanofibers of PolyCaprolactone PCL/gelatin (sheath and core respectively) for tissue engineering and drug delivery^{58, 59}. Core solution concentration was observed to be a major determinant of morphology and the

mechanical properties of the core-sheath nanofibers was observed to be higher than nanofibers electrospun from the individual polymers. Bognitzki *et al.* have demonstrated the synthesis of core sheath nanofibers of poly(p-xylene) (PPX)/ polyLactic acid PLA by the principle of template growth using electrospinning, wherein PLA nanofibers were electrospun and then coated with PPX by the usage of chemical vapor deposition⁶⁰. The usefulness of core sheath morphologies for the impartment of unique functionalities for nanoscale devices has been widely studied⁶¹⁻⁶⁵.

Hollow nanofiber/microfibers have also been fabricated using electrospinning and find application in a variety of fields like drug delivery, catalysis, nanoelectronics etc^{66, 67}. The hollow morphology can be realized by the selective removal of the core polymer (of a core-sheath electrospun nanofiber) by dissolution or thermal degradation. Hollow ceramic nanofibers and nanotubes were produced first by Li and Xia, by the usage of co-axial electrospinning, wherein non polymeric liquid (mineral oil) was used in the core and PVP with ceramic precursors were used in the sheath⁶⁸. The moisture-sensitive precursor was hydrolyzed by prolonged exposure to air, followed by condensation, and the oil was extracted using octane, resulting in the formation of ceramic nanotubes with a hollow morphology. Wendorff *et al* have created PCL microtubes with a tube diameter of 3 μ m approximately, using a combination of dry/wet electrospinning⁶⁹. Tubular morphologies of biopolymers, with special functional dopants have particularly been studied for applications like controlled drug delivery, encapsulation etc.^{61, 70, 71}.

Thus electrospinning offers the possibility of producing functionalized nanofibers, with unique morphologies, that find use in a variety of novel applications. It is pertinent at this point to summarize (Table 2.1) the various parameters that determine the morphology of nanofibers during the process of electrospinning.

Table 2. 1 Effect of various parameters on electrospun fiber morphology.

Parameters	Effect on morphology	References
Polymer MW (concentration/viscosity)	As MW increases, number of beads, droplets decreases, fiber uniformity increases	39, 72-74
Flow rate	As flow rate increases, fiber diameter increases	75-77
Solution Conductivity	Increased solution conductivity resulted in uniform fibers	72, 78
Collector geometry	Smooth fibers- stationary metal collector Aligned fibers- rotating collectors, parallel electrodes, rings, Yarns, tubular structures can be obtained	54-56, 79-81
Needle Assembly	Single Needle- Smooth solid nanofibers Coaxial 2 capillary needle- Core sheath/hollow nanofibers	82, 83

2.1.2. 4 Structural properties of nanofibers and their effects on mechanical properties

Considering that the morphology of a nanofiber has a profound effect on the mechanical properties of the nanofiber mat, it is pertinent to delve deeper into this and explain the role of crystallinity and molecular orientation on the structure of a nanofiber.

Nanofiber morphology, more specifically nanofiber diameter was demonstrated to have a very important effect on the mechanical properties of nanofiber mats. The co-relation between fiber diameter and crystalline morphology and its subsequent effect on mechanical properties has been explained by Lim *et al* in detail⁸⁴. In their study, they demonstrated that crystalline morphology of electrospun nanofibers was closely associated with the diameters of the nanofibers. This can be clearly observed in Figure 2.6 below. Nanofibers with smaller diameters showed a dense and aligned packing of lamellae and fibrils, due to which they showed higher crystallinity and molecular orientation. This increased crystallinity in the form of oriented fibrils was responsible for the increased stiffness and strength of the nanofibers of smaller diameters. This has been attributed to the large resistance to axial tensile force offered by the *oriented fibrillar structure*. On the other hand, nanofibers with a higher diameter showed a distinct *absence of fibrillar structures* and the lamellae were observed to be misaligned. The fact that larger diameter fibers had a much larger elongation necessitates an understanding of the molecular arrangements within these fibers, with a critical understanding of the process of electrospinning itself.

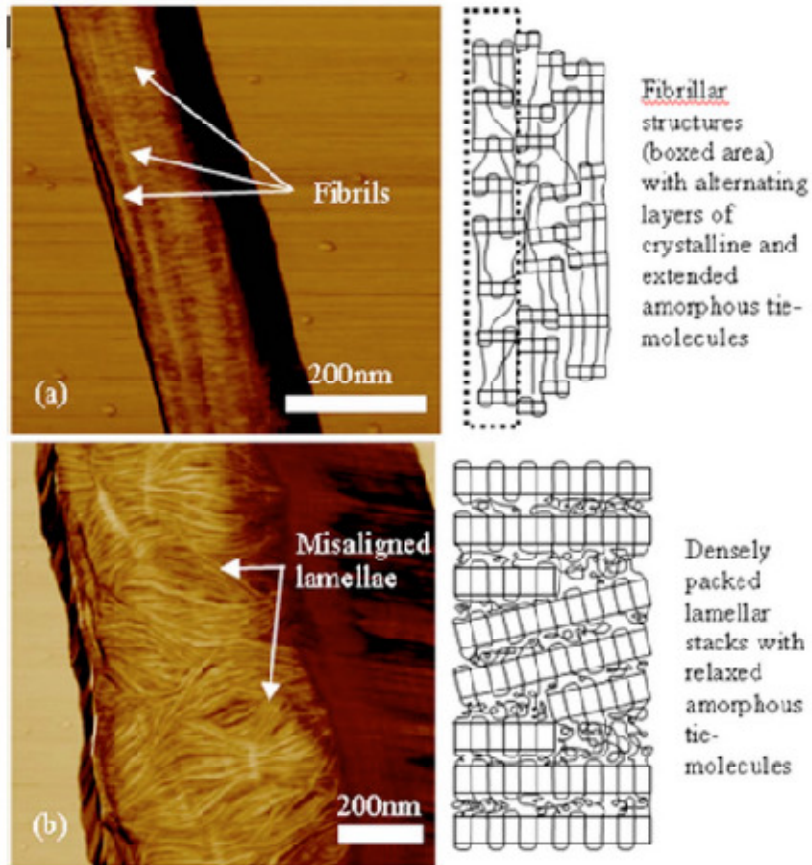


Figure 2. 6:AFM phase images showing the surface morphologies of PCL nanofibers with a diameter of (a) 150 nm and (b) 450 nm.⁸⁴

During the process of electrospinning, the jet formation stage is marked by the presence of highly oriented macromolecular chains in the solution. However, during the bending instability, chain relaxation occurs. Complete crystallization of polymer chains is realized only when it is deposited on the collector causing the resultant crystalline morphology to be less ordered and lamellar. On the other hand, more whipping, coupled with complete crystallization of polymer chains before reaching the collector and additional elongation of

the jet causes the crystallized lamellar structure to stretch. This kind of drawing is likened to the increase in molecular orientation that occurs in spun filaments, when they are drawn on godet rollers, with a resultant increase in mechanical properties^{84-87, 87, 88}. Also the amorphous regions of the more ordered morphologies is marked by the presence of extended tie molecules whereas the ones in misaligned morphologies show relaxed tie molecules which also confirms the large elongation values and strain hardening that was being observed in the larger diameter nanofibers obtained by Lim *et al*⁸⁴.

Molecular orientation, during the process of electrospinning, is thus observed to be a major determinant of mechanical properties of the nanofiber web. The fact that the polymer jet itself is under the influence of electric field; capable of producing elongation strain 10^6 times draw rate is large enough to bring about alignment of molecular chains during the process itself^{86, 89-91}. This is verified by Zong *et al* who showed that the macromolecular chains in an electrospun PLLA nanofiber mat were in highly oriented state as compared to the random coiled state found in a PLLA film⁹². The fact that electrospinning as a process in itself is responsible for macromolecular chain orientation has been widely demonstrated^{90, 93}. In a particular study by Wong *et al*, the tensile properties of electrospun PCL (Sample 1) were compared with that of a non spun extrusion molded PCL sample (Sample 2)⁹⁰. The results as demonstrated in the Figure 2.7 below indicate the fundamental differences in tensile behavior between an electrospun sample and an extruded sample. While the electrospun samples do not show necking behavior (due to oriented polymer chains), the molded sample demonstrate clear necking.

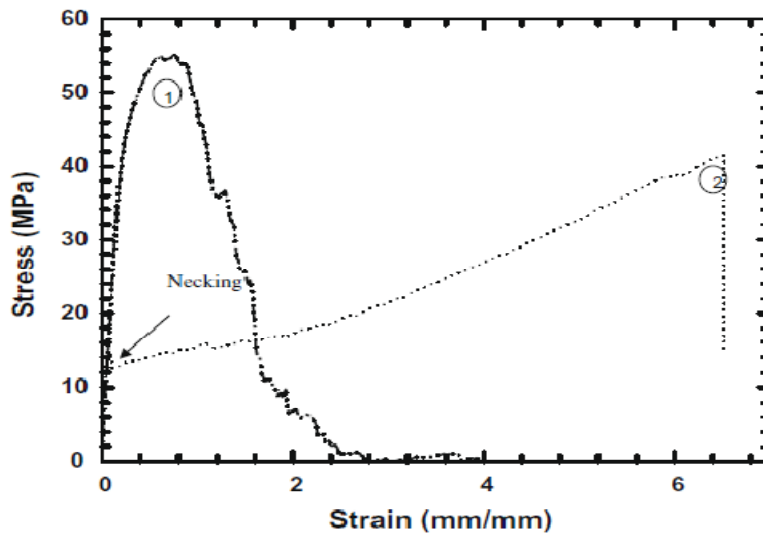


Figure 2. 7: Stress–strain curves obtained from tensile tests performed on electrospun PCL and non-spun PCL samples.⁹⁰

Increased molecular orientations have also been realized by the usage of rotating collectors. As explained by Kongklang *et al*, the rotational speed of the collector exerts a shearing, elongational force on the polymer chains, causing molecular orientation in the axial direction, which is observed to increase with an increase in rotational speeds⁹⁴. Kotaki *et al* has referred to this phenomenon as the “Fanning effect” wherein the high speed rotation causes quicker evaporation of solvent, thereby resulting in the formation of extended chain crystals⁹⁵. It is germane to note that this extended chain crystal morphology was not observed in nanofibers that were collected between stationary parallel electrodes, even though macroscopic alignment was demonstrated.⁹⁰ Huang *et al* compared the tensile properties of an aligned

nanofiber mat with that of a random one and observed that the axially aligned mats possessed higher tensile strength and modulus⁹⁶. Uniaxial orientation that enables equal distribution of tensile stress, higher packing density, lesser inter fiber spacing, and lower nanofiber diameters as a consequence of higher rotational speeds have been suggested as the reasons for improved mechanical properties of oriented mats^{56, 81, 97-99}.

2. 2 NANOCOMPOSITE MATERIALS

In this section, a brief overview of nanocomposites will be presented. Types of nanoparticles used in the fabrication of polymer nanocomposites will be covered, with special emphasis on nanofillers. The changes the crystalline morphology of the polymer as a result of nanoparticle addition, and subsequent effects on mechanical properties of the nanocomposite will be reviewed.

2.2. 1 Introduction

Polymer nanocomposites refer to a specific class of nanomaterials with polymers as the matrix phase and nanoparticles acting as reinforcement. Polymer nanocomposites have been of particular interest due to their ability to be tailored to provide enhanced properties for a variety of applications^{39, 100}. Conventional methods to fabricate nanocomposites include solvent blending, melt blending, and insitu polymerization to name the most common routes. Each of these has its own shortcomings, the most faced problem being the difficulty in

obtaining a nanoscale particle dispersion^{101, 102}. Electrospinning on the other hand has emerged as a process for the fabrication of nanocomposites, which can be produced by blending/ incorporation of various nanoparticles within the fluid before electrospinning the nanofibers¹⁰³⁻¹⁰⁵.

To have a better understanding of nanocomposites and the microstructure therewith, it would be relevant to begin with the basic components of a nanoscale composite material. Primarily, a nanocomposite comprises 3 components, namely the polymer matrix, the nanoparticle filler and the interfacial material. By volume, the polymer matrix is the largest component of the nanocomposite. Hence its structural chemistry, molecular architecture, coupled with its interaction with the nanofiller determines the overall mechanical properties of the nanocomposite. Nanofillers, their chemistry and the effect of their structure on mechanical properties of a nanocomposite will be the focus of this review.

2.2. 2 Different types of nanoparticles

Nanofillers in various sizes, shapes and geometries, of different chemistries, have been used in conjunction with polymers for the fabrication of electrospun polymer nanocomposites.

The most common structures/shapes in which nanoparticles are used include nanospheres, nanorods, quantum dots, nanotubes, and nanocages, available in 1/2/3-dimensional morphologies^{106, 107}.

Carbon nanotubes (CNT) feature among the most popular nanofillers which are used in the fabrication of a polymer nanocomposite. Their high aspect ratio, combined with their ability

to withstand torsional and flexural forces, makes them an ideal material for reinforcements.^{108, 109} Their high thermal and electrical conductivity is an added advantage for the synthesis of conductive nanocomposites for energy storage, fuel cells, and batteries^{110, 111}. Their ease of dispersion at lower loading concentrations and ability to be incorporated into a polymer nanofiber during electrospinning has led to extensive research being carried out in the field of electrospun CNT nanofiber composites¹¹².

Silica nanoparticles have also been popular for compounding with polymers to produce mechanically strong nanocomposites for a wide variety of applications covering electronics, aerospace, etc¹¹³⁻¹¹⁵. They belong to the class of inorganic fillers, which are helpful in the improvement of the strength and thermal stability of the composites due to their inherent rigidity¹¹⁶. In a strategic work by Denault *et al*, the mechanical properties of nanocomposites loaded with 2-5 % of layered silicates was found to be similar to those achieved in conventional polymer composites when loaded to 30-40 %¹¹⁷. The addition of inorganic nanoparticles organoalkoxysilanes especially in combination with epoxy silanes, has been explored for improving the hard coating on eye lenses, which improves their abrasion resistance without losing transparency¹¹⁸.

Apart from their use for the improvement of mechanical properties, selected nanoparticles are also used for specialized applications. Titanium dioxide nanoparticles have been used for their strong photo catalytic properties for the application of nanocomposites in filtration¹¹⁹. Quantum dots of Cadmium Selenide and Zinc Selenide have been used in nanocomposites for semiconductor devices and optical switches^{120, 121}. Gold and Silver nanoparticles have

been incorporated into polymer matrices and used in the fabrication of unique nanodevices for biological and chemical sensors. These properties include magnetism, exhibition of Plasmon resonance, and fluorescence^{122, 123}.

2.2. 3 Structural properties of nanocomposites: Role of nanofillers

High surface to volume ratios of nanofillers that offers large reinforcement properties at relatively small loadings is the basic principle of the functioning of polymer nanocomposites. Nanofillers or nanoparticles, being in the nanoscale regime, exhibit high surface area, thereby maximizing the amount of interfacial region between itself and the polymer. The interfacial region controls structural arrangements on the molecular scale and is thus responsible for the realization of unique new properties when it is maximized¹²⁴⁻¹²⁷.

In this aspect the chemistry of the nanofiller has a major role to play in the structural properties of a nanocomposite. The chemistry has a direct effect on the type of interactions of the particle with the polymer; these interactions may include enthalpic interactions like Vander Waals forces between the nanoparticle and the polymer, ionic / covalent bonding, hydrogen bonding.^{124, 128}. These interactions have a direct impact on the morphology of a polymer nanocomposite, especially at higher volume fractions of the filler.^{124, 129}. This is because the nature of these interactions affects the size of the particle aggregates; In case of higher inter particle interaction, nanoparticles can aggregate and instead of retaining their original unique properties as a nanofiller, they begin to act as a larger particle. Extremely weak interactions can lead to the deformation of particles thereby leading to loss of

mechanical energy. Hence the effective dispersion of nanofillers within the polymer matrix is a key factor that determines the structural properties of a nanocomposite.

Filler dimension is yet another determinant of the quality of the interfacial region. With the usage of smaller nanoparticles, there will be more surface area available for interactions with the polymer, thereby increasing the area of the interfacial region, which is beneficial to the transfer of stresses between the polymer and the filler¹³⁰.

Excluded volume interactions and their associations with conformational entropy of the polymer chain also affect the structural properties of the nanocomposite. The exuded volume refers to the volume around a particle that cannot be occupied by another particle, the entropy of the particle generating a repulsive force. Crosby *et al* suggests that “An important conclusion from excluded volume contributions is that high-aspect ratio objects, such as long cylinders, are increasingly difficult to disperse isotropically as the aspect ratio, L/r , increases. In other words, ordered phases, similar to liquid crystalline transitions, will develop at low volume fractions of fillers”¹²⁴. Lee *et al* have studied the effect of this nano-scale mechanism on the deformation of glassy polymers and concluded that the conformational entropy of polymer chains can cause the fillers to be “pushed” towards the polymer coil that in turn altered the crazing morphology of the glassy polymer¹²⁹.

Crystal structure and overall crystallinity of the polymer is observed to change by the addition of a nanofiller during the fabrication of a nanocomposite. While in some cases, the addition of nanofillers was observed to aid crystal growth, other reports have observed the addition of nanofillers resulted in hindering crystal structure and growth. Both these cases will be discussed in detail.

Nucleation crystallization is a phenomenon that has been observed in the nanocomposites wherein the addition of a nanofiller resulted in improving the crystalline morphology of the polymer because of the nanofiller acting as a nucleation site for crystallization to occur. For instance, Naebe *et al* demonstrated that the addition of CNT was observed to induce crystallization in the host polymer that caused crystalline polymer layers to be formed around them. In a separate study by the same research group on PVA/MWCNT nanofibers, crystallinity induced in the fibers was attributed to both, the process of electrospinning itself as well as the nucleating ability of the CNT, when placed in a polymer matrix^{131, 132}. They suggested that the electrospinning process itself was responsible for the crystallization, with the rapid fiber stretching and solidification that the process provided, leaving very little time for PVA to crystallize around the CNT¹³³. Baji *et al* in their study of carbon nanotube reinforced electrospun nylon nanofibers have suggested that the presence of CNT acted as a nucleation site for crystallization to occur and promoted the formation of the α -crystalline phase^{91, 134, 135}. Nucleation crystallization of polymers induced by nanofillers for various polymers has been widely studied¹³⁶⁻¹³⁸.

However, at higher doping concentrations, nanofillers have been observed to retard crystallization, mainly due to diffusion problems and aggregate formations^{114, 139-141}. Waddon and Petrovick suggest that this is because, in a material which is doped with even a moderate volume fraction of nanofillers, the separation between the particles will also be in the nanoscale regime, which is of the same size scale of the polymer chain parameters like end to end chain distance and radius of gyration. However, at higher volume fractions, chain dynamics will be affected thereby introducing constraints on the polymer chain topology¹⁴². The nanospheres have been referred to as non crystallizable impurities that affect the kinetics of crystal formation. Bhimraj *et al* studied the effect of Al₂O₃ nanoparticles addition on the crystalline morphology of PET^{143, 144}. They observed that the addition of alumina fillers retarded the nucleation of crystals. They attributed this to the disruptive effect of alumina nanofillers on the spherulitic morphology of the polymer due to their physical size and proximity to one another. XRD studies confirmed a reduction in lamellar thickness due to filler addition. Several other studies on the effect of nanoparticle addition on crystalline morphology have also been reported¹⁴⁵⁻¹⁵⁰.

2.2. 4 Effect of structural properties of nanocomposites on mechanical properties

In case of polymer based nanocomposites, the mechanical properties are directly related to the hierarchical microstructure which is in turn affected by a variety of factors like matrix properties, filler chemistry, distribution, bonding of the filler with the polymer interphase, etc.¹⁵¹. Considering the broad range of factors that are involved, this review, in particular,

will focus on the role of nanofillers in the determination of nanocomposite mechanical properties.

Before going into the details of the effect of structural morphology of a nanocomposite on mechanical properties, it is pertinent at this point to explain the deformation mechanism that occurs in a nanocomposite when it is subjected to tensile axial loading. Kim *et al* has suggested the following model (Figure 2.8) to describe the various stages of deformation that occur in an electrospun nanocomposite with nanoparticles in a binary phase system¹²⁷.

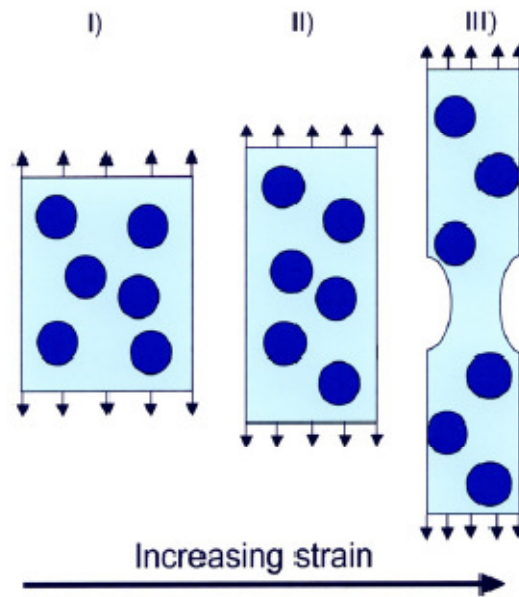


Figure 2. 8: Schematic illustration of mechanical deformation processes of the electrospun PMMA nanocomposite with 10 weight % of SiO₂ under uniaxial tensile load.¹²⁷

As seen in the figure above, Stage 1 shows the nanoparticles finely dispersed into the polymer matrix. Potentially, these fillers will act as stress concentrators when subjected to tensile load due to their elastic properties being different from that of the matrix. In the 2nd stage, on application of load, slight deformation of the fibers along with the nanofillers occurs. Shear yielding of the matrix between the nanofillers occurs due to the stresses generated by the individual nanoparticles. As the strain increases, shear yielding occurs. In the 3rd stage, beyond a certain value of stress, necking occurs at the point where the stress is highly concentrated i.e. at the nanoparticles. Any increase in strain beyond this point is accompanied by the propagation of the necking, accompanied by a crease in yield strength until the nanofiber composite yields completely. Kim makes an important observation that during this entire process, the structure of the nanofiller remains intact thereby acting as reinforcement for the matrix. This is the reason for the high stiffness and toughness of a nanocomposite. Having discussed the deformation mechanism in a nanocomposite, we can look into the various aspects of nanofillers that affect the mechanical properties of a nanocomposite.

Optimal nanofiller concentrations along with uniform dispersion are a very vital determinant of the mechanical properties of the nanocomposite. A uniform distribution not only prevents localization of stresses, but also enables a good interfacial bonding to be developed to achieve effective load transfer^{127, 152, 153}. An ideal example is in the case of CNT composites, wherein the addition of CNT to a polymer at lower concentrations was observed to increase the tensile modulus at lower concentrations, due to the reinforcement provided by the stiff

CNT¹⁵⁴⁻¹⁵⁶. However, at higher concentrations, the tensile moduli were observed to decrease. This has been attributed to the aggregation of CNTs that occur at higher concentrations, making lesser area available for interaction with the polymer, causing lesser interfacial regions available for load transfer. Moreover these aggregates act as sources of stress concentration, which in turn causes the structure to fail earlier. Similar trends have also been observed by other researchers, wherein an increase in filler concentration was observed to reduce the tensile modulus¹⁵⁷⁻¹⁵⁹. Thus we see that there are critical loading concentrations at which maximum tensile properties are realized, depending on the nature of the nanofiller used.

Inter Filler interactions are an issue of major concern in polymer clay composites, wherein 2 morphologies are possible namely exfoliated and intercalated. In the exfoliated morphologies, filler particles are well dispersed and its length as well as geometric stiffness is very small. On the other hand, in the intercalated morphology, though a uniform dispersion of filler is present, the clay filler shows multiple layers of clay sheets which are strongly attracted to each other and behave similar to larger fillers. This causes the mechanical properties of intercalated morphologies to be very different since the surface to volume ratio has reduced substantially.^{124, 139}.

Nature of the interfacial region between the polymer and the nanoparticle plays a major role in the transferring of load across the nanocomposite. Yield stress was found to decrease (relative to the polymer matrix alone), in cases where poor interaction of nanoparticles with

the matrix was present^{157, 158}. This has led to the usage of functionalized nanoparticles, that help to increase improve the filler-polymer bonding. An example of improved mechanical properties due to usage of functionalized nanoparticles has been demonstrated by Tjong as indicated in Figure 2.9 below¹⁵¹.

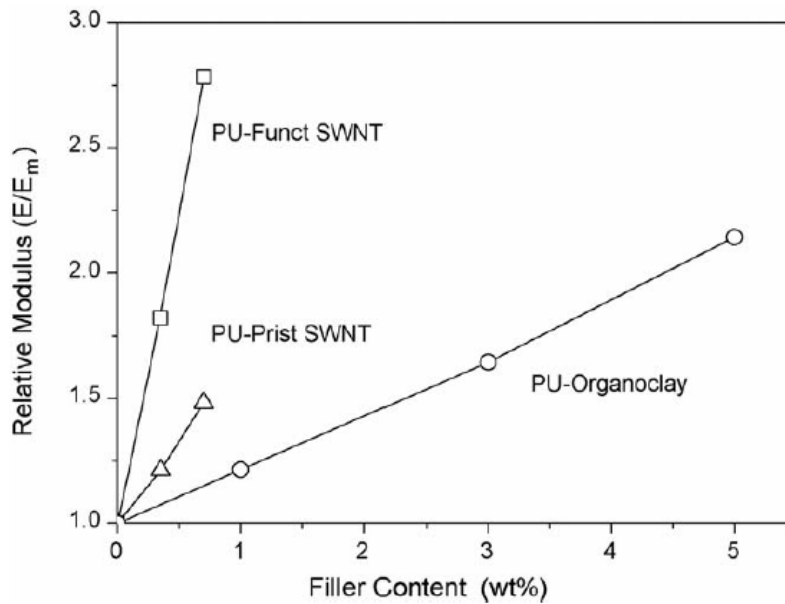


Figure 2. 9:Relative modulus (E/Em) vs. filler content for PU reinforced with pristine SWNT , functionalized SWNT and organoclay nanoparticles.¹⁵¹

The Figure 2.9 shows the effect of addition of 3 different types of nanoparticles, namely functionalized Single wall Nanotubes SWNT, pristine SWNT and organoclay on the mechanical properties of a polyurethane (PU) nanocomposite. Functionalized SWNTs were observed to provide a higher provide higher modulus in PU than the pristine one. This has

been attributed to the better dispersion and stronger interfacial attraction between PU and the functionalized SWNT as compared to the latter^{151, 160, 160, 161}. On the other hand, a different type of reinforcement was provided by the organoclay nanoparticles wherein their addition enhanced the strain at break of the sample. The authors attributed this to the different morphologies (exfoliated, intercalated) that may have been assumed by the clay nanoparticles when dispersed within the matrix.

Nucleating ability of the nanofiller is also an important determinant of polymer nanocomposite mechanical properties. Nucleation induced by nanoparticles was found to improve the crystallinity in various polymer nanocomposite systems^{162, 163}. Electrospun nanocomposites of Nylon 6,6 nanofibers with MWCNT were observed to possess higher stiffness and strength⁹¹. The authors attributed this to the nucleating crystallization effects of the CNT coupled with the restricted mobility of the polymer chains by the CNT. Crystallization retarding effects of nanoparticles, that stem from aggregate formation (explained earlier), on the other hand were observed to affect the mechanical properties of a nanocomposite.

Thus the importance of nanocomposite in the overall improvisation of structural and mechanical properties, that makes them unique from a polymer composite, focusing on the role of nanofillers, has been summarized.

2.3 POST PROCESSING: CONVENTIONAL ANNEALING

2.3.1 Annealing effects on crystallinity in bulk polymers

Annealing of a semicrystalline polymer at temperatures significantly above the polymer glass transition (but below the melt temperature), leads to an increase in crystal size and perfection.^{164, 165} High temperature annealing has been found to improve polymer crystallinity by aiding both nucleation and growth mechanisms of spherulitic superstructures, with lamellae as the dominant crystal form within the spherulites.¹⁶⁶ Thermal annealing was found to increase the thickness of single crystal lamellae in polyethylene crystallized from solution. This was accompanied by lateral perfection of crystallites which was suggestive of major chain refolding of the molecules.¹⁶⁴ Kawai et al propose partial melting of smaller crystals followed by recrystallization with thicker lamellae to be the reason for the increase in thickness of lamellae during thermal annealing, during which melting and recrystallization effects were found to occur.¹⁶⁷

Specifically in case of bulk low molecular weight PEO, crystallization mechanisms on annealing have been evidenced by the presence of non-integrated folding crystals as the initial transient state which on annealing result in lamellar thickening causing an increase in the thickness of bulk crystals and finally result in chain folding.^{168, 169} Spherulite growth in PEO films shows a distinct temperature dependence with spherulite sizes being affected by cooling rates.^{169, 170} Annealing and crystallization studies done by Chen et al at a range of temperatures (55-58 °C) close to the melting temperature suggests the melting of once folded chain crystals from the inner parts of the lamellar surface and thickening of the lamellar

edges into extended chain crystals during annealing.¹⁷¹ Recrystallization at the sides of the lamella with the lamella acting as nucleation sites for crystallization have also been suggested. Other studies by Massa et al suggest that annealing PEO systems (films) at temperatures close to and above the melting temperatures was found to destroy the spherulitic morphology, melting the crystallized chains and causing them to relax from their crystalline morphology.¹⁷²

2.3. 2 Effect of annealing on conventional structures

Annealing refers to a process in which the polymer crystallinity (of a semi-crystalline material) is enhanced by heating a polymer well above its glass transition temperature (but below the melt temperature) during its processing. The absorption of the heat by the polymer chains imparts mobility to a certain extent leading to subsequent crystallization (or recrystallization or cold crystallization). This in turn is observed to enhance the mechanical properties (specifically the modulus) of a fiber²⁷.

As mentioned before, the most common effects of annealing at temperatures significantly above the polymer glass transition include increase in overall crystallinity and crystal size in the polymer. A more perfect arrangement of crystals is obtained, that causes the overall density of the fiber to increase; an effect that cannot be caused by just increase in overall crystallinity¹⁷³. The process of annealing differs from drawing in the fact that the observed increase in crystallinity is due to the crystallization of oriented amorphous fractions in the polymer¹⁷³.

Gupta *et al* explain the effect of high temperature annealing on the morphological structure of a semi-crystalline polymer using Polyethylene terephthalate as a model ^{174, 175}. High temperature annealing was observed to cause an initial rapid increase in crystallinity. This stage has been attributed to “primary crystallization”, during which, a rapid growth of crystals occurs in the already existent nuclei present in drawn PET fiber, thereby causing major structural reorganization. Over time, the smaller crystals can merge to produce bigger ones, and the reduction in smaller crystals can overall cause a more uniform perfect crystal formation. Beyond primary crystallization, further annealing can result in secondary crystallization to occur, with the perfection of crystals improving due to the disappearance of crystal defects. Secondary crystallization shows a distinct time dependence ¹⁷⁵.

Figure 2.10 below shows the polarizing optical micrographs of PET films that were prepared by melt crystallization, by (a) a linear cooling rate (1 K/min), (b) an ice bath quench, (c) , cooling at 1 K/min and then annealed at 473 K for 60 minutes, and (d) quenching in an ice bath and then annealed at 473 K for 60 minutes ¹⁶⁶. As observed, the linear cooling resulted in the formation of a spherulitic superstructure, which increased in size due to the post annealing. The quenched samples on the other hand showed no superstructure development and were fully amorphous. Upon annealing, small spherulites seen to nucleate from the originally amorphous material. The authors surmised that the process of post annealing was responsible for both nucleation and growth mechanisms, with lamellae as the dominant crystal form within the spherulites ¹⁶⁶.

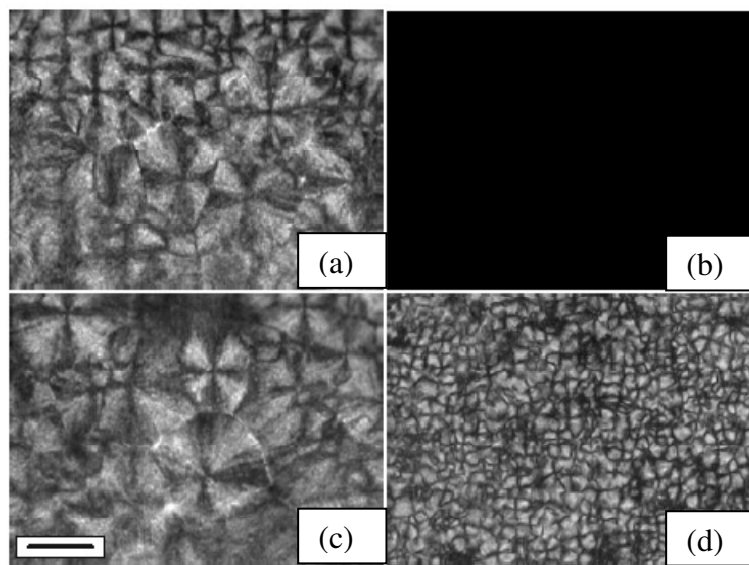


Figure 2. 10: Polarizing optical micrographs of a PET film of 100 μm thickness, melt-crystallized at 1 Kmin^{-1} (top, left), or quenched in ice water (top, right). The bottom images show the structure after additional annealing at 473 K for 60 min. The scaling bar represents a distance of 20 μm ¹⁶⁶

Enhancement of mechanical properties of a polymer is a direct outcome of the improvements in crystallization provided by annealing. Modulus and overall strength of the fibers is increased by the process of post processing annealing induced crystallization that reduces the degree of molecular randomization. As mentioned before, the semi-crystalline polymeric structure of a fiber comprises chain folding lamellae that radiate from a nucleation site to form a spherulite, with a single polymer chain capable of existing in more than one lamella or spherulite. The tie molecules (intercrystalline molecular fragments) determine the load bearing strength of the polymer. Higher molecular weight polymers possess longer polymer chains, with more number of tie molecules, which results in higher strengths.

The variables that determine the effect of annealing on the mechanical properties of a polymer include annealing temperature, annealing time, mode of annealing (constrained or unconstrained), and history of the sample (effect of pre-drawing).

Temperature at which annealing is carried out is observed to have a very important influence on the modulus and tensile strength of the fiber. Studies indicate that to reap maximum benefits of annealing for mechanical property improvements, the process should be carried out near the melting temperatures for semi-crystalline polymers or above the glass transition temperature for amorphous polymers^{176, 177, 178}. Babatope *et al* have studied the effect of annealing temperatures (60-200 °C) on the mechanical properties of Nylon 6,6 extrudates¹⁷⁹. Significant improvements in tensile modulus (and small increase in tensile strength) were reported up to 150 °C possibly due to substantial chain motion, causing increased crystallinity. Annealing at 200 °C was observed to deteriorate the mechanical properties. Interestingly, the improvement in mechanical properties was more significant at 60 °C as compared to 100 °C. A microstructure based explanation by the authors suggests that at 60 °C (near T_g), hydrogen bond rupture occurs but chain mobility is not introduced as yet. At 100 °C however, hydrogen bond rupture, coupled with chain mobility (causing relaxation of load bearing chains) is responsible for poorer mechanical properties as compared to 60 °C annealed ones. The poor mechanical properties at 200 °C, has been attributed to the thermal degradation of tie molecules. Thus the temperature of annealing, relative to the glass transition and melt temperature play an important role in the mechanical properties determination of the polymer.

The type of annealing (*i.e.*, constrained or unconstrained annealing) also plays an important role in microstructure development that determines the mechanical properties. Gupta *et al* have demonstrated the effect of type of annealing on the mechanical properties of PET filaments, the results of which are indicated in Figure 2.11¹⁷⁴

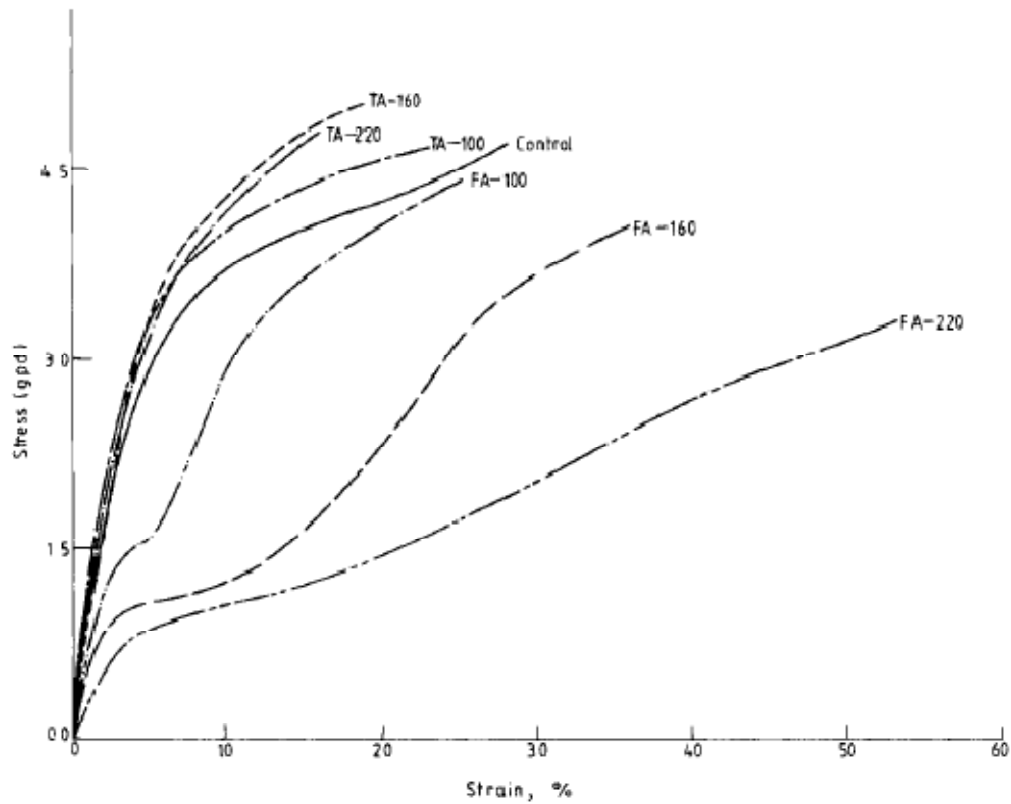


Figure 2. 11:Stress-strain curves for samples heat set for 1 min at 100 o C, 160 o C, and 200°C and for control sample (FA, free-annealed; TA, taut-annealed).¹⁷⁴

As seen above, the constrained (taut-annealed) samples demonstrated a higher breaking stress, and a lower elongation than the control sample. On the other hand, unconstrained (free-annealed) samples showed relatively higher elongations and lower breaking stress values. The taut annealed samples show a brittle behavior as compared to the ductile yielding behavior observed in freely annealed ones.

A very important mechanism of tensile deformation has been explained as a function of annealing temperatures and type of annealing. In the freely annealed samples, the number of oriented tie molecules will be very small, resulting in high stress concentrations and the ease of deformation (1st yield point). Strain hardening occurs subsequently due to the uncoiling of the interlamellar amorphous regions. As the annealing temperature is increased, an increase in yield strain coupled with a decrease in yield stress occurs due to the lower amorphous orientations in freely annealed samples. On the other hand, in constrained annealed samples, the material extends uniformly, with a uniform distribution of strains and the crystalline phase offering a resistance to deformation. Moreover, considering that the amorphous orientation is relatively higher, there is more resistance to further extension. The yield point is very close to the fracture point, considering that beyond yield, a major snapping of tie molecules with mass slippage might have occurred.

2.3. 3 Effect of annealing on electrospun structures

Electrospun nanofiber mats show poor structural integrity due to the lack of inter fiber bonding and molecular orientation. Though, electrospinning has been demonstrated to

produce nanofibers of well defined crystalline order, due to the additional step of in process drawing, this is true only in case of lower polymer concentrations and very small diameter nanofibers¹⁸⁰. On the contrary, crystallization retardation during electrospinning has been reported by many studies, that attributed this phenomenon to rapid solidification of the polymeric chains during the later stages of electrospinning, implying that the elongated polymer chains did not have enough time to organize into an ordered crystal structure before solidification^{181, 92, 182}. Lack of crystalline order, combined with limited interfiber bonding can be attributed to the poor mechanical properties demonstrated by electrospun nanofiber mats. Strategies to improve the mechanical properties aim to address this problem in 2 ways, namely (1) creating ordered morphologies by altering the electrospinning process (that is, to produce aligned nanofibrous mats) and (2) post processing treatments^{39, 183-185}. Post processing thermal annealing in particular has emerged as an effective method for improvisations in the mechanical properties of a nanofiber web.

The effect of thermal annealing on the structural morphology of electrospun nanofiber has been explained by Lim *et al.*¹⁸⁰.

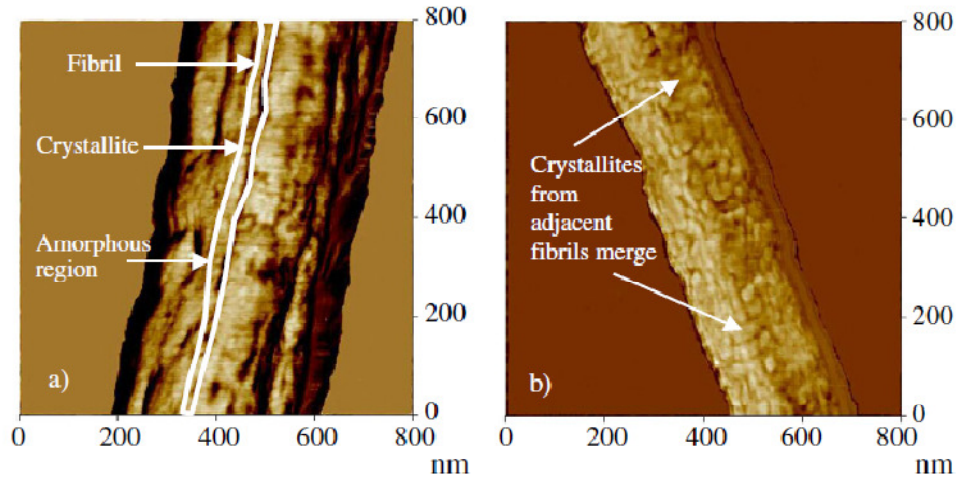


Figure 2. 12: Phase image of electrospun PLLA nanofiber (as-spun nanofiber) and (b) annealed nanofiber.¹⁸⁰

As shown in Figure 2.12, the as spun nanofiber shows a fibrillar structure with distinct crystalline and amorphous regions, with the fibrils being aligned along the fiber axis (direction in which fiber is drawn during electrospinning). The interfibrillar region comprises aligned non crystalline molecules (tie molecules). Annealing was observed to increase the size of the crystallites, and merging of larger crystallites with those from adjacent fibrils was observed. The authors also hypothesized that this merging maybe a result of the intermittent tie molecules crystallizing. Significant reductions in fiber diameters corroborate the hypothesis that annealing caused the amorphous chains to rearrange and form more closely packed crystallites. DSC thermograms verified that the increased crystallinity was due to the crystallization of non-crystalline oriented structures.

Effect of annealing on the improvement of inter fiber bonding has also been widely demonstrated^{176, 181, 186, 187}. Studies indicate that to introduce interfiber bonding in semi-crystalline polymer based nanofiber webs, annealing should be carried out at or above melting temperature, whereas for amorphous polymer, annealing temperature should be well above the glass transition temperature^{176, 110, 177}.

Choi *et al.* have examined the effect of morphological changes in electrospun mats of Polyetherimide (PEI), when subjected to thermal annealing at 80-240 °C in a convection oven¹⁷⁶. Fibers treated at 240 °C showed a clear presence of inter fiber bonding, above its glass transition temperature, which was not present at temperatures 80-220 °C as shown in the Figure 2.13 below. This was observed to have a direct impact on the mechanical properties of annealed webs, with the 240 °C annealed samples showing a higher modulus and significantly less elongation than as-spun nanofiber mats.

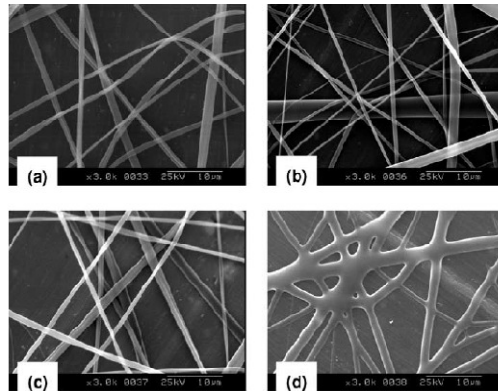


Figure 2. 13:Scanning electron microscopy (SEM) images of electrospun PEI nanofibers after thermal treatment at (a) 80°C, (b) 150 °C, (c) 220 °C, (d) 240 °C.¹⁷⁶

You *et al.* thermally bonded electrospun poly (L-lactic acid) nanofibers slightly above their melting temperature in a convection oven and reported the effect of thermal annealing on the mechanical properties of the web ¹⁷⁸. Tensile strength in the electrospun fibers was observed to be maximum when the fibers were physically joined without severe surface or bulk modification and maintained their three dimensional structure, thereby emphasizing the importance of inter-fiber bonding.

Thermally bond electrospun fibers of Poly Lactic Acid with varying concentrations of MWCNT were studied by Gorga group to determine the effect of different annealing temperatures on the mechanical and electrical conductivity properties ¹⁸⁸. Annealed samples showed an increased modulus and strength in both cases i.e. with and without MWCNT. However, the conditions that determine the maximum tensile values in each of these systems are dependent on cold crystallization. 100% PLA nanofibrous mat exhibited cold crystallization when annealed near their melting point, which resulted in a sharp increase in mechanical properties. On the other hand, cold crystallization in MWCNT doped mats was observed to be impeded. This study thus shows that the increment in mechanical properties which is obtained by thermal annealing varies depending on the presence of dopants in nanofibers ¹⁸⁸.

Ravandi *et al* report the usage of a thermal zone between the needle and rotating collector to obtain aligned as well as heated electrospun samples of PAN ¹⁸³. Treated samples demonstrated an increased modulus coupled with lower fiber diameters and elongations. The heat treatment coupled with the tension of collection was reported to be the cause for the

higher molecular orientation in the axial direction, which resulted in enhanced tensile strength.

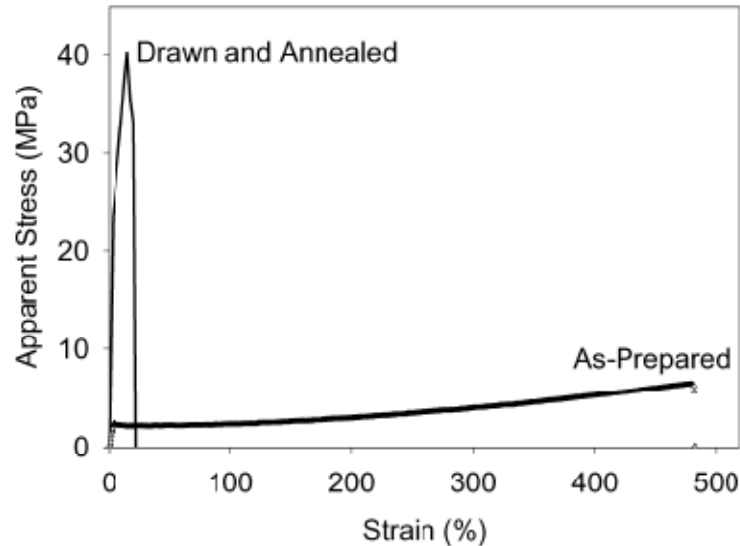


Figure 2. 14:Mechanical property comparison between the as-prepared electrospun PLA10GA90 membrane with that annealed at 90 °C for 20 min under a strain of 450%.¹⁸¹

The effect of post drawing coupled with annealing has also been explored to improve the overall mechanical properties of an electrospun web. Zong *et al* have studied the effect of post stretching and annealing on the mechanical and biodegradation properties electrospun, poly (glycolide-co-lactide), nanofiber membranes¹⁸¹. Crystallinity was found to have increased by annealing at higher temperatures. Crystalline orientation was improved when nanofibers were stretched and then annealed. The improved crystallinity manifested itself in

the form of significantly improved tensile strength and embrittlement of the membrane (evidenced by lower elongation), as shown in Figure 2.14. Increased retention of tensile strength during in-vitro degradation was attributed to the higher crystallinity of the scaffolds. This study is important because it considers the effect of annealing an electrospun mat under conditions of constrained annealing.

The importance of constrained annealing versus unconstrained free annealing has been demonstrated by Bao *et al.*¹⁵⁶. Electrospun PEO webs were thermally annealed near their melting temperature under conditions of constrained annealing (wherein they were held taut on a rigid frame) and unconstrained annealing (freely relaxed state). Mechanical properties showed a difference in trends in both cases, wherein unconstrained samples showed an increase in tensile strength while constrained samples showed an increase in modulus. This was attributed to the fact that constrained annealing induced molecular orientation along constraint direction (resulting in the formation of more-perfect crystal structures with higher crystal orientation), whereas free shrinkage of webs occurred due to the unconstrained heating, resulting in a random morphology.

Thus we observe that post processing thermal annealing of both conventional as well as nanofibrous structures can be used to enhance the mechanical and structural properties of these systems.

2. 4 POST PROCESSING PHOTOTHERMAL ANNEALING

2.4. 1 Surface Plasmon Resonance (SPR) mediated photothermal annealing

Surface plasmons refer to collective charge oscillations that occur at the interface of conductors and dielectrics when the electrons are disturbed from their equilibrium positions^{189, 190}. These disturbances, induced by an electromagnetic wave (e.g., light), cause the free electrons of a metal to coherently oscillate (relative to the lattice of fixed positive ions) at a resonant frequency¹⁹⁰. Because the surface charge oscillations are intimately coupled to electromagnetic fields, surface plasmons are polaritons. They can assume various forms, like freely propagating electron density waves along metal surfaces to localized oscillations on metal nanoparticles. It is this unique property (i.e., their sensitivity to a changing environment at a nanoscale) that enables their use in a variety of applications encompassing nanoscale light manipulation, single molecule biosensors, optical transmission through sub wavelength apertures, optical imaging below imaging limits etc.^{191, 192, 193, 194, 195}.

Considering that the penetration depth of an electromagnetic wave on the surface of a metal is limited, the plasmons caused by surface electrons are most significant, and hence are referred to as surface plasmons. There are two types of surface plasmons; namely propagating surface plasmon (surface plasmon associated with an extended metal surface), and localized surface plasmon (wherein the collective electron oscillation is confined to a finite volume like a metal nanoparticle). The current review will focus on the latter.

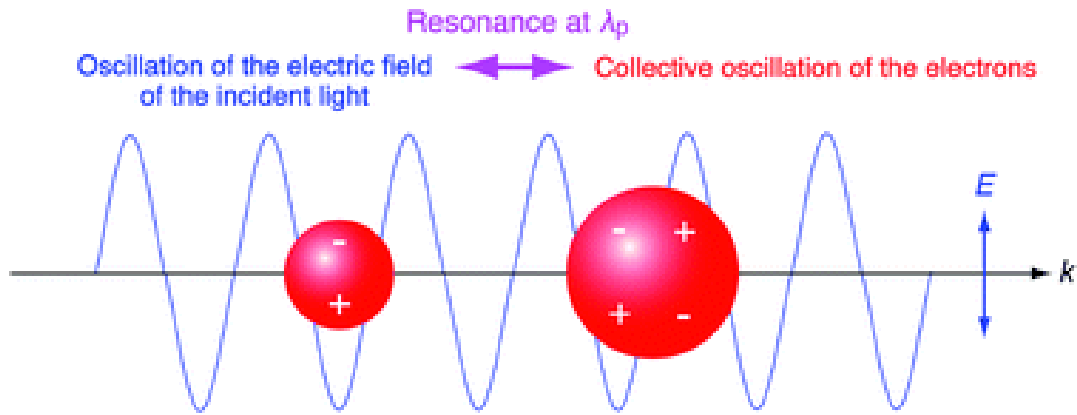


Figure 2. 15:Schematic of plasmon oscillation for a sphere, showing the displacement of the conduction electron charge cloud relative to the nuclei.¹⁹⁶

As shown in Figure 2.15 above, excitement of metal nanoparticles by resonant incident light causes collective electron oscillations to occur. This phenomenon is referred to as a local surface plasmon resonance (SPR). At this resonant frequency, the nanoparticle interacts with the incident light; some of these photons are released with the same frequency in all directions which is referred to as scattering. Simultaneously, some of the photons will also be converted to phonons or lattice vibrations and this process is called absorption¹⁸⁹. Hence, in general it can be observed that the SPR peak for a metal nanoparticle will include both the above mentioned components, with the respective compositions varying with size and shape of a nanoparticle.

The photothermal effect of gold nanoparticles refers to SPR-mediated heating, wherein the incident light energy is converted to heat (phonons). The incident light absorbed by the

nanoparticle generates a non-equilibrium electron distribution that decays by electron scattering ¹. Link *et al* showed that the light induced excitation of metal nanostructures resulted in the formation of a heated electron gas that cools rapidly by exchanging energy with the nanoparticle lattice ². Subsequently, phonon-phonon interactions cause the nanoparticle lattice to exchange its energy with the surrounding medium. This fast energy conversion and dissipation is responsible for the heating of the local environment. It is important to note that though electron phonon interactions can cause electron temperatures to reach elevated temperatures of few thousand kelvins, the change in gold nanoparticle lattice temperatures (in gold colloidal solutions) maybe only a few tens of degrees owing to differences in heat capacity between the two¹⁹⁷. However, the lattice temperatures can be made to rise by usage of excitation pulses of higher intensity (by increasing the energy of the excitation pulse, keeping the same spot size)^{2, 198}. It is this production of heat energy that makes them promising materials for treatment of cancers and tumors by hyperthermia.

The SPR frequency is directly dependant on the size, shape, and composition of the nanoparticles as well as other factors like the dielectric constant of the surrounding medium. Extinction spectra for gold nanoparticles typically show an SPR peak at 520 nm approximately [¹⁹⁹. As the size of the nanoparticle increases, the SPR peak shifts to higher wavelengths (as shown in Figure 2.16, and shifts to the Nearinfrared (NIR) region in case of nanoparticle agglomeration ²⁰⁰. On the other hand, in case of nanorods, the SPR spectrum shows a distinct dependence on the aspect ratio (ratio of the length of the nanorod to its width), with increased aspect ratios leading to significant red shifts. The SPR spectrum is

observed to split into 2 bands as shown in Figure 2.16 (b) - “a prominent long wavelength in the NIR region due to longitudinal oscillation of electrons and a relatively weaker short wavelength band at around 520 nm due to transverse electron oscillations”²⁰⁰. The longitudinal SPR of nanorods can be shifted easily by changing their aspect ratio.

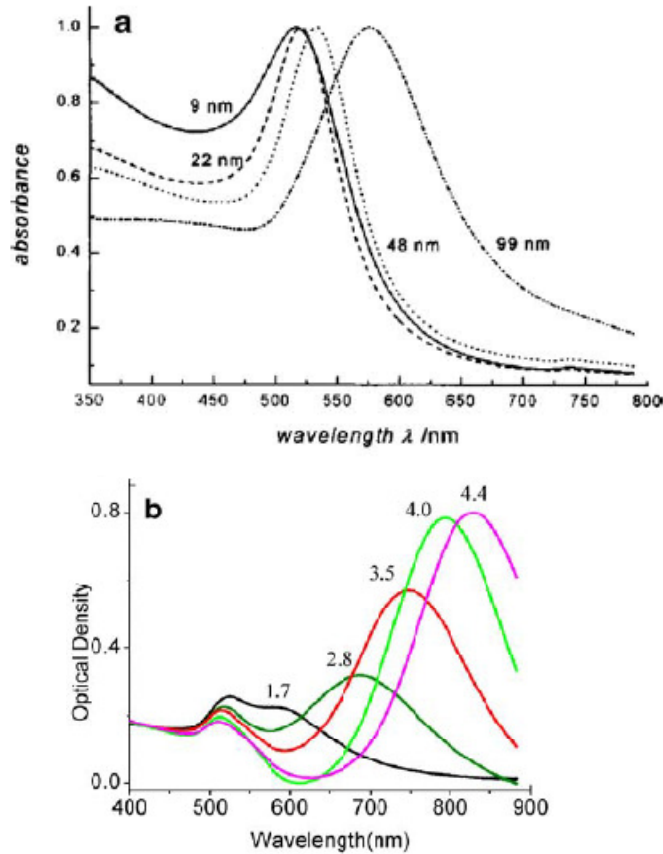


Figure 2. 16: Size, shape, and composition dependence of the surface Plasmon absorption spectrum of plasmonic gold nanostructures. (a) Nanospheres of different sizes; (b) nanorods of different aspect ratios.²⁰⁰.

An important implication of this is the tunability of the nanoparticles to yield different temperatures by the usage of different laser intensities. This concept of localized heating, achieved by localized surface plasmon resonance is of special interest when used for specific application like controlled drug release, therapeutic applications for treatment of tumors, nanoscale sensors and actuators etc ^{201, 202}. The next section will review the various applications wherein the photothermal effect of gold nanoparticles has been utilized, with special emphasis on the usage of this technology in polymer based systems.

2.4. 2 Previous work involving the photothermal effect of gold nanoparticles

Gold nanoparticles find extensive use in biomedical applications as electrochemical sensors and catalysts, wherein they are used in aqueous solutions ^{203, 204, 200}. For instance, Storhoff *et al* used 13 nm gold nanoparticles modified with nucleotides to diagnose errors in polynucleotide sequences based on colorimetric assays ²⁰⁵. An error in the polynucleotide sequence would manifest itself in the form of nanoparticle agglomeration, which caused the solution to turn from red to blue. On the same lines, Nath *et al* have fabricated a biomolecular optical sensor, that provides a colorimetric assay of the concentration of fibrinogen by changes in plasmon resonance intensity (measured by UV-vis) ²⁰⁶.

It was only in the early 2000's that the photothermal effect of gold nanoparticles was used as a source of localized heating. The photothermal therapeutic effect of gold nanocages, nanorods, and nanoshells has been widely studied for the treatment of tumors and cancers ^{192, 207-209}]. The localized heating enables these nanoparticles to be used as hyperthermia agents that are capable of heating tissues to a temperature of 41-47 °C for tens of minutes to kill

tumor cells²¹⁰. Richardson *et al* suggest the use of selective biomolecular linkers to attach nanoparticles to tumor cells, which are destroyed by the heat generated due to the optical stimulation of the nanoparticles²¹¹. Cell destruction was also accelerated by the bubble formation around the nanoparticle that imposes mechanical stresses leading to cell damage. The photothermal effect in these systems was realized by irradiation with short laser pulses that lead to the “rapid heating of the particles and vaporization of a thin layer of fluid surrounding each particle, producing a microscopic version of underwater explosion and cavitation bubble formation”²⁰⁰. It is important to note that this wide-range of work on photothermal heating with nanoparticles primarily utilized aqueous media.

It is only recently that the application of the photothermal effect in solid materials has been explored, primarily in the field of controlled drug delivery. The first description of a polymer based system for the controlled drug delivery using the photothermal effect of nanoparticles appeared in 2000 by Halas *et al*²¹². Essentially, the research involved the usage of a polymer gel incorporated with gold nanoshells to obtain a photothermally modulated drug delivery. Subsequently, Caruso *et al* demonstrated the actuation of polymer based capsules with gold nanoparticles to release lysozyme to destroy *Micrococcus lysodeikticus* bacteria. A schematic representation of the delivery capsule, based on “illuminate and burst” principle is given below in Figure 2.17. An antibody functionalized polymer capsule was bound to the target and the application of laser caused the outer shell of the capsule to heat, resulting in its burst and subsequent of delivery of lysozyme to the localized area. Other modification to the outer

shell was also demonstrated ²¹³. Similar studies based on fabrication of hollow polyelectrolyte capsules have also been carried out using silver nanoparticles ²¹⁴, ²¹³

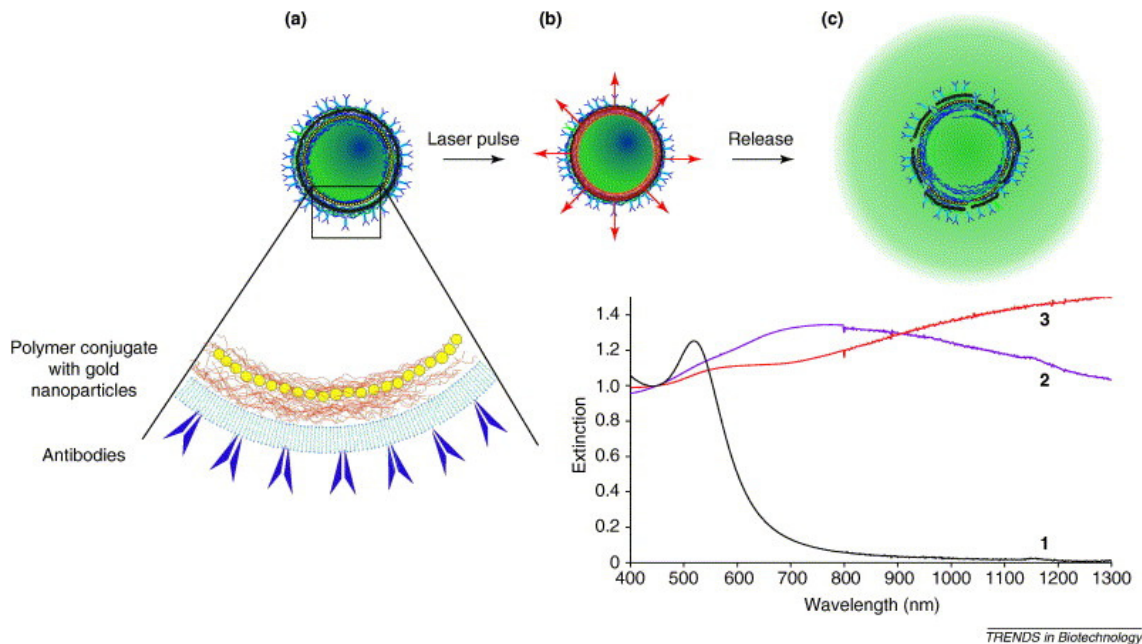


Figure 2. 17:The antibody-functionalized polymer capsule (a) binds to the target (*Micrococcus lysodeikticus*), and application of laser light causes the gold nanoparticles in the shell of the capsule to heat up (b), bursting the container and releasing the therapeutic.²¹³

Studies have been carried out that exploit the photothermal effect of nanoparticles to activate shape memory polymeric (SMP) devices. The usage of light to actuate shape recovery (optically-active SMP) is advantageous considering that it offers the possibility of remote

activation coupled with spatial and temporal control. In this regard, Koerner *et al* hypothesized that the usage of light to optically activate nanoparticles to generate heat would in turn heat the SMP to a temperature greater than its thermal transition and actuate shape recovery³. The photothermal effect is thus utilized to combine the advantages of an optically active SMP with a thermally activated one. This is a mechanism that would offer two distinct advantages in the processing of a SMP. Firstly, the photothermal heating raises the temperature of the polymer locally, thereby offering better control, as against a thermally activated SMP in which the heating from the environment is a bulk effect. Studies suggest that since the polymer is cooled as soon as the light is stopped, multiple intermediate shapes can be obtained between the initial temporary and permanent shapes. This is an important advantage over thermal activation, because the environment has a fixed temperature and the alteration of shape recovery processes cannot be realized without changing the external environmental temperature⁴. Secondly, this method offers the advantage of temperature tunability by adjusting the incident light intensity. An implication of this is that the rise of temperature within the polymer can be tuned optically, to control stress release and shape recovery.

Hribar *et al.* have studied the encapsulation of gold nanorods in a biodegradable and amorphous matrix of SMP poly (tert-butyl acrylate) (PtBA) cross-linked with a poly(b-amino ester)⁵. Exposure to near infrared light (770 nm corresponding to the longitudinal plasmon absorption of nanorods of aspect ratio 3.64 could produce heat in the sample greater than the

glass transition temperature (actuation temperature) and activate the shape recovery. The presence of nanorods did not have any effect on the toxicity of the material.

An optically triggered shape recovery process has been demonstrated by Zhang *et al* using Poly(ϵ -caprolactone) (PCL)-surface functionalized AuNPs , loaded in a thermosensitive shape-memory polymer (SMP) matrix of oligo(ϵ -caprolactone) (bOCL) cross-linked with hexamethylene diisocyanate (HMDI), referred to as XbOCL⁴. SPR-mediated photothermal heating was demonstrated by the study of stepwise contraction as shown in the Figure 2.18 below.

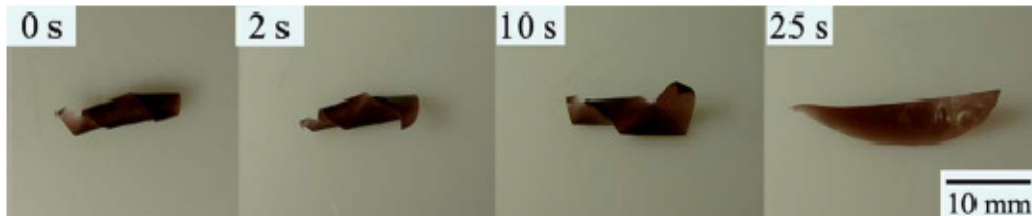


Figure 2. 18: Optically triggered shape recovery of an AuNP-loaded XbOCL film at room temperature (laser at 532 nm, 1.1 W cm²): photographs showing a fast untwisting upon scanning of the laser spot (3 mm) along the film.⁴

This research is particularly important because it shows the actuation of AuNP-loaded composite material under conditions where the environmental temperature (bulk

temperature) was below the actuation temperature. This is because the actuation temperature could be optically photo-induced by a laser, even at different environmental temperatures.

The photothermal effect of gold nanoparticles has also been used in the fabrication of microelectronic devices. Chen *et al* used gold nanoparticles embedded in PMMA matrix to convert photon energy into thermal energy which in turn was used to decompose polymer at the subsurface layer of the nanocomposite film, leading to the formation of microtunnels and reservoirs in the film.

Xu *et al* covalently conjugated gold nanoparticles onto the surface of thiol-functionalized thermosensitive unimolecular micelles to fabricate satellite-like stimuli responsive nanostructures. The resultant nanostructures consisted of gold nanoparticles distributed across the unimolecular micelle surface. The micelles being thermosensitive swelled and shrunk reversibly in response to elevated temperatures resulting from the photothermal effect of the gold nanoparticles. This nanostructure is expected to be used in the fabrication of tunable multifunctionalities and self assemblies, due to its ability to fine tune the spatial distances between the gold nanoparticles ⁶.

Having reviewed the applications of SPR-mediated photothermal heating in solid systems, it is noteworthy to study this effect when incorporated in polymer nanostructures, more specifically electrospun nanofibers. Electrospun nanostructures show a large proportion of void spaces, wherein the effect of photothermal heating can be expected to be more pronounced. The possibility of heating a nanofibrous structure from the inside to outside can

be realized using photothermal heating. A direct impact of this could be obtaining specific morphologies by selective heating of zones within a nanofibrous system that cannot be obtained by conventional heating wherein heat flows from the outside to the interior. In this regard, Maity *et al* fabricated composite polyethylene oxide (PEO) electrospun nanofibers, doped with gold and silver nanoparticles, and irradiated them using a low intensity laser tuned to the SPR ¹. The specificity of the photothermal process was demonstrated by the absence of melting in pure PEO nanofibers as compared against the pronounced complete melting which was observed in the doped PEO nanofibers (Figure 2.19).

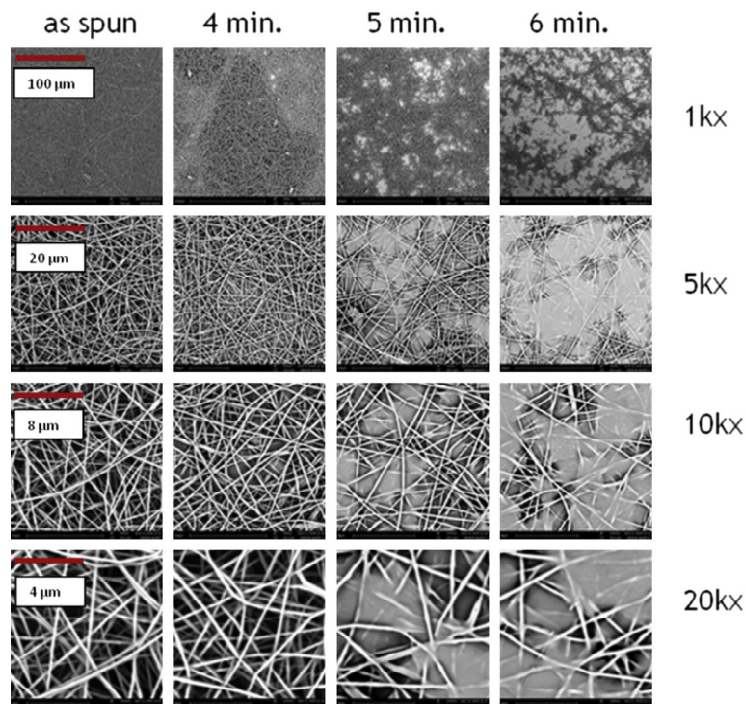


Figure 2. 19:SEM images of the effect of continuous 532 nm light irradiation on AuN1 doped PEO nanofibrous mats (0.15% volume fraction AuN1 batch #1).¹

In the above mentioned research, a very important explanation for thermodynamic changes occurring within the nanofiber when photothermally heated has been discussed. Electrospun structures being predominantly porous (70%) are responsible for relatively slower losses of phonon energy away from the nanoparticle as compared to a liquid medium where heat losses occur in all directions by conduction and convection. The heat flow along the fiber is also hindered by the large aspect ratio of the electrospun nanofiber, which causes significantly higher temperatures to be achieved locally than in a conventional aqueous solution. A notable feature of this work is that it emphasizes the possibility of localized heating by the selective placement of nanoparticles within the electrospun nanofiber.

The use of electrospinning to fabricate nanofibers with localized heating sources (nanoparticles) within them offers immense scope to fabricate systems which have the potential to be used for *in situ* polymer processing, which is currently not fully realized. The current research thus aims to study the effect of photothermally mediated post processing annealing on the mechanical properties of electrospun nanofibrous materials utilizing the photothermal effect of gold nanoparticles.

Chapter 3: RESEARCH OBJECTIVES

3: RESEARCH OBJECTIVES

With overwhelming importance placed on high strength nanocomposites, the development of smart materials and transformational polymer processing is of profound importance. The application of the unique SPR properties of gold nanoparticles (by adding them as dopants) in a polymer environment could potentially enable materials that are thermally processable by traditional annealing means to be now light processable. In applications, that have been hindered by poor mechanical properties of nanofibrous systems (like filtration), high strength rigid materials can be created by in situ polymer processing (annealing) from flexible polymeric materials by SPR mediated annealing. While the ability of gold nanoparticles to produce heat on light activation has been largely studied, very few studies have utilized the photothermal effect of gold nanoparticles in a polymeric environment and more so in a polymer nanofibrous environment. Hence the objective of this research is to provide a thorough understanding of the relationship between the microscopic impacts of the photothermal annealing process (i.e. morphology and crystal structure) on the macroscopic properties of the AuNP containing nanocomposites (mechanical properties). With intent to achieve this goal, a systematic experimental protocol was undertaken and the below mentioned research objectives were finalized:

1) To develop a mechanistic understanding of conventional and photothermal annealing using SPR mediated heating of gold nanospheres in polymer films: Effect on spherulite morphology and polymer crystallinity

Post fabrication annealing is an effective approach to improve and perfect crystal organization in polymer nanocomposites thereby resulting in improvements in bulk properties. Under conventional annealing conditions, the outer surface the polymeric medium heats first, and the heat subsequently transfers to the substrates interior. Using an alternative approach, the incorporation of optically tunable heat sources (gold nanospheres) within the polymer matrix can enable the interior of the medium to heat up first and then transfer the heat away from the nanospheres thereby avoiding potential surface melting. Also, a heterogeneous temperature distribution can be realized by the photothermal annealing, subjecting the sample to a range of temperatures, thereby aiding crystallinity alterations. Hence the objective of this study is to elucidate the spherulite structure and overall crystallinity as a function of annealing temperature and annealing time for both conventional and photothermal annealing.

2) Mechanistic understanding of conventional and SPR mediated photothermal annealing using gold nanospheres in electrospun polymeric nanofibers: Effect on nanofibrous morphology and mechanical properties

Nanofibrous structures offer significant promise for many applications like tissue engineering, drug delivery, energy sources etc. However, they show poor mechanical properties due to lack of interfiber bonding and structural integrity. Post processing annealing can be a useful tool to improve fiber-fiber bonding within the nanofibrous mats by introduction of thermally-induced crosslinking. While direct conventional annealing can

cause large scale bulk melting, destroying the fibrous morphology, the usage of selective annealing by the photothermal heating from randomly distributed gold nanoparticles can improve crosslinking in selective areas within the nanofibrous structure, without causing bulk melting. Hence, this research aims to study the effect of using post processing annealing to improve mechanical properties and at the same time maintaining the nanofibrous morphology of the polymeric system.

3) Study of conventional and photothermal annealing in polymeric films and nanofibers by utilizing the SPR of gold nanorods: Effect on overall crystallinity and morphology

Having studied the photothermal effect of gold nanospheres in film and fiber media, it would be interesting to explore the possibility of utilizing the photothermal effect of gold nanorods. Gold nanorods show a widely tunable longitudinal surface plasmon resonance (LSPR) apart from the transverse surface plasmon resonance (TSPR). The polarization specificity of gold nanorods allows light to be absorbed by LSPR only if the linear polarization direction overlaps the longer axis of the nanorod. When incorporated into electrospun nanofibers, the nanorods align along the fiber axis as against aqueous solutions wherein they are randomly oriented. This direction and polarization specific photothermal effect by using nanorods offers tremendous scope to manipulate the crystallinity within nanocomposite systems by altering crystallinity and morphology by obtaining a heterogenous temperature distribution by changing the aspect ratio of the nanorods.

Chapter 4: THERMAL ANNEALING OF POLYMER NANOCOMPOSITES VIA PHOTOTHERMAL HEATING: EFFECTS ON CRYSTALLINITY AND SPHERULITE MORPHOLOGY

[This chapter was accepted to publish in *Macromolecules* (2013), under *Vidya Viswanath*¹, *Somsubhra Maity*², *Jason R. Bochinski*², *Laura I. Clarke*^{2**} and *Russell E. Gorga*^{1,*}]

¹Fiber and Polymer Science Program, NC State University, Raleigh NC 27695, USA

²Department of Physics, NC State University, Raleigh NC 27695, USA

*Corresponding Author: email: regorga@ncsu.edu (R.E. Gorga)

**Co-Corresponding Author: email: liclarke@ncsu.edu (L.I. Clarke)

CHAPTER 4: Thermal annealing of polymer nanocomposites via photothermal heating: effects on crystallinity and spherulite morphology

Metal nanoparticles embedded within polymeric systems can act as localized heat sources, facilitating in situ polymer processing. When irradiated with light resonant with the nanoparticle's surface plasmon resonance (SPR), a non-equilibrium electron distribution is generated which rapidly transfers energy into the surrounding medium, resulting in a temperature increase in the immediate region around the particle. This work compares the utility of such photothermal heating versus traditional heating in gold nanoparticle/poly(ethylene oxide) nanocomposite films, crystallized from solution and the melt, which are annealed at average sample temperatures above the glass transition and below the melting point. For all temperatures, photothermally annealed samples reached maximum crystallinity and maximum spherulite size faster. Percentage crystallinity change under conventional annealing was analyzed using time-temperature superposition (TTS). Comparison of the TTS data with results from photothermal experiments enabled determination of an "effective dynamic temperature" achieved under photothermal heating which is significantly higher than the average sample temperature. Thus, the heterogeneous temperature distribution created when annealing with the plasmon-mediated photothermal effect represents a unique tool to achieve processing outcomes that are not accessible via traditional annealing.

4. 1 Introduction

The macroscopic properties of semi-crystalline polymers are determined by structural morphology at the molecular level, including crystallinity fraction and crystallite size and structure. Post-fabrication thermal annealing at temperatures significantly above the polymer glass transition T_G (but below the melt temperature T_m) is a straightforward, efficient approach to alter nanoscale molecular organization and realize improvements in bulk properties due to increase in crystal size and perfection.^{177, 178, 186} Annealing increases crystallinity by aiding both nucleation and, particularly importantly, growth of spherulitic superstructures which contain crystal lamellae.¹⁶⁶ Mechanical modulus and overall strength are improved due to reduction in the degree of molecular randomization.^{175, 179} Tuning polymer crystallinity also alters optical,^{211, 215} barrier,²¹⁶ and dielectric^{217, 218} properties, as well as the percolation process in polymer nanocomposites, which are important parameters for applications such as controlled drug delivery,²¹⁹ biosensors,^{220, 221} energy storage devices,²²² and packaging.²²³

Annealing relies on a balance between thermally-induced molecular motion, which re-organizes amorphous material or less-perfect crystals into larger or more perfect crystalline structures and bulk melting, which destroys existing crystalline regions. Ideally, to maximize crystalline fraction, existing highly stable crystalline regions should remain unchanged during the annealing process with only less stable (i.e., lower melting point) crystals or amorphous material (which has dynamics determined by $T - T_g$) experiencing thermally-induced changes. For this reason, the maximum crystallinity achievable is generally obtained by annealing at temperatures well below T_m (i.e., $\sim 10 - 20$ °C).²²⁴ However, from a practical

processing perspective, for lower annealing temperatures, longer times are required to achieve maximum crystallinity. This observation argues that a heterogeneous temperature distribution, where the polymer is simultaneously subjected to a range of temperatures (randomly distributed throughout its interior) may be beneficial in manipulating crystallinity fractions if the average molecular mobility rate can be enhanced while simultaneously preventing bulk melting.

We explore this hypothesis in a metal (gold) nanoparticle: poly (ethylene oxide) (AuNP:PEO) nanocomposite film. Nanoparticles have previously been utilized for a wide range of technological applications including biological spectroscopy and imaging,^{225, 226} biochemical sensors²²⁷, and as nanoscale electronic components.²²⁸⁻²³¹ Here the photothermal property of metal nanoparticles embedded in a material environment is utilized: when the films are uniformly irradiated with visible light, the dilute concentration (1.6 wt %; 0.07 vol. %) of metal nanoparticles provides local nanoscale-sized heat sources from which annealing of the polymer matrix occurs.

The photothermal effect of metal nanoparticles refers to surface plasmon resonance (SPR)-mediated heating, wherein incident light energy is converted to heat.²³² The light absorbed by the nanoparticle generates a non-equilibrium electron distribution (i.e., a surface plasmon) that decays by electron-electron scattering.²³³ The heated electron gas cools rapidly by exchanging energy with the nanoparticle lattice² and the particle temperature increases significantly, leading to heating of the local environment. Under steady-state conditions, a temperature gradient (decaying as $\sim 1/\kappa r$ where κ is the thermal conductivity and r is the

radial distance from the particle)²³⁴⁻²³⁶ is established around each particle which is warmest near the particle and terminates at an average background temperature far from the particle. In the experiments described here, there is no specific interaction between the polymer and the incident light so when the sample is uniformly illuminated, absorption of the light and thereby the photothermal heating, occurs only at particle locations.

The fundamental photothermal properties of metal nanoparticles have been previously scientifically explored and utilized in the aqueous phase,²³⁷⁻²⁴⁴ particularly for hyperthermia-based cancer treatment,^{192, 200, 208-210, 245} and only recently has photothermal heating been applied to a solid medium or for materials processing, with a particular focus on drug delivery and actuation of shape memory polymers.²¹²⁻²¹⁴ Recent published work has utilized photothermal heating to demonstrate wavelength^{246, 247} and polarization-specific²⁴⁸ processing, with the ability to selectively thermally treat one subset of a sample and leave the remainder unchanged. The spatial specificity of particle-based heating enables energy to be deposited inside the polymeric medium as opposed to conventional methods where the outer surface heats first; thus photothermal heating avoids potential surface melting before the interior warms, which is particularly important for thermally-sensitive polymeric nanostructures.

In the current report, we compare the effect of post-fabrication annealing with either photothermal heating or a conventional uniform-temperature approach at several different temperatures and a wide range of times, investigating the resulting structural morphology and crystallinity fraction as observed by polarized optical microscopy (POM), and differential

scanning calorimetry (DSC). These measurements demonstrate that when annealing AuNP:PEO nanocomposites (initially crystallized from either solution phase or melt phase), the maximum crystallinity is achieved much more quickly when heating photothermally. This result is consistent with a heterogeneous temperature distribution within the sample where the regions near a nanoparticle (AuNPs are separated by an average distance of ~248 nm) are much warmer than the average temperature. In the experimental range ($T_m - 35$ °C to $T_m - 5$ °C), our observations from conventional heating followed time-temperature superposition, enabling use of this calibration to estimate the "effective dynamic temperatures" when undergoing photothermal heating, which are significantly greater (~20 °C) than the average sample temperature. Thus, the rate at which crystallinity increases (and thus the time required to anneal) acts as though the sample were at a significantly higher temperature. This effect has special significance at average annealing temperatures close to T_m wherein photothermal annealing was found to produce effective temperatures significantly higher than the melting temperature, enabling higher temperature dynamics within the sample (i.e., a fast increase in crystallinity) without bulk sample melting which would occur under traditional annealing where the entire sample would uniformly experience the higher temperature. This unusual approach to annealing may be particularly useful for nanostructured samples (such as electrospun nanofibers, nanopillars, or nanocolumns), enabling rapid crystallinity enhancement at the molecular scale without destroying desired meso-scale patterning. We utilize a time-temperature superposition model to understand the fundamental response of the polymer to heterogeneous internal temperatures, and estimate an effective temperature near the nanoparticle heaters.

4. 2 Experimental

4.2. 1 Polymer nanocomposite fabrication

Citrate-stabilized gold nanoparticles (AuNP) were synthesized using the Fren's method.²⁴⁹ Aqueous tetrachloroauric (III) acid was reduced with aqueous trisodium citrate solution (both Sigma Aldrich) to obtain spherical gold nanoparticles. Dry polyvinyl pyrrolidone (PVP) (Scientific Polymers Products, Inc.) in an amount equal to that of the tetrachloroauric (III) acid was added to the solution to further stabilize the nanoparticles after synthesis. Freshly prepared nanoparticle solution was drop cast onto copper grids (Ted Pella, PELCO 400 Mesh Grids) for transmission electron microscopy (TEM) (Hitachi HF2000 transmission electron microscope), which showed approximately spherical particles with an average diameter of 24 ± 7 nm (Figure 4.1b). Extinction spectra of the solution were measured with an ultraviolet-visible spectrometer (CARY 50 Scan) to identify the location of the surface plasmon resonance (SPR) as 527 nm (Figure 4.1a), where the spectral location of the 514 nm photothermal excitation source (Coherent Sabre Innova) is indicated by the vertical dotted line.

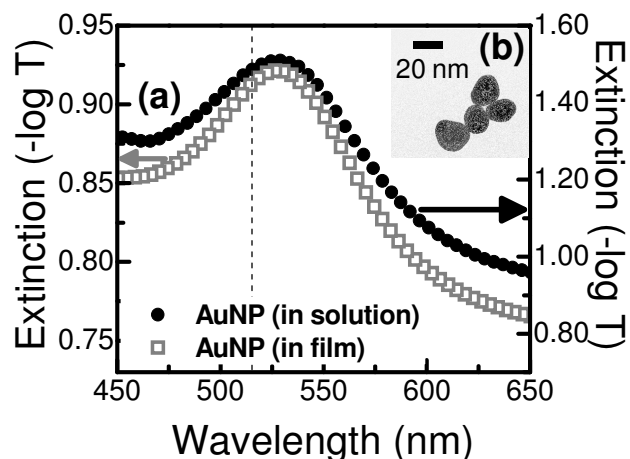


Figure 4. 1:(a) Extinction spectrum of the nanocomposite film (left axis) and the gold nanoparticles (13 wt %) in aqueous solution (right axis), where the broad peak is the spectral location of the surface plasmon resonance (SPR). The vertical dotted line indicates wavelength of the photothermal heating laser. (b) TEM image of neat gold nanoparticles.

For films crystallized from solution, PEO (molecular weight 400,000 g/mol) (Scientific Polymers Products, Inc.) was dissolved in deionized water to obtain a 6 weight percent (wt %) solution, which was combined with aqueous nanoparticle solution and perylene in powder form (Sigma Aldrich # 394475-1G), resulting in 1.6 wt % AuNP:PEO and 0.09 wt % perylene:PEO in the final nanocomposite sample. The perylene additive enables internal temperature monitoring (see section 4.2.2). The mixture was magnetically stirred for 10 hours at room temperature and then spuncast (Laurell Technologies WS-650SZ-6NPP/lite) at 1000 revolutions per minute for 30 seconds on 2.5 cm × 2.5 cm glass slides (Fisherbrand, microscope cover glass 12-540B). Film thickness was measured by an alpha step

profilometer (VeecoDektak Model 150) to be $11 \pm 2 \mu\text{m}$. Extinction measurements (Figure 4.1a) confirm a negligible spectral shift of the AuNP SPR in solution versus in the solid phase, indicating well-dispersed nanoparticles within the final nanocomposite samples. In order to compare annealing effects on melt-crystallized films, initially spin-coated film samples were subsequently heated at $64 \text{ }^\circ\text{C}$ for 15 minutes on a temperature-controlled heating stage and then cooled to room temperature under ambient conditions over 30 minutes ($\sim 1.5 \text{ }^\circ\text{C}/\text{min}$).

4.2. 2 Annealing methods and temperature measurement

Conventionally annealed control samples were created utilizing a programmable, temperature-controlled heated stage (a copper block $2.5 \text{ cm} \times 7.5 \text{ cm} \times 1 \text{ cm}$ attached to a commercial hot plate (VWR 7X7 CER Hotplate)) as shown in Figure 4.2a. Samples were placed on the pre-heated stage and the average temperature (which matched the calibrated set point of the hot plate) was monitored via a fluorescence technique during initial heat up, the active annealing time at a constant temperature, and the cool down to room temperature. Ramping temperature control matched the heating rate for conventionally-heated samples to that which occurred for the photothermally annealed samples. Thus, for instance, for a 20 minute anneal at $50 \text{ }^\circ\text{C}$ (Figure 4.3), the sample was heated at a rate of $2.5 \text{ }^\circ\text{C}/\text{minute}$ for 10 minutes, was held at $50 \text{ }^\circ\text{C}$ for 20 minutes and then cooled at a rate of $1.7 \text{ }^\circ\text{C}/\text{minute}$ for 15 minutes; hence, the temperature cycle matched for both the traditional and the photothermal cases.

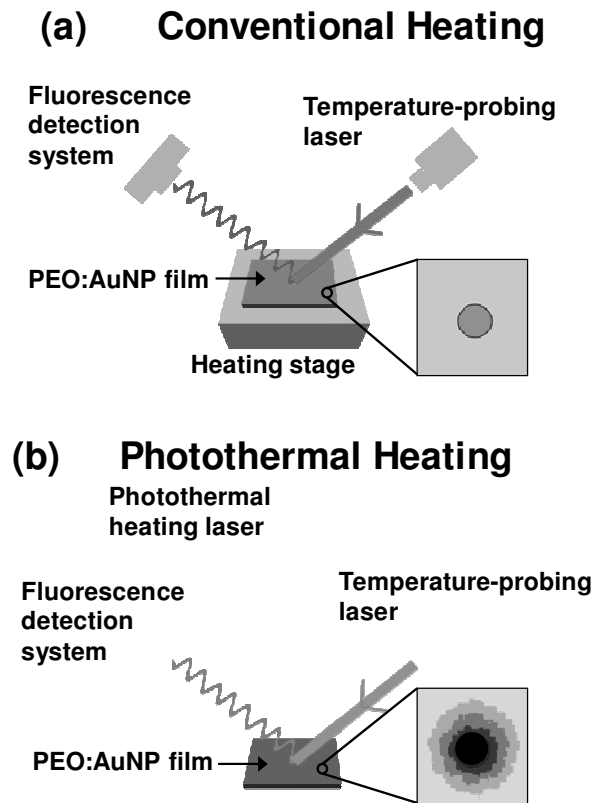


Figure 4. 2: Schematic of (a) conventional and (b) photothermal annealing methods. Magnified diagrams of the nanocomposite sample are shown, schematically showing with a gold nanoparticle remaining inactive in conventionally annealed, uniformly heated samples, and acting as nanoscale-heaters due to SPR-resonant laser exposure in the photothermally annealed samples.

For photothermal annealing, samples were mounted on the same stage at room temperature and irradiated with 514 nm light, expanded to a spot size of 3 cm in diameter as shown in Figure 4.2b. The intensity of the laser beam was determined using a power meter (Coherent Model Powermax PM10). The average temperature of the system was increased by

increasing the intensity of the laser, as discussed in detail previously.²⁴⁷ In this work, light intensities ranging from 0.078 W/cm² to 0.125 W/cm² were utilized, resulting in steady state temperatures of 40 ± 2.4 °C to 60 ± 1.8 °C. Samples that had experienced photothermal annealing cooled significantly more slowly (~3× slower) than conventionally annealed samples after the heating source was removed. In order to exactly match the entire temperature cycle (heating and cooling), the cooling rate for photothermal annealing was matched to that observed under conventional annealing by applying an external cooling fan (Figure 4.3). If photothermally annealed samples are allowed to cool naturally from an annealing temperature of 50 °C, the time to reach maximum crystallinity decreases by ~20 minutes (data not shown) when compared to samples cooled using the external fan (data presented below). Thus matching the entire temperature cycle enables isolation of the effect of the heterogeneous temperature alone; the increase in speed to maximum crystallinity is even greater without this control, as a slower cooling rate (*i.e.*, a longer cooling time) is associated with higher crystallinity.

The solution crystallized films were annealed at 40, 50, and 60 °C by photothermal annealing and at 40, 45, 50, 55, and 60 °C by conventional annealing for times ranging from 4 - 400 minutes. The melt-crystallized films were similarly annealed at 30, 40, 50 and 60 °C for durations ranging from 4 - 160 minutes.

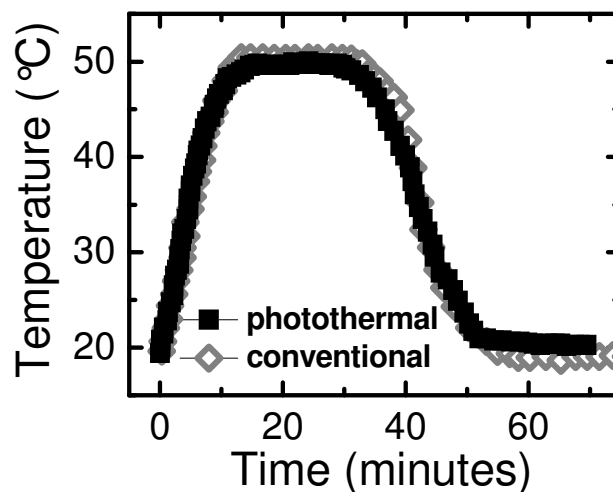


Figure 4. 3: Identical heating and cooling curves (measured via perylene thermometry) for the samples during photothermal or conventional annealing for 15 minute anneal at a temperature of 50 °C.

A non-contact measurement using the fluorescent molecule perylene was used to monitor the average temperature of the nanocomposite.²⁵⁰ Perylene has multiple emission wavelengths and the shape of this emission spectrum changes with temperature (Figure 4.4). In particular, the ratio of the emission intensity at the "trough" at 465 nm to that of the "peak" at 479 nm is essentially linear with temperature (where a calibration curve is determined using conventional heating) as shown in Figure 4.4 (inset); hence, observing the perylene fluorescence provides an in situ probe of temperature, as described previously.²⁴⁷

A 405 nm, 5 mW continuous-wave violet diode laser was amplitude-modulated at a rate of 2 kHz, expanded to a spot size of 0.5 cm diameter, and aligned on the sample spatially

overlapping the photothermal heating laser. The corresponding fluorescence spectrum was imaged onto the entrance slit of a double-grating scanning monochromator (SPEX 1680B) with a side-on photomultiplier tube (PMT) detector (Hamamatsu 931B) at the exit port. The amplified PMT output was photon-counted (Stanford Research Systems SR400), with a corresponding background correction.

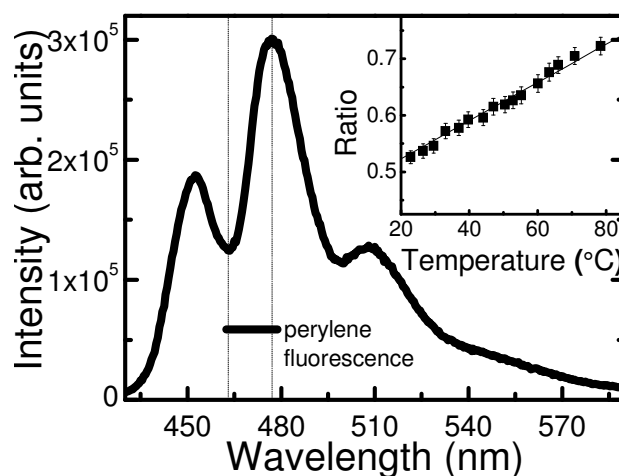


Figure 4. 4: Full emission spectrum of embedded perylene at 25 °C; vertical dashed lines indicate spectral locations of the peak and trough used for temperature measurement. Inset: Ratio of perylene emission intensity under conventional heating enables calibration of the fluorescence-temperature relationship.

Perylene is dispersed uniformly at a dilute level (0.09 wt %, 0.02 vol. %) within the polymer nanocomposite. Because of the large average distance between gold nanoparticles ~248 nm

(derived from a polymer: nanoparticle concentration calculation), the majority of the perylene molecules are located far from a nanoparticle. This result can be demonstrated from a simple model: dividing the average distance between two particles into three equal radial segments, the total volume of material associated with each particle (i.e., a sphere of radius 124 nm with a total volume of $7.99 \times 10^{-21} \text{ m}^3$) divides into a sphere closest to the sample with radius 41 nm (volume $2.88 \times 10^{-22} \text{ m}^3$), a spherical shell with radii between 41 and 82 nm (volume $2.02 \times 10^{-21} \text{ m}^3$), and a second spherical shell with radii between 82 and 124 nm (volume $5.68 \times 10^{-21} \text{ m}^3$). The warmest regions of the sample will be within the spheres most closely surrounding the nanoparticle which represent only 3.6% of the total sample volume. Assuming the perylene molecules are uniformly-distributed, this model indicates that the warmest regions will contribute less than 4% of the measured perylene signal. Moreover, the overall perylene quantum efficiency actually decreases by ~20% with increasing temperature over the range employed here (i.e., the total fluorescence will have an even smaller contribution from the warmest regions). Thus it can be inferred that the perylene measures the “average” temperature of the system with only a ~3% contribution coming from the hottest regions nearest to the nanoparticles.²³⁶

4.2. 3 Sample characterization

Polarized optical microscopy (POM) was employed to study spherulite morphology in the polymer nanocomposite films. Using a Nikon Eclipse 50i POL Optical Microscope at 100x and 400x magnification, micrographs of the control and annealed films were captured with a CCIDIRIS/RGB color video camera (Sony Corporation), using crossed polarizers and a first

order wave plate ($\lambda = 530$ nm). Due to the anisotropy of the spherulite, when viewing a sample under crossed polarized light, the spherulitic structure (chains of the crystallites oriented either perpendicular or parallel to the spherulite radius) results in a specific arrangement of the optical indices. This results in the formation of a Maltese cross pattern which arises from the interaction of polarized light with the crystallites within the sample.²⁵¹ The light emerging from a first order wave plate remains linearly polarized, yet is retarded by 530 nm, which can be used to calculate the birefringence, but is utilized here to provide an additional means of contrast (due to the color gradient) between adjacent spherulites during image analysis. Difference in color of polarized images can be attributed to birefringence changes arising from differences in the surface structure/thicknesses of the films.

Spherulite density (number of spherulites per volume) was calculated by counting the number of spherulites per unit area from the polarized optical micrographs and accounting for the known film thickness. Similar approaches to determine nucleation densities have been previously reported.²⁵²⁻²⁵⁴ Images were processed using the split channel mode to separate the red, green and blue components (using the NIH ImageJ software). The component with the best contrast showing clearly discernible spherulite boundaries was selected and spherulite number was determined using the point selector tool to prevent repetitive counting. At least 2 separate images were analyzed for each annealing condition. Quantitative analysis was not performed for conditions where spherulite boundaries were not discernible due to morphology changes (e.g., such as the transformation to a hedritic structure).

Differential scanning calorimetry (DSC) was performed using a Perkin Elmer Diamond DSC-7 to determine the crystalline fraction. The specimens were subjected to heating scans from 25 to 80 °C at a heating rate of 5 °C/minute (first heating cycle). Pyris software was used to analyze the DSC data. Overall sample crystallinity percentage (% X_c) was calculated by: % X_c = ($\Delta H_m / \Delta H_m^*$) × 100, where ΔH_m and ΔH_m^* are the melting enthalpies for the specimen and 100% crystalline PEO, respectively ($\Delta H_m^* = 213.7 \text{ J/g}$).²⁵⁵

4. 3 Results and discussion

4.3. 1 Effect of presence of nanoparticles and a brief background

The AuNP:PEO nanocomposites overall exhibited a similar range of crystallinity values as neat PEO films, indicating that the addition of a low concentration of particles did not significantly enhance or inhibit the ability of PEO to crystallize. As originally fabricated, AuNP:PEO films have a crystallinity fraction of 58 ± 1%, comparable with the value of 60 ± 1% in neat PEO. No pronounced change in peak melt temperatures (T_m) was observed, with T_m in the range of 64 - 67 °C for both neat PEO and composite films. These crystallinity and T_m values are consistent with those reported for similar systems of PEO composites with gold nanoparticles.²⁵⁶ The maximum crystallinity observed in the PEO composite films used in this study was ~70%, consistent with expectations for an entangled semi-crystalline PEO obtained in previous studies.^{257, 258}

The nanocomposite films revealed the distinct presence of spherulitic morphology as shown in the optical microscopy images in the figures throughout this work. Spherulites are spherical structures formed during crystallization of polymers under quiescent conditions,

which include radial protrusions that alternate between crystalline regions (where lamellae are the dominant structure) and regions of amorphous chains. After nucleation, lamellae grow radially outward from the nucleation site but the entanglement of the polymer chains traps amorphous materials between these crystalline regions. Post-processing annealing of films has been associated with both new nucleation/growth and growth of existing spherulites.¹⁰ Annealing increases the size of the spherulites by providing the thermal energy necessary for continued radial growth of lamellae.^{259, 260} Previous studies have demonstrated that annealing PEO films at temperatures close to the melt temperature (for sufficient time) results in crystal melting and subsequent recrystallization.^{171, 172} This overt melting process produces a new crystallization pattern determined by the conditions present during recrystallization; in this work, melting and recrystallization resulted in a decrease in crystallinity fraction.

Since irradiated gold nanoparticles provide the source of heat in photothermal annealing, efforts were taken to ensure that the nanoparticles were dispersed uniformly throughout the nanocomposite film. When nanoparticle aggregation occurs, the surface plasmon resonance shifts to redder (i.e., longer) wavelengths.²⁶¹ Figure 4.1 compares the SPR for nanoparticles well-dispersed in solution and in the polymer composite, where the similar spectral location of SPR indicates that the nanoparticles remain isolated and do not aggregate within the solid film. PEO lamellae in spherulitic morphologies possess thickness of 10 - 15 nm,^{262, 263} whereas the characteristic size of the nanospheres utilized in this work is 24 ± 7 nm. Thus, by steric hindrance it is expected that the nanoparticles remain in the amorphous regions of the

semi-crystalline polymer nanocomposite system. Such locating of particles may assist in enhancing crystallization by usefully generating the photothermal heat selectively in the amorphous regions.

4.3. 2 Annealing of solution crystallized films

Figure 4.5a displays the change in crystallinity in AuNP:PEO nanocomposite films as a function of annealing time at 50 °C (i.e., $\sim T_m - 15$ °C) under uniform heating (e.g., the conventional approach) versus heterogeneous heating via the photothermal effect of the embedded gold nanoparticles. In both cases, the crystallinity was found to increase initially and then decrease at longer durations of annealing. This general trend can be explained as follows. At short times, the dominant effect is the conversion of amorphous or mesophase material to crystalline and growth of spherulites (discussed below); however, at longer times, crystal melting and recrystallization occur. Recrystallization after melting results in lower overall crystallinity as the recrystallization process occurs in a completely different environment than the initial condition (i.e., crystal formation as solvent is lost during initial film fabrication). As discussed below, after melting, many small spherulites are observed. At lower processing temperature (where bulk melting cannot occur during the timescale of the experiment, < 35 °C, data not shown) the crystallinity fraction saturates at long times. Reduced crystallinity at longer annealing times has been previously reported for other semi-crystalline polymeric systems.^{264, 265}

The perfection/growth of crystals at short times and overt melting at longer times is one example of the effect of time-temperature superposition where a barrier-limited process (here both reorientation of segments within amorphous material to enable crystal formation and melting) can occur either due to increased temperature or increased time.²⁶⁶

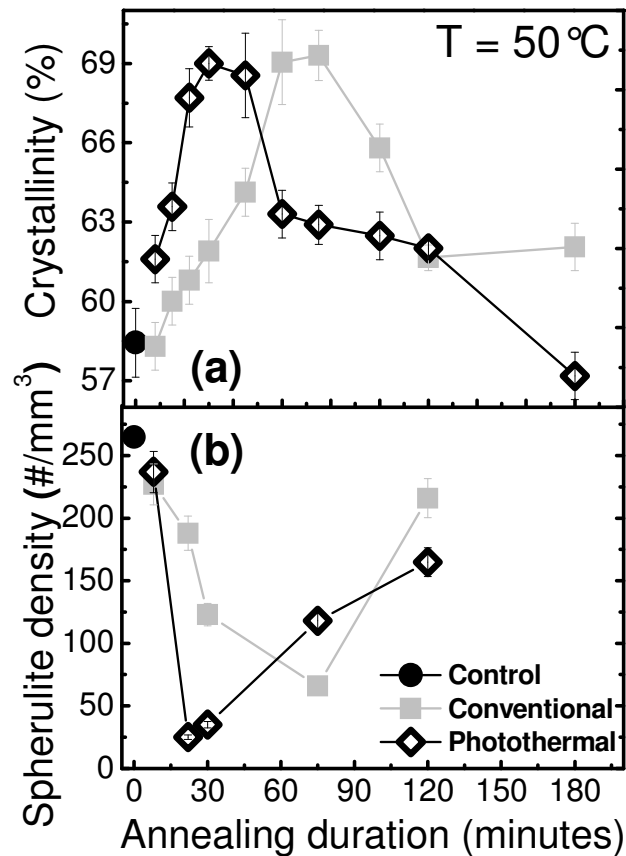


Figure 4. 5: Sample crystallinity measured by DSC as a function of annealing time at 50 °C (i.e., at $\sim T_m - 15\text{ }^{\circ}\text{C}$) for films of PEO doped with 1.6 wt % of gold nanoparticles annealed via photothermal (open diamonds) or conventional (grey squares) methods. The control is an untreated sample as fabricated. (b) Spherulite density (number of spherulites per unit volume) as a function of annealing time.

Though the bulk average temperature is the same under both annealing protocols and the general shape of the response is similar, the photothermally annealed films show a much faster increase in crystallinity (maximum value at 33 minutes) as compared to conventionally annealed films (maximum value at ~ 68 minutes). Thus, the heterogeneous temperature distribution results in a faster response.

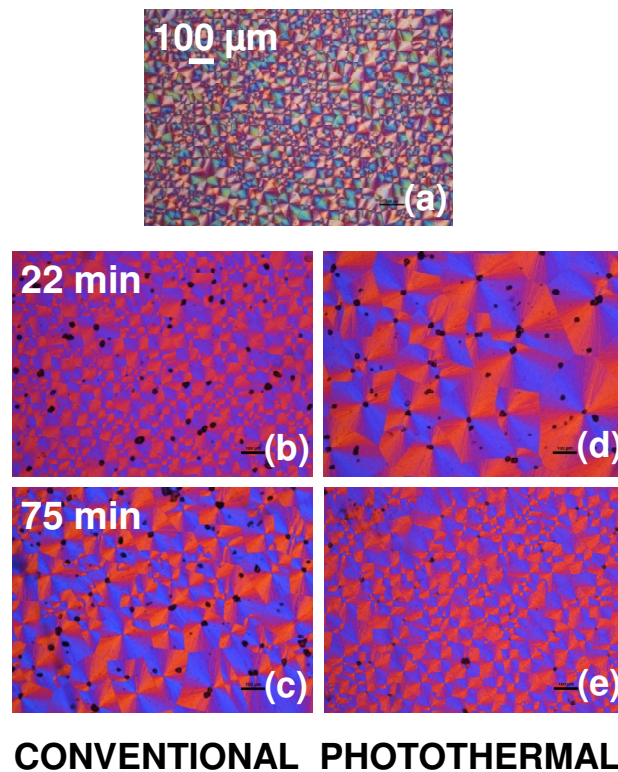


Figure 4. 6: Cross-polarized optical images of (a) as spun AuNP:PEO films; after conventional annealing for (b) 22 and (c) 75 minutes; and after photothermal annealing for (d) 22 and (e) 75 minutes at 50 °C.

The increase in crystallinity can be correlated with changes in spherulite size by imaging the spherulites as shown in Figure 4.6. Spherulite density (i.e., number per volume) from analysis of different images taken as a function of time is shown in Figure 4.5b. Spherulite density is a minimum (i.e., the spherulite size is a maximum) at similar annealing times as when the crystallinity fraction is maximized. The largest spherulites are obtained for significantly shorter annealing times (22 minutes) under photothermal annealing as compared to the traditional approach (>75 minutes). Following the trends shown in the crystallinity fraction, at long times the spherulite diameter decreases as melting destroys the existing structure and new smaller spherulites are nucleated from the melt upon cooling to room temperature. This decrease in spherulite size (associated with melting) does not occur when annealing at low temperatures (e.g., 30 °C for 2700 minutes) where melting cannot occur during the timescale of the experiment.

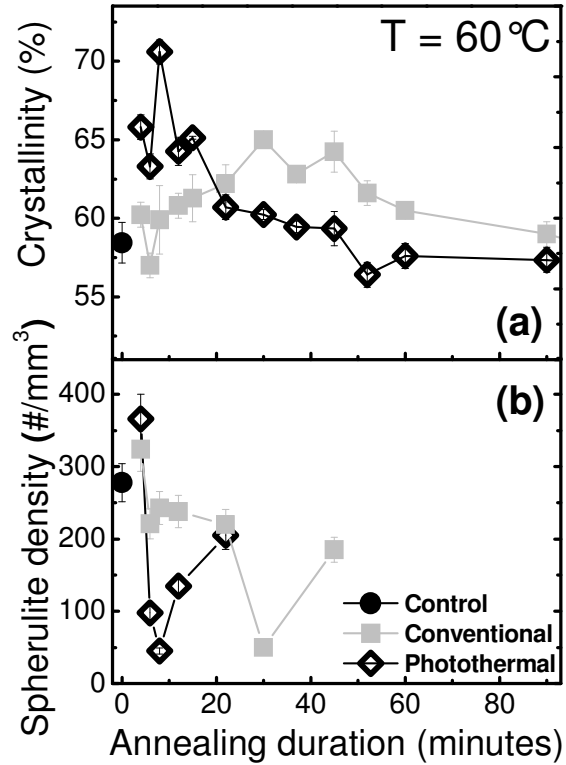


Figure 4. 7:(a) Crystallinity and (b) spherulite density as a function of annealing duration for AuNP:PEO films post-processed via conventional and photothermal heating at 60 °C.

Figure 4.7 shows the effect of annealing at 60 °C (i.e., $\sim T_m - 5$ °C). The general trends (crystallinity increase and then decrease) shown at lower temperatures similarly occur but at shorter times. Furthermore, photothermally annealed samples achieve overall higher crystallinity values ($71 \pm 2\%$) than results from conventionally annealing ($65 \pm 1\%$) in approximately 20% of the time (8 minutes versus 37 minutes). Again, spherulite density from optical images as a function of annealing time shows similar trends as at lower temperatures

(Figure 4.8). While it takes 30 minutes of conventional annealing to produce the largest spherulites (Figure 4.8c), it takes only 8 minutes to achieve the largest spherulite size (corresponding to maximum crystallinity) via photothermal annealing (Figure 4.8e).

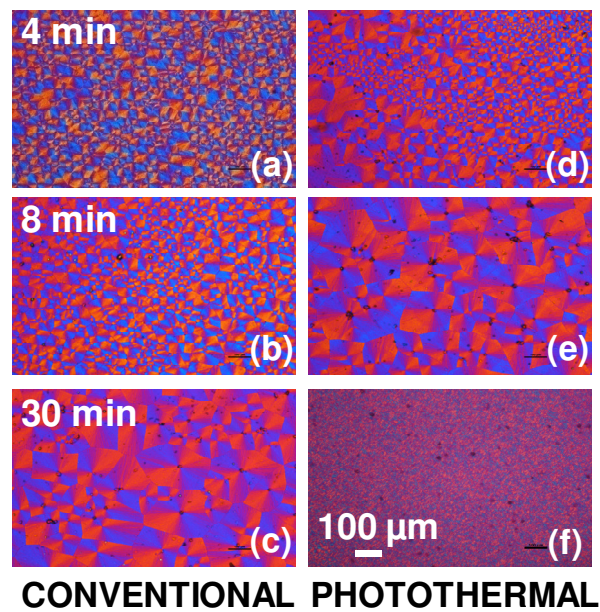


Figure 4. 8:Cross-polarized optical images of the AuNP:PEO films after annealing at 60 °C for 4, 8, and 30 minutes conventionally (a), (b), (c) and photothermally (d), (e), (f), respectively.

At longer annealing times at 60 °C (>20 minutes for photothermal and >45 minutes for conventional), significant morphological changes were observed (Figure 4.9): instead of spherulites of decreasing size (as the maximum in crystallinity has already been achieved), an intermediate spherulite-hedrite morphology was observed. Note: spherulite densities are not reported once a disruption of the spherulite morphology is observed. Hedritic morphology has previously been reported in PEO during annealing studies.^{10, 267-270} Hedrites are composed of a number of lamellae joined together along a common line or, more often, along a common plane. Whereas hedrites are mainly layered lamellar structures grown from a central screw dislocation, spherulites are lamellar structures that grow in three dimensions.²⁶⁸

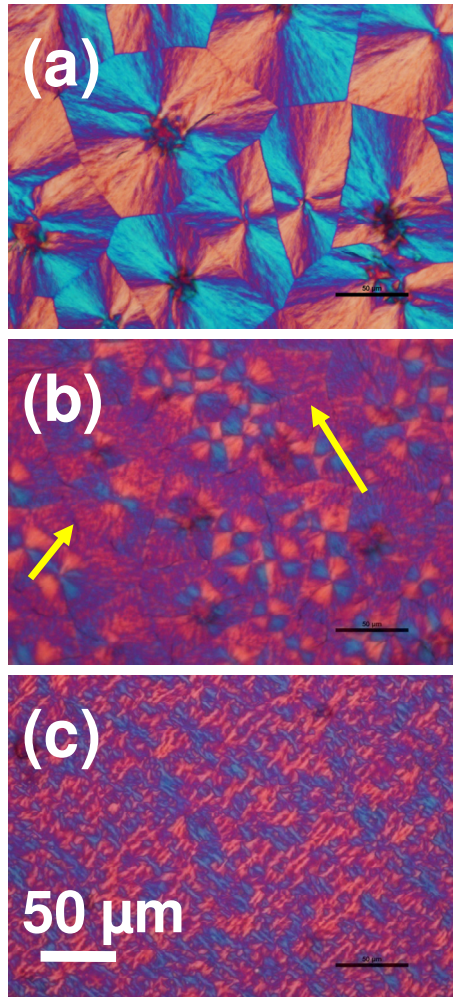


Figure 4. 9: Cross-polarized optical images of the AuNP:PEO films after photothermal annealing at 60 °C for (a) 8 minutes, (b) 22 minutes, and (c) 30 minutes reveal the transition from spherulitic to hedritic morphology.

Figure 4.9a is an image of spherulitic structures (shown at the peak of the crystallinity after an 8 minutes photothermal anneal at 60 °C), which develops into an intermediate semi-hedritic morphology after a 22 minutes (Figure 4.9b), until (after 30 minutes) becoming a

hedritic structure with a complete absence of spherulites and showing the presence of internal dominant lamellar structure (Figure 4.9c). Intermittent featureless patches outside of the hedritic structure are observed (Figure 4.9b), indicative of annealing-induced partial melting which is responsible for thermal etching of the previously formed spherulitic structure, thereby producing a hedrite with underlying lamellae exposed. These images support the hypothesis that the samples melt given sufficient annealing time with complete destruction of the spherulites initially formed from solution crystallization and subsequently enhanced by short-time annealing.

Both conventional and photothermal annealed samples showed the hedritic morphology with the process arising at earlier annealing times under photothermal heating. Thus such morphology is a natural result of annealing PEO near T_m and as with other crystallinity changes, simply occurs more rapidly under photothermal heating. This argues that the innate crystallization process in PEO is unchanged with the addition of the AuNP and the resultant morphology achieved via photothermal annealing is similar to that obtained by conventional heating for longer times. The only exception to this rule is the higher crystallinity fraction obtained at $T_m - 5$ °C via photothermal heating, which appears to be unachievable by conventional heating at any time.

Table 4.1 summarizes the annealing time required to obtain maximum crystallinity (from DSC) and the average annealing time at which the largest spherulites (minimum spherulite density) are obtained (from polarized light microscopy) for different conventional (5) and photothermal (3) annealing temperatures. From this data it is clear that photothermal

annealing decreases the annealing time necessary to achieve the maximize crystallinity (and minimum spherulite density). Further for the lowest and highest annealing temperatures reported (40 and 60 °C, respectively) there is a statistically significant increase (albeit small) in the crystallinity for the samples annealed photothermally.

Table 4. 1 Annealing time to maximum crystallinity and to obtain largest spherulites (minimum spherulite density) in solution cast films for different annealing temperatures using conventional or photothermal annealing.

Annealing temperature (°C)	Annealing technique	Annealing time to maximum crystallinity (minutes)	Average time to minimum spherulite density (minutes)	Maximum crystallinity (%)
40	Conventional	200 ± 14	180 ± 20	64 ± 1
	Photothermal	55 ± 7	45 ± 15	68 ± 1
45	Conventional	180 ± 14	180 ± 14	67 ± 1
50	Conventional	68 ± 11	75 ± 15	69 ± 1
	Photothermal	33 ± 16	22 ± 8	69 ± 1
55	Conventional	55 ± 7	60 ± 15	70 ± 2
60	Conventional	37 ± 10	30 ± 7	65 ± 1
	Photothermal	8 ± 4	8 ± 4	71 ± 2

4.3. 3 Annealing of melt-crystallized films

Figure 4.10 shows the effect of annealing films crystallized from the melt (solution cast films heated to 65 °C for 15 minutes (which results in complete melting) and then cooled to room

temperature under ambient conditions (~30 minute cool) at 60 °C. Melt-crystallized samples had a lower crystallinity fraction ($54 \pm 1\%$) than solution crystallized films ($58 \pm 1\%$) and, as fabricated, showed no clear evidence of either hedrite or spherulite morphology, although lamella-like features may be discernible (Figure 10a).

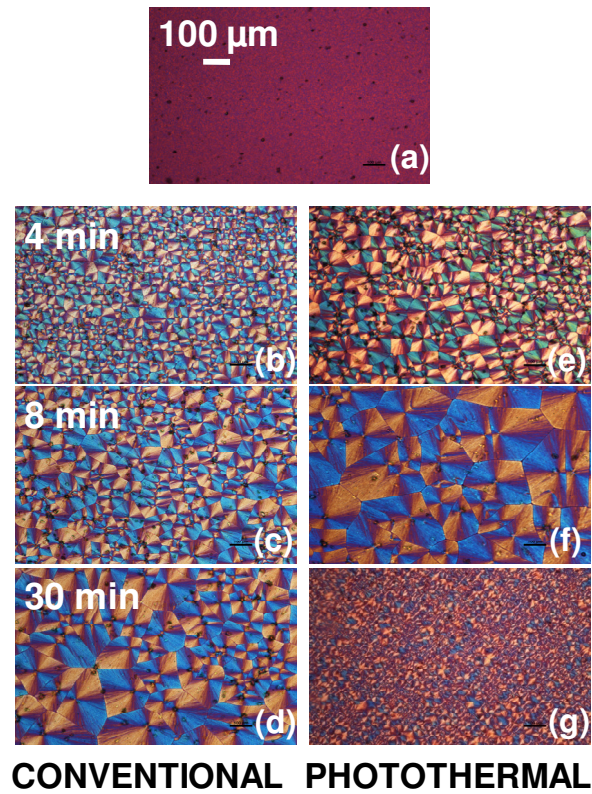


Figure 4. 10: Cross-polarized optical images of (a) melt-crystallized AuNP:PEO film after conventional annealing at 60 °C for 4, 8, and 30 minutes conventionally (b), (c), (d) and photothermally (e), (f), (g), respectively.

Melt-crystallized films annealed at 60 °C show the development of crystalline structure, marked by well-formed spherulites as illustrated in Figure 4.10. Photothermally annealed samples revealed a faster development of spherulitic morphology, producing the largest spherulites at 8 minutes of annealing, as compared to conventional annealing where the largest spherulites occurred for 30 minute times (as summarized in Figure 4.11b). Similar to solution crystallized films, at shorter annealing times, as the spherulites begin to grow the overall crystallinity increases, as shown in Figure 4.11a for the melt-crystallized films. At longer durations, melting occurs, which results in the nucleation and growth of new, smaller, spherulites, thereby resulting in a decrease in crystallinity. These trends are observed at each annealing temperature investigated, presented in Table 2. As temperature increases, the annealing time required to reach maximum crystallinity decreases. The biggest spherulites (i.e. minimum spherulite density) occur at the same annealing time (for a given temperature) thereby confirming that the resultant crystallinity increase observed is due to the increase in spherulite size.

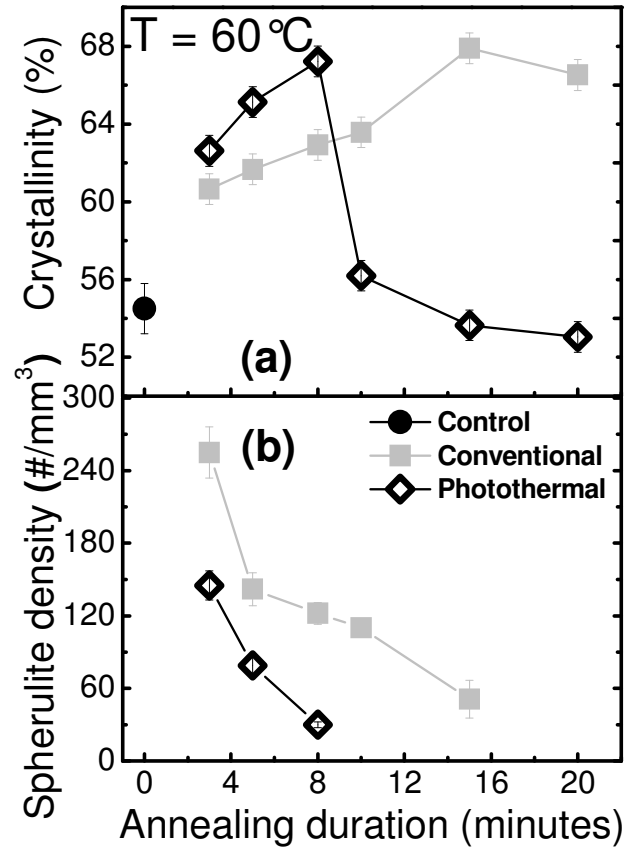


Figure 4. 11:Crystallinity and (b) Spherulite density as a function of annealing time for AuNP: PEO melt-crystallized films annealed by conventional and photothermal heating at 60 °C. Quantitative analysis was not performed for conditions where spherulite boundaries were not discernible due to morphology changes (e.g., such as the transformation to a hedritic structure) (see Figure 10g).

As summarized in Figures 4.11 and Table 2, the same trends observed for solution-crystallized samples are present in melt-crystallized samples. Photothermal heating increases the speed to the maximum crystallinity. Comparing the two types of films, the maximum crystallinity achievable at a given temperature was independent of sample type, and

presumably set by the degree of entanglement within PEO of this molecular weight. However, it is germane to note, films crystallized from the melt reach the same maximum level of crystallinity more rapidly than solution-crystallized films. This may be due to steric effects: the large initial spherulite size in solution-crystallized samples hinders further spherulite growth due impingement of neighboring spherulites; in contrast, the almost featureless morphology of the melt-crystallize films enables rapid initial growth before spherulite interactions become significant.

Table 4. 2 Annealing time to maximum crystallinity and to obtain largest spherulites (minimum spherulite density) in films crystallized from the melt at different annealing temperatures using conventional and photothermal annealing.

Annealing temperature (°C)	Annealing technique	Annealing time to maximum crystallinity (minutes)	Average time to minimum spherulite density (minutes)	Maximum Crystallinity (%)
30	Conventional	120 ± 41	150 ± 30	64 ± 1
	Photothermal	90 ± 31	90 ± 30	65 ± 1
40	Conventional	75 ± 10	90 ± 15	69 ± 1
	Photothermal	30 ± 21	60 ± 15	66 ± 1
50	Conventional	30 ± 10	30 ± 15	67 ± 1
	Photothermal	15 ± 14	15 ± 7	68 ± 1
60	Conventional	15 ± 2	15 ± 5	68 ± 1
	Photothermal	8 ± 3	8 ± 3	67 ± 1

4.3. 4 Time temperature superposition

For annealing studies in general and this work in particular, the interplay between time and temperature lead to the point of sample maximum crystallinity fraction. Specifically, the needed annealing time decreases with increasing temperature. Recently time-temperature superposition has been applied to conventional polymer annealing,²⁷¹ where data at different temperatures was compressed into a master curve by shifting along the time axis. The time to reach maximum crystallinity at a given temperature, normalized by the same quantity at a single low reference temperature, was defined as a shift factor and the scaling of such as a function of temperature was utilized to determine a characteristic barrier in the system. Because the effect of plasmonic heating is heterogeneous, there is no single temperature that describes the photothermal annealing process; however by comparing photothermal shift factors to those from conventional heating, an "effective dynamic temperature" can be determined. That is, the system responds at a rate that is consistent with the effective dynamic temperature. This enables quantification of the effect of photothermal heating at the molecular scale.

Time-temperature superposition is associated with thermally-activated processes where rates are generally exponentially-dependent on the ratio of barrier height to temperature. Thus, motion or relaxation is possible at any temperature: one must simply wait long enough for a thermal fluctuation that overcomes the average barrier height in the system. In photothermal heating, only a small fraction of the sample, near the particle, experiences the higher temperature. However, because thermally-activated processes are exponentially dependent on temperature, the effect of this minute fraction is observable, while the remainder of the

sample is relatively cool. This heterogeneous heating approach appears to prevent bulk melting while enhancing the motion of amorphous or metaphase material, enabling it to crystallize; the location of the particles (primarily in the amorphous region due to steric effects) may enhance this effect. Our analysis below focuses on this simple model of thermal activation with a distribution of barriers.

To determine the shift factors (utilizing conventional heating where the temperature is known throughout the sample) the lowest available temperature was utilized as the reference value (40 °C (30 °C) for solution (melt) crystallized samples since it is closest experimental temperature to the PEO glass transition temperature. (Experiments on solution-crystallized samples at 30 °C were inconclusive at times up to 2000 minutes.) The shift factor a_T , defined as the ratio of the experimental time to achieve maximum crystallinity to the same quantity at the reference temperature is defined in Eq. (4.1) as:

$$\ln(a_T) = A + \frac{E_a}{kT} \quad (4.1)$$

where the underlying dynamics in the system are assumed to fit a simple Arrhenius equation. In Eq. (4.1), E_a is the effective activation energy (average barrier height), k is the Boltzmann constant, T is the temperature and $A = -E_a/kT_{\text{ref}}$ is a dimensionless constant where T_{ref} is the reference temperature.²⁷² Plots of $\ln(a_T)$ versus $1/T$ for conventional heating are shown in Figure 4.12a (b) for solution (melt) crystallized films (filled squares). Over this temperature range, the Arrhenius fit is sufficient and produces a linear relationship between (a_T) and $1/T$ (where $E_a = 18.8$ kcal/mol and $A = -30.29$ for solution crystallized films; $E_a = 14.3$ kcal/mol

and $A = -24.16$ for melt-crystallized films). Observed shift factors for photothermal heating are also shown (open diamonds) initially plotted at the background temperature. In fact, as discussed above, the background temperature is not the effective temperature for photothermal annealing, as evidenced by the lower than expected time to maximum crystallinity, and thus *a priori*, this initial placement is incorrect. While the annealing process is the same (as argued above) in both cases (and thus a_T should be the same at a given temperature), the effective temperature at which the photothermal process occurs is higher than the average temperature experienced by both samples. Thus, by examining Figure 4.12, the actual effective temperature (the temperature at which the system is responding) can be determined by shifting the photothermal data onto the calibration curve determined by the conventional data; that is the photothermal data (open black diamonds) are translated horizontally until they fall on the linear regression curve (open grey diamonds). This calibration enables quantification of an effective dynamic temperature which is discussed below and depicted in Figure 4.13.

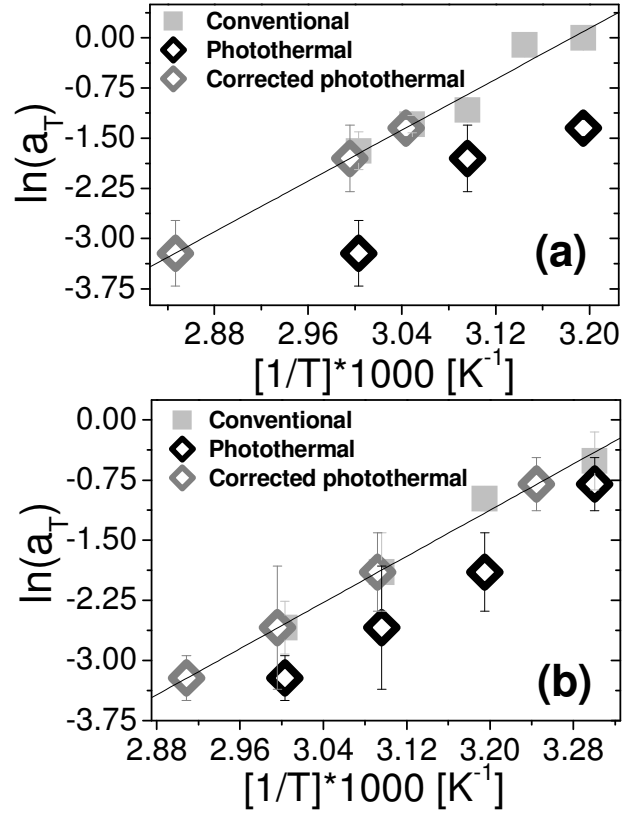


Figure 4. 12: Logarithm of shift factor as a function of reciprocal temperature for films crystallized from (a) solution and (b) the melt for conventional or photothermal annealing. The solid lines show a linear regression through the conventional annealing data.

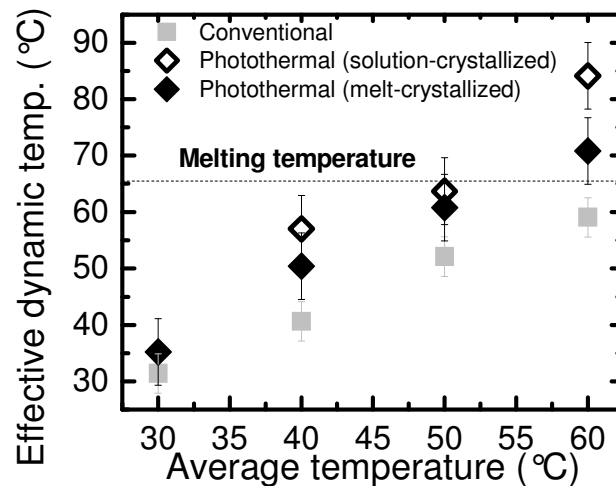


Figure 4. 13: Effective dynamic temperature for AuNP: PEO films crystallized from either solution or melt and annealed at the average temperature.

Figure 4.13 shows the effective dynamic temperature obtained from time-temperature superposition plotted as a function of the average temperature. To reiterate, the average temperature is the temperature present at all locations under conventional annealing and far from the gold nanoparticles under photothermal heating. Even though the time-temperature superposition analysis resulted in a slightly different average barrier value (E_a) in the melt-crystallized and solution-crystallized cases (which reflects the different steric environments), the effective dynamic temperatures in the two cases are similar. Thus, regardless of the specific morphology, the PEO responded at a rate that was consistent with a temperature 5 - 25 °C higher than the background. For instance, for samples annealed photothermally at an average temperature of 50 °C, the time to reach maximum crystallinity indicates that the

effective dynamic temperature is approximately 65 °C (for both solution and melt-crystallized samples). It is important to note that this cannot be achieved by conventional annealing, since annealing at 65 °C ($\sim T_m$) would result in complete melting of the crystal structure and subsequent melt crystallization upon cooling (similar to what is seen in the melt-crystallized films). Similarly, plasmonic heating at an average temperature of 60 °C resulted in effective dynamic temperature equivalent to heating at 70 °C (85 °C) for solution-crystallized (melt-crystallized) films, well above the melting temperature of the polymer. However, no visible melting of the sample is observed at times up to which the maximum crystallinity is observed (~ 8 minutes). In fact a continuous and rapid increase in crystallinity is observed, evidenced by a steady increase in spherulite size, up to the annealing time for maximum crystallinity. This intentional breaking of the symmetry between melting and annealing (transitioning amorphous material to crystalline) may explain the higher maximum crystallinity possible under photothermal annealing at 60 °C ($T_m - 5^\circ\text{C}$).

As an aside, we point out that the temperature near the particle under photothermal heating is expected to increase at a more rapid rate than the background temperature under these conditions, as discussed in a previous work.²³⁶ Measurement of the effective temperature in the volume of polymer immediately surrounding photothermally-heated gold nanorods in the same molecular weight PEO (with a similar AuNP:PEO ratio) in thin films slightly above the PEO melting point showed effective temperatures of 10 to 30 °C above the background temperature with this temperature difference increasing with laser intensity (and thus background temperature) .

The results of Figure 4.13 indicate that heterogeneous heating via the photothermal effect breaks the symmetry between growth of lamella at the periphery of the spherulite and bulk melting of existing crystalline regions. If nanoparticles are dominantly positioned in amorphous regions, amorphous material will be more influenced by the annealing process. Furthermore, if the existing crystalline regions are the coolest in the sample, this will not only help to preserve existing crystalline structure but also serves as a cold nucleating site, triggering the warm amorphous material to crystallize. This temperature-induced symmetry break between melting and crystal formation is not possible in a uniformly heated sample.

To illustrate the potential utility in annealing with photothermal heating, Figure 4.14 shows the annealing time to achieve the maximum crystallinity (%) at a particular temperature (t_{\max}) as a function of the average annealing temperature. Comparing conventional annealing of solution crystallized films (grey open squares/grey solid line) with the photothermally annealed films (black open diamonds/black solid line), it is evident that photothermal annealing has a lower t_{\max} at every temperature. The same can also be seen in melt-crystallized films, for photothermally and conventionally annealed films (the black closed diamonds/black dotted lines and grey closed squares/grey dotted lines, respectively). Whereas at higher temperatures, as discussed in the previous paragraph, photothermal annealing enables access to processing regimes not accessible by traditional means, at low temperature, the photothermal approach has a significant practical advantage, much shorter annealing times. In fact, the difference in t_{\max} is most pronounced at lower temperatures

where the time required to achieve the maximum crystallinity (i.e. largest spherulites) is 3 to 6 times more rapid than that required for conventional annealing.

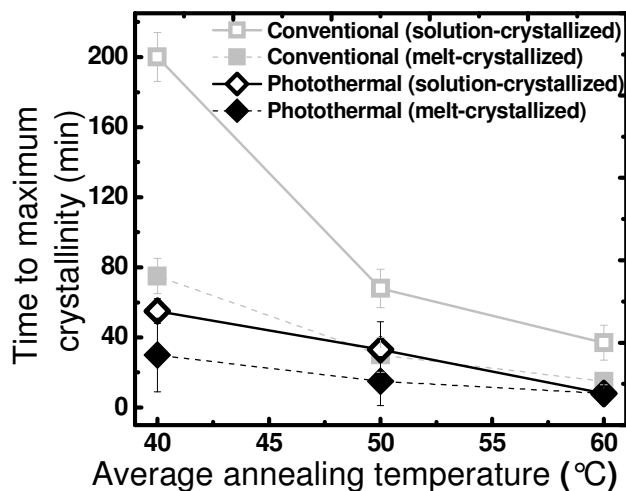


Figure 4. 14:Time to reach the maximum crystallinity (t_{max}) as a function of average annealing temperature as determined by DSC for each annealing time at each temperature.

Thus there are benefits to photothermal heating both far from and close to the melting temperature of the matrix polymer. Well below the melting point, photothermal heating allows annealing at lower average temperatures and for shorter times than that for a traditional annealing approach. At post-processing temperatures close to T_m , photothermal

heating effectively enables higher annealing temperatures than would be possible with traditional annealing. Thereby processing outcomes can be achieved with photothermal heating that are not accessible with traditional means.

4. 4 Conclusion

This work demonstrates the efficacy of photothermal heating as a tool for annealing metal particle polymer nanocomposite systems. At low annealing temperatures (relative to the melt temperature), photothermal annealing can be used to attain maximum crystallinity in shorter annealing times, while at temperatures closer to the melt, it produces effects akin to annealing at much higher temperatures, without globally melting the sample thus generating results not attainable via traditional annealing schemes. This symmetry-breaking ability to perfect and grow existing spherulites while preventing bulk melting is due to the heterogeneous temperature distribution within the sample where the temperature increase is much larger in the regions around the nanoparticles than in the remainder of the sample. The effective dynamic temperature at which the sample responds was calculated via use of the time-temperature superposition principle.

This research extends scientific understanding of the use of metal nanoparticles as localized heat sources within solid (particularly polymeric) materials to manipulate crystallinity, cross-linking, or chemical reactions within a solid object upon exposure to visible light. In this post-processing approach, internal sample structure can be altered at any point during an object life cycle: immediately after traditional fabrication (such as molding) to improve

properties, to repair or reinforce during the active life of the object, or at end-of-use to trigger degradation. Although in this work, the metal nanostructures were introduced specifically for photothermal heating, the same approach could be utilized in any metal particle containing composite where the primary use of the particle was another function (e.g., thermal, electrical, or optical). As demonstrated here, the effects of the innately heterogeneous temperature distribution and avoidance of surface heating (due to heat being generated from inside the sample) enables access to new polymer processing outcomes that are not achievable via traditional thermal treatment.

**CHAPTER 5: ENHANCED MAXIMUM
CRYSTALLINITY AND MECHANICAL MODULUS
OF POLYMER NANOFIBERS WITHOUT LOSS OF
NANOFIBROUS MORPHOLOGY VIA
HETEROGENEOUS PHOTOTHERMAL ANNEALING**

Chapter 5: Enhanced maximum crystallinity and mechanical modulus of polymer nanofibers without loss of nanofibrous morphology via heterogeneous photothermal annealing

5. 1 Introduction

Polymeric nanofibers are technologically-useful low-cost, high surface area materials for applications such as tissue engineering^{273,37, 72}, drug delivery ^{274,219}, filtration^{275,276}, and energy storage^{277, 278,222}. A common technique for generation of polymeric nanofibrous materials is electrospinning.⁸⁰ However, electrospun nanofibrous mats typically show poor structural integrity due to the lack of inter fiber bonding and molecular orientation. Crystallinity retardation due to rapid solidification during the electrospinning process also contributes to poor mechanical performance.^{181, 92, 182} Strategies to improve mat mechanical properties aim to address these issues by (1) aligning nanofibers ^{183, 184}, (2) thermal annealing, or (3) chemical cross-linking.^{279, 280} In particular, post-processing thermal annealing has emerged as an effective method for improving nanofiber web mechanical properties.¹⁸⁸¹⁸⁰¹⁸³¹⁸¹¹⁷⁸

Post-fabrication annealing can be utilized to enhance crystallization, with studies on electrospun nanofibers suggesting that heating to temperatures above the glass transition but below the melting temperature increases crystallite size and results in merging of larger crystallites due to crystallization of tie molecules.¹⁸⁰ The ideal process of crystallinity maximization involves selective thermally-induced crystallization of amorphous regions

coupled with simultaneous retention of any pre-existing highly stable crystalline structure. The lower the heating temperature utilized, the longer the time needed to achieve maximum crystallinity; however when annealing using temperatures closer to the polymer melt temperature, undesirable melting and recrystallization (i.e., loss of existing crystallites) effects become more dominant. Melting and recrystallization in an annealing experiment generally lead to a dramatic decrease in overall sample crystalline fraction. An additional complicating factor when annealing nanostructures is the large surface area to volume, which results in strong surface melting effects, where the innately less stabilized surface melts (or more generally, relaxes) at a lower temperature than the sample interior. Furthermore, in electrospun materials the polymer chains tend to be aligned and elongated along the fiber axis. This unstable quasi-equilibrium can lead to dramatic relaxation (including mat shrinkage) upon heating. These factors suggest that a heterogeneous temperature distribution where, for example, the interior of the fiber is much warmer than the exterior or the amorphous regions hotter than the crystalline volumes, may be a highly beneficial approach to post-process polymeric nanofibers, thus retaining the highly useful nanostructured morphology while simultaneously improving the properties (for instance, increasing the crystalline fraction) of select regions.

In the current study, we explore this approach of creating a heterogeneous temperature distribution within polymer nanofibers by using a low concentration of gold nanospheres (AuNP) as internal, optically-controlled nanoscale heat sources within the fibers. The size scale of the nanoparticles (~20 nm diameter) indicates (from hysteric considerations) that

they will be predominantly located within amorphous regions. Metal nanoparticles exhibit a surface plasmon resonance (SPR) and corresponding thermal energy generation when incident light energy resonant with the SPR is converted into heat ²³². Such photothermal heating has been previously demonstrated in aqueous systems,²³⁷⁻²⁴⁴ as well as solid polymer environments such as films^{281, 3,4, 5, 6}, with few reports within nanofibrous systems.^{282, 283,236, 246} Because the heat is generated at the nanoparticles, these sites are the warmest points in the solid and the temperature decreases as one moves away from such thermal hot spots.^{234,284-286} Photothermal heating in a nanofibrous system (which has a high porosity, >70%) will differ from that in bulk as conduction will be the predominant heat mechanism along the fibers, which have a very small cross-sectional area (diameter ~200 nm), in competition with convection losses through the air surrounding each fiber. This heterogeneous environment is much more complex than the relatively homogeneous region surrounding the heated nanoparticle in a liquid or uniform bulk solid medium where heat loss occurs uniformly in all directions by conduction.

In the current report, we compare the effects of post fabrication annealing (including nanofibrous mat morphology, crystallinity fraction, average crystallite size, and mat mechanical properties) in a metal (gold) nanoparticle: poly (ethylene oxide) (AuNP:PEO) electrospun nanofibrous composite via conventional means with that obtained from photothermal heating at the same average temperature. The studies demonstrate that the maximum crystallinity is achieved more quickly under photothermal heating and higher maximum crystallinity values are obtained. The most important aspect of this work is that

comparing cases with the same increase in crystallinity (achieved at the same temperature), photothermal heating preserves the unique nanostructured morphology of the nanofibrous mat whereas such effects are not possible with the uniform temperature distribution present under conventional annealing treatment. Evaluation of mechanical properties confirms that samples annealed by photothermal heating possess higher moduli than those annealed conventionally, consistent with the observation of higher crystallinity.

In the range of annealing temperatures 5-35 °C below melt temperature, crystallinity trends for conventional annealing followed time temperature superposition, thereby enabling the use of this calibration to estimate the “effective dynamic temperatures” experienced by the sample when subjected to photothermal heating. This causes the sample to act as if it were at a significantly higher temperature, thereby showing faster crystallinity increase. The effective dynamic temperature achieved during photothermal annealing is significantly greater than the average temperature achieved by conventional annealing. This ability has special significance at annealing temperatures closer to melt temperature where photothermal annealing was found to demonstrate effective temperatures significantly higher than the melting point, enabling high temperature dynamics within the sample (a fast increase in crystallinity) without bulk melting (which would occur in conventional annealing where the entire sample would experience this temperature).

5. 2 Experimental

5.2. 1 Metal nanoparticle synthesis

Fren's method was used to synthesize the citrate stabilized spherical gold nanoparticles²⁴⁹ wherein aqueous tetrachloroauric (III) acid was reduced with aqueous trisodium citrate solution (both Sigma Aldrich). Dry polyvinyl pyrrolidone (PVP) (Scientific Polymers Products, Inc.) was added to the solution in an amount equal to that of the tetrachloroauric (III) acid to further stabilize the nanoparticles after synthesis. Characterization of gold nanoparticles in solution was done using transmission electron microscopy (TEM) (Hitachi HF2000 transmission electron microscope) using freshly prepared nanoparticle solution drop cast directly onto copper grids (Ted Pella, PELCO 400 Mesh Grids). Spherical nanoparticles were observed to have an average diameter of 19 ± 3 nm. Extinction spectra of the solution were measured with an ultraviolet-visible spectrometer (CARY 50 Scan) identifying the peak of surface plasmon resonance (SPR) at 527 nm.

5.2. 2 Nanocomposite mat fabrication

Poly(ethylene oxide) (PEO) (Scientific Polymer; molecular weight 400, 000 g/mol) solutions in AuNP solution were prepared and perylene in powder form (Sigma Aldrich # 394475-1G) was added to them to obtain a 6 weight percent (wt %) solution resulting in 1.6 wt % AuNP:PEO and 0.09 wt % perylene:PEO in the final nanofibrous sample after electrospinning. This solution was magnetically stirred for 24 hours at room temperature before electrospinning.

The AuNP:PEO solution was electrospun using a traditional needle electrospinning set up with a 5 cm long, 18 gauge stainless steel needle. A programmable syringe pump (New Era Pump Systems, Model NE 500) extruded the polymer out of a 12 mL syringe and with an applied positive polarity, high voltage to the needle (Glassman High Voltage, Model No. FC60R2). A feed rate of 4 $\mu\text{L}/\text{min}$ with an operating voltage of 11kV and working distance of 12 cm was used. The grounded collector was covered with aluminum foil to collect the randomly-oriented nanofibrous mat. The nanofibrous samples were electrospun for 1 hour to obtain mats with a thickness of $7 \pm 3 \mu\text{m}$ as measured by an alpha step profilometer (VeecoDektak Model 150). The mats were subsequently annealed by conventional or photothermal heating at average temperatures ranging from 40-60 $^{\circ}\text{C}$ for 4-400 minutes.

5.2. 3 Annealing methods and temperature measurement

Three different methods of post-process annealing were used to treat the nanofibrous samples: conventional annealing, photothermal annealing (natural-cooled), and photothermal annealing (fan-cooled)

Conventional annealing of the nanofibrous samples was carried out using a programmable, temperature-controlled heated stage utilizing a copper block 2.5 cm x 7.5cm x 1 cm attached to a commercial hot plate (VWR 7X7 CER Hotplate), details of which have been described previously.²⁸¹ Samples were placed on the pre-heated hot stage; the average temperature attained by the sample during initial heat up, the active annealing time at a given annealing temperature, and the cool down to room temperature were monitored via a fluorescence technique (see below).

For photothermal annealing, samples were mounted on the same stage at room temperature and irradiated with 514 nm light. In this work, light intensities (measured using a power meter (Coherent Model Powermax PM10) ranging from 0.078 W/cm^2 to 0.125 W/cm^2 were utilized, resulting in steady state temperatures of $40 \pm 2.4 \text{ }^\circ\text{C}$ to $60 \pm 1.8 \text{ }^\circ\text{C}$. The average temperature of the system was increased by increasing the laser intensity, as discussed in detail previously.²⁴⁷ Samples that experienced photothermal annealing cooled significantly slower than conventionally annealed samples after the removal of the heating source. This effect was observed to be most pronounced at higher annealing temperatures ($60 \text{ }^\circ\text{C}$) where photothermally annealed samples took almost 20 minutes longer than conventionally annealed samples to cool down to room temperature (i.e. ~ 40 minutes to cool as compared to ~ 23 minutes cool down time in conventionally annealed samples).

In order to isolate the effect of cool down from the effect of annealing temperature and duration alone, a third protocol was implemented wherein photothermally heated samples were actively fan-cooled. Thus, in the fan-cooled experiments, the cooling rate for photothermal annealing was matched to that observed under conventional annealing by the use of an external cooling fan in order that the entire temperature cycle (i.e., heating, annealing, and cooling) was identical for the two types of thermal treatment. A non-contact temperature measurement utilizing perylene as a fluorescent probe monitored the average temperature of the nanocomposite.²⁵⁰ Perylene displays temperature-dependent changes in its emission spectrum; in particular, the ratio of the emission intensity at the "trough" at 465 nm to that of the "peak" at 479 nm changes linearly with temperature, providing an in situ probe

of temperature.²⁴⁷ As previously discussed, perylene molecules are uniformly distributed throughout the entire sample and thus the temperature measured via this technique is an average over all environments. Due to the dilute doping of AuNP, most perylene molecules (and in fact, most of the polymeric sample) are relatively far from a gold nanoparticle. Thus this temperature measurement provides a result which is slightly higher than but very close to the background temperature, which is the coolest temperature in the heterogeneously heated sample.^{236, 248, 287}

5.2. 4 Sample characterization

Scanning electron microscopy (SEM) (JEOL JSM-6400 FE w/EDS, operating at 5 kV) images were used to study fiber morphology and porosity changes as a function of annealing conditions. Electrospun mats were sputter coated with gold/palladium to reduce surface charging. Nanofiber diameters were obtained from an average of at least 100 points for each annealing condition from the SEM images using the NIH ImageJ software. Porosity of the electrospun webs was determined using Image J software, converting the SEM image to an 8 bit image, adjusting the pixel intensity to approximately select only the first layer of nanofibers,^{156, 288, 289} and calculating this area fraction. Porosity measurements from this image analysis method were consistent with direct density measurements (measuring the mass of a nanofibrous mat of known volume), where the literature values of PEO density and the law of mixing were used to estimate void space fraction.

Differential scanning calorimetry (DSC) (Perkin Elmer Diamond DSC-7) was used to determine crystalline fraction. The specimens were subjected to heating scans from 25 to 80 °C at a heating rate of 5 °C/minute (first heating cycle). Pyris software was used to analyze the DSC data. Overall crystallinity (% X_c) was calculated from: $\%X_c = (\Delta H_m / \Delta H_m^*) \times 100$, where ΔH_m and ΔH_m^* are the melting enthalpies for the specimen and 100% crystalline PEO, respectively ($\Delta H_m^* = 213.7$ J/g).²⁵⁵

The Universal testing machine (Instron Model 5544 using the Bluehill version 2.0 software) measured the moduli of the samples as a function of annealing. Mechanical measurements were carried out for the untreated control, nanofibrous samples annealed at 40 °C for 15 and 180 minutes, and at 60 °C for 15 and 30 minutes. These conditions were selected based on crystallinity values obtained from the DSC where the crystallinity of the annealed sample was observed to show the most pronounced change at the given specific annealing temperature. Samples were prepared according to ASTM standard D4762-04 with a gauge length of 1.5 cm, width of 1.0 cm. To account for variation in thickness within a single mat, the thickness of each electrospun specimen was measured before mechanical measurements using a thickness gauge (Mitutoyo absolute Digimatic thickness gauge, Code No.543-394B, and a measuring force of less than 0.7 N). The moduli values obtained were corrected as a function of mat porosity thereby accounting for the fiber fraction contribution.

To study annealing induced crystal structure changes, wide angle x-ray diffraction (WAXD) was performed at 2θ angles ranging between 5 and 30° using a step size of 0.01° on a Rigaku

Smartlab diffractometer with CuK α radiation at a wavelength of 0.1541 nm. From the diffractograms, FWHM (full width at half the maximum intensity) and average crystallite size (calculated using the Scherer equation) was reported for the peak observed at $\sim 2\theta$ angle 19° corresponding to the (120) reflection of PEO.²⁹⁰

5.3 Results and Discussion

5.3.1 Increased crystallinity without compromising nanofibrous morphology

The key result in this study is that photothermal annealing results in higher overall crystallinity without sacrificing the nanofibrous morphology of the nonwoven mat as is shown in Figure 5.1 where samples were annealed at 50°C ($\sim T_m - 15^\circ\text{C}$), where this phenomenon is most pronounced.

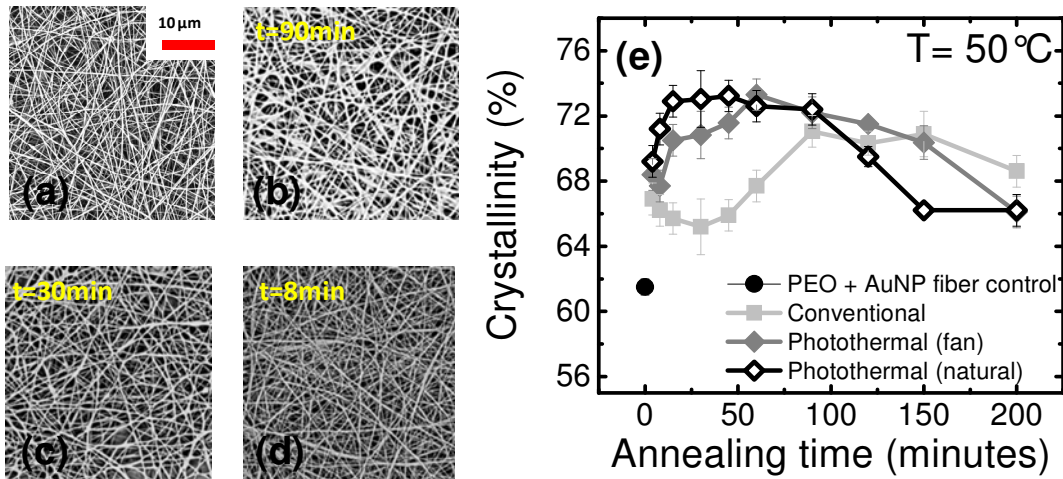


Figure 5. 1. SEM images of (a) untreated AuNR:PEO nanofibers; and at a crystallinity percent of $\sim 70\%$ after annealing at 50°C for (b) 90 minutes conventionally, (c) 30 minutes by photothermal annealing (fan cooled) , (d) 8 minutes by photothermal annealing with natural cooling ; (e) Crystallinity as a function of annealing duration (minutes) at 50°C .

Each curve demonstrates the expected response: at short times the crystallinity increases, whereas at longer time, overt melting occurs, which destroys existing crystallites, results in non-ideal recrystallization, and thus decrease crystalline fraction: between these extremes, a maximum crystallinity is achieved. Here, the maximum crystallinity achieved under conventional annealing is 70% which occurs at ~ 100 min. For the fan-cooled photothermal samples (with identical heating/cooling times) the maximum crystallinity is 73% which occurs at ~ 60 min. As discussed in Section 5.3.4 below, the heterogeneous temperature distribution resulting from photothermal heating means that regions particularly close to the particles are significantly warmer than the average temperature in the sample. Thus, the effective dynamic temperature in the sample is higher under photothermal heating, which reduces the time needed to achieve maximum crystallinity. For the photothermal samples cooled naturally (slower cooling rate), the overall crystallinity was equal to that for the fan cooled samples (73%) but occurred at ~ 20 min of active heating (vs. 60 min). In this case, the sample remains warm after the resonant light is removed, effectively increasing the annealing time as the sample naturally, slowly cools.

Examining the morphology of the samples at 70 % crystallinity, we observe that the mat morphology is essentially completely preserved for the photothermal (natural-cooling) case which was confirmed by image analysis which shows the average fiber diameter (143 ± 32 nm) and porosity (76.4 ± 0.5) are unchanged from that in the original, as-spun sample (average fiber diameter 169 ± 27 nm, porosity (77.2 ± 0.4)). The photothermal sample with fan-cooling, which required a longer active treatment to achieve the same crystallinity, has a

morphology very similar to the original mat, with only a slight thickening of the fibers (204 ± 39 nm) and decreased porosity (72.6 ± 0.5) whereas there is overt damage to the sample annealed (average fiber diameter 350 ± 79 and porosity 61.2 ± 0.6) under conventional conditions. This result highlights the utility of annealing with a heterogeneous heat profile. Under conventional conditions, the lower melting point surface of the sample is the first to warm as heat must penetrate through the fiber surface in order to reach the interior. This results in surface relaxation and melting. In contrast, in the photothermal approach the fiber surface is the coolest region of the sample: heat is generated within the nanofiber and the heat loss mechanism of convection and conduction by the air is the most dominant at the fiber surface. Thus the fiber surface is less affected in the photothermal approach, leaving the nanostructured morphology intact.

Similar behavior was seen for all samples at 60°C , however the time scale is compressed (as expected from time-temperature superposition) and the overall crystallinities are slightly higher for the photothermally annealed samples (as shown in Figure 5.2). At 60°C , for the photothermal samples, there appears to be a two stage increase in crystallinity. The first stage, which is identical to the annealing behavior for the conventional samples, happens rapidly with a sharp increase in crystallinity from 62 to $\sim 70\%$ over ~ 10 min annealing period. Then the photothermal samples continue to increase in crystallinity (to a maximum of 77 and 76%) over the next 20 to 50 min for natural and fan cooled samples, respectively. No further increase in crystallinity is observed for the conventional samples.

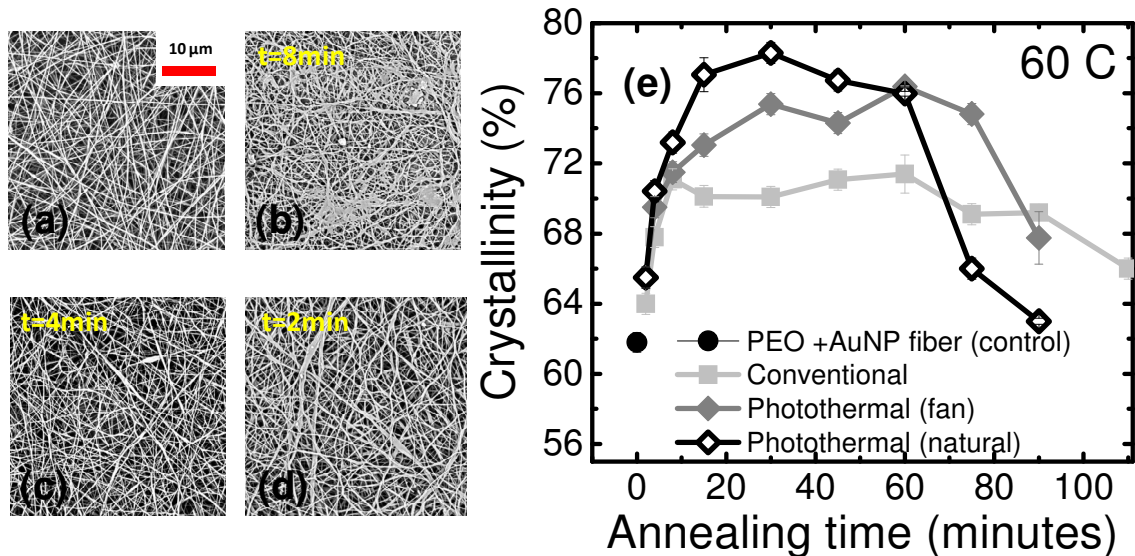


Figure 5.2 SEM images of (a) untreated AuNR:PEO nanofibers; and at a crystallinity percent of ~70% after annealing at 60 °C for (b) 8 minutes conventionally, (c) 4 minutes by photothermal annealing (fan cooled) , (d) 2 minutes by photothermal annealing with natural cooling ; (e) Crystallinity as a function of annealing duration (minutes) at 60 °C.

As is expected, at lower annealing temperatures (40 °C), the time to reach maximum crystallinity increases dramatically (~600 min for conventional and ~300 min for photothermal) and the overall maximum achievable crystallinity is lower for the photothermal samples (as shown in Figure 5.3). It is of note that the maximum crystallinity for the conventional samples is ~70% for all annealing temperatures studied. At each of these temperatures, the naturally cooled photothermal samples achieve higher crystallinities at shorter annealing times, which is logical due to the slower cooling rate for the photothermal samples. It is germane to note that in choosing an annealing process, the

naturally cooled photothermal samples yield the largest increase in crystallinity over the shortest annealing time, and therefore would be the optimal route to obtain highest crystallinity while maintaining the nanofibrous morphology. In this study, the fan cooled samples were employed primarily to validate the efficacy of the photothermal approach under identical heating/cooling conditions.

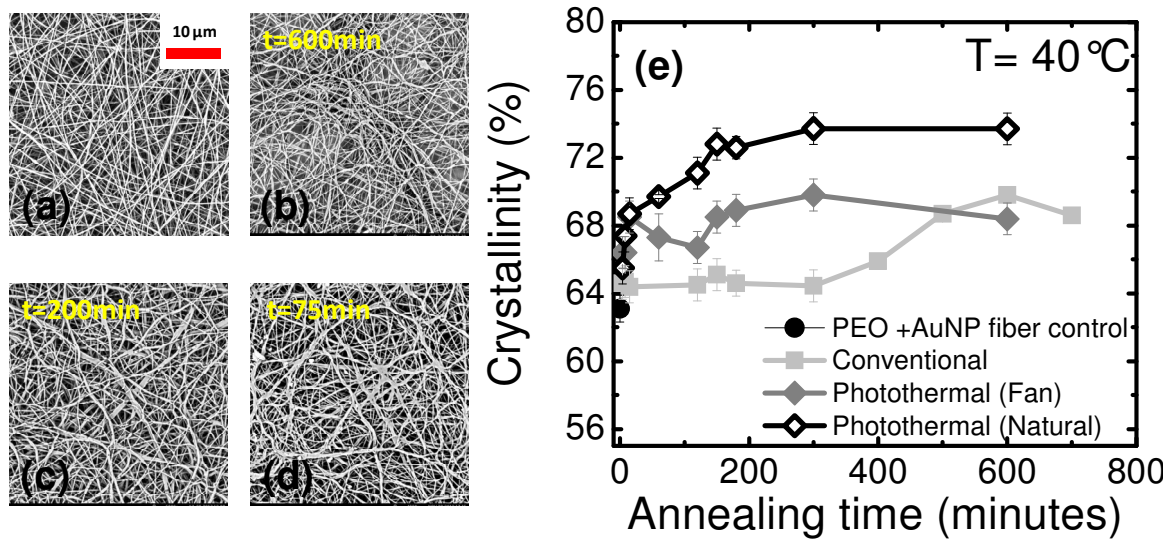


Figure 5.3 SEM images of (a) untreated AuNR:PEO nanofibers; and at a crystallinity percent of ~70% after annealing at 60 °C for (b) 600 minutes conventionally, (c) 200 minutes by photothermal annealing (fan cooled) , (d) 75 minutes by photothermal annealing with natural cooling ; (e) Crystallinity as a function of annealing duration (minutes) at 40 °C.

At the three temperatures studied, recrystallization is evident in the higher temperature (50 and 60 C) as shown by the decrease in crystallinity at longer annealing times. This, however, is not present for the samples annealed at 40 C for the annealing times studied (up to 600 min).

5.3. 2. Crystal structure and morphology

Wide angle x-ray diffraction revealed two crystalline peaks ($2\theta \sim 19.0^\circ$ (120 reflection) and 23.1° (112)). An example of the intensity as a function of 2θ is presented in the supporting information. The 120 reflection is strong and the 112 reflections are very weak, which is believed to be due to the orientation of the crystals (row nucleated structures) in the nanofibers (as shown in Fig. 5.4).

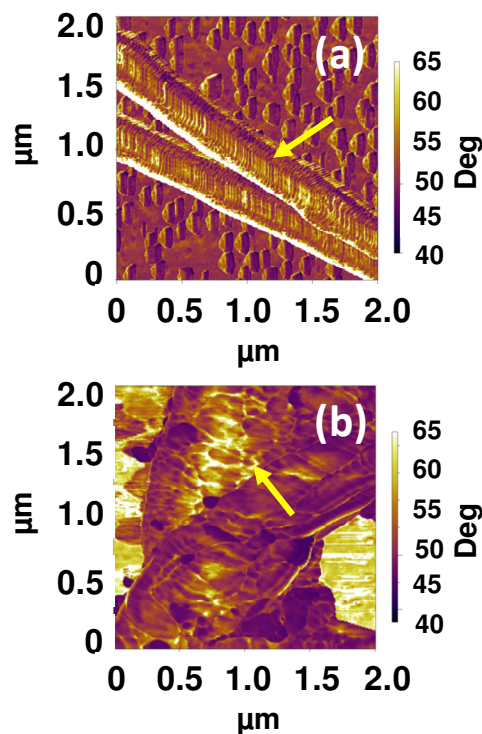


Figure 5. 4 AFM images of (a)untreated AuNP:PEO nanofibers, with arrow indicating row nucleated structure; (b) AuNP:PEO nanofibers annealed by photothermal annealing at 60 °C for 60 minutes with arrow indicating the annealing induced merging of adjacent lamellae.

As is to be expected, the integral peak area increased with annealing temperature and time, indicative of increased crystallinity. Quantification of the crystallinity was not possible, however, due to a convoluted amorphous halo. This was not seen in previous studies on film samples and may be due to the roughness of the mat samples. Crystallite thickness was calculated using the Scherer equation ^{290]} and the results for select samples are shown in Table 5.1. For both annealing conditions studied (40 °C for 180 min and 60 °C for 30 min) the crystallite thickness (120 reflection measured from $2\theta \sim 19.0^\circ$) increased as a function of

annealing method (smallest for conventional and largest for natural cool photothermal). This is consistent with increases in crystallinity as shown by the DSC studies discussed above.

Table 5. 1 Average crystal size and FWHM from WAXD Patterns of As-Spun and annealed AuNP:PEO nanofibers at 40 and 60°C for 180 and 30 minutes respectively

Annealing temperature (°C)	Annealing technique	At 20~19.01°	
		Average crystal size (A)	FWHM (°)
Control	n/a	298	0.28
40 °C, 180 minutes	Conventional	305	0.27
	Photothermal(fan cooled)	346	0.24
	Photothermal(natural cooled)	391	0.21
60 °C, 30 minutes	Conventional	325	0.25
	Photothermal(fan cooled)	356	0.23
	Photothermal(natural cooled)	401	0.21

5.3. 3 Mechanical properties

The ultimate goal in this work is to demonstrate that photothermal annealing will improve the mechanical properties of these fragile nonwoven mats while maintaining the nanofibrous morphology. In general, as shown in Figure 5.5, the modulus of the mats increases as a

function of overall crystallinity. Specifically, at both temperatures (40 and 60 C) and the respective annealing times (15 and 180 min; 15 and 30 min) studied the increase in modulus is most pronounced for the photothermally annealed samples that were allowed to cool naturally. The conventional samples show the smallest increase in modulus. At 15 minutes, there is no change in modulus for the samples annealed at 40 C, whereas, there is a small, yet statistically significant increase in modulus for samples annealed at 60 C. At 60 C, the maximum annealing time before samples begin to lose fibrous morphology is 30 min (see Fig. B). Here, the modulus is about 2 times that of the unannealed control sample. Interestingly, the samples annealed for 180 min at 40 C show the largest increase in modulus, where the modulus for the naturally cooled photothermal sample is ~3 times that for the control. We postulate that this is due to continued crystallization without melting/recrystallization, which occurs at the higher temperatures. Hence, optimal annealing (that is, the largest increase in modulus without compromising the nanofibrous structure) occurs for samples annealed at the lower temperature for longer times.

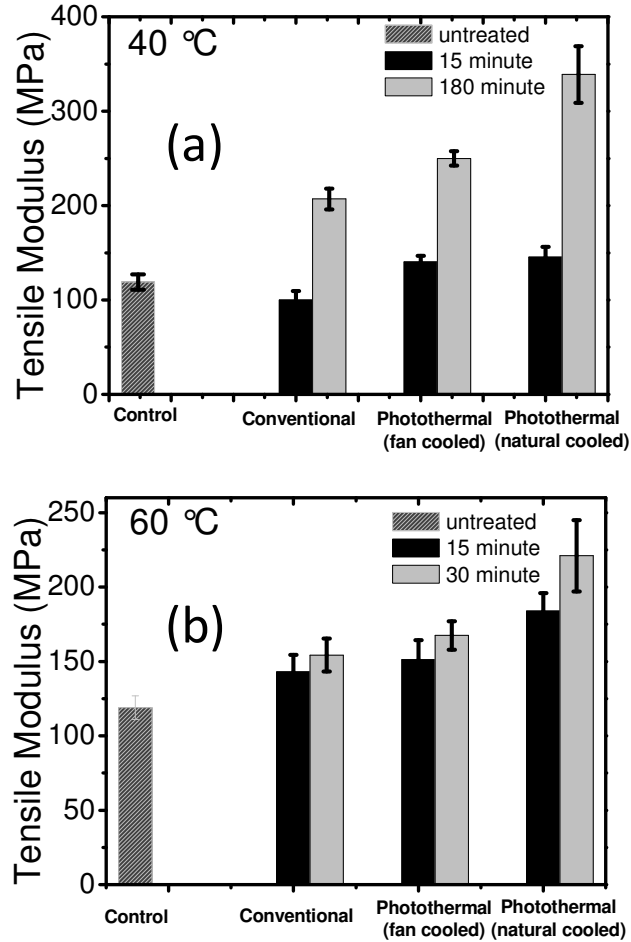


Figure 5. 5 Tensile modulus of AuNP:PEO nanofibers annealed by conventional heating, photothermal heating (fan cooled) and photothermal heating (natural cooled) at (a) 40 °C and (b)60 °C.

5.3. 4 Time-temperature superposition

Since the perylene probe measures an average (or background) temperature, time-temperature superposition was used to estimate an effective dynamic temperature (as discussed previously).²⁸¹To determine the shift factors (utilizing conventional heating where

the temperature is known throughout the sample) the lowest available temperature was utilized as the reference value (40 °C) since it is closest experimental temperature to the PEO glass transition temperature. The shift factor a_T , defined as the ratio of the experimental time to achieve maximum crystallinity to the same quantity at the reference temperature is defined in Eq. (5.1) as:

$$\ln(a_T) = A + \frac{E_a}{kT} \quad (5.1)$$

where the underlying dynamics in the system are assumed to fit a simple Arrhenius equation. In Eq. (5.1), E_a is the effective activation energy (average barrier height), k is the Boltzmann constant, T is the temperature and $A = -E_a/kT_{ref}$ is a dimensionless constant where T_{ref} is the reference temperature.²⁷²

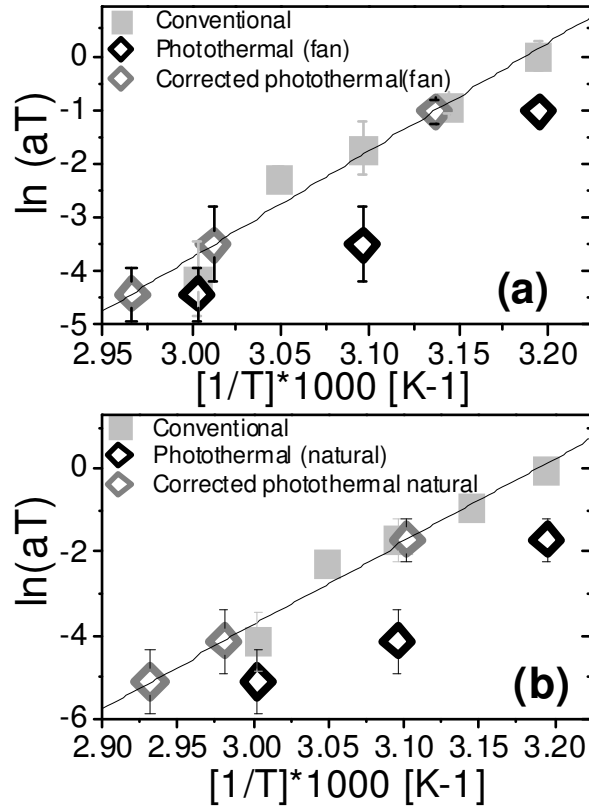


Figure 5. 6 Logarithm of shift factor as a function of reciprocal temperature for nanofibers treated with conventional or (a) photothermal annealing with fan cooling and (b) photothermal annealing with natural cooling . The solid lines show a linear regression through the conventional annealing data.

Plots of $\ln(aT)$ versus $1/T$ for conventional heating are shown in Figure 5.6. Over this temperature range, the Arrhenius fit is sufficient and produces a linear relationship between $\ln(aT)$ and $1/T$ (where $E_a = 40$ kcal/mol and $A = -63.72$). Observed shift factors for photothermal heating (both fan and natural cooling) are also shown (in (a) and (b) respectively) initially plotted at the background temperature. In fact, as discussed elsewhere²⁸¹, the background temperature is not the effective temperature for photothermal annealing, as evidenced by the lower than expected time to maximum crystallinity, and thus a priori, this initial placement is incorrect. While the annealing process is the same for conventional samples and fan cooled photothermal samples (as argued above) (and thus a_T should be the same at a given temperature), the effective temperature at which the photothermal process occurs is higher than the average temperature experienced by both samples. This is further exasperated for the natural cooled photothermal samples due to the longer cooling time. Thus, by examining Figure 5.6, the actual effective temperature (the temperature at which the system is responding) can be determined by shifting the photothermal data onto the calibration curve determined by the conventional data; that is the photothermal data (open black diamonds) are translated horizontally until they fall on the linear regression curve (open gray diamonds). This calibration enables quantification of an effective dynamic temperature which is discussed below and depicted in Figure 5.7

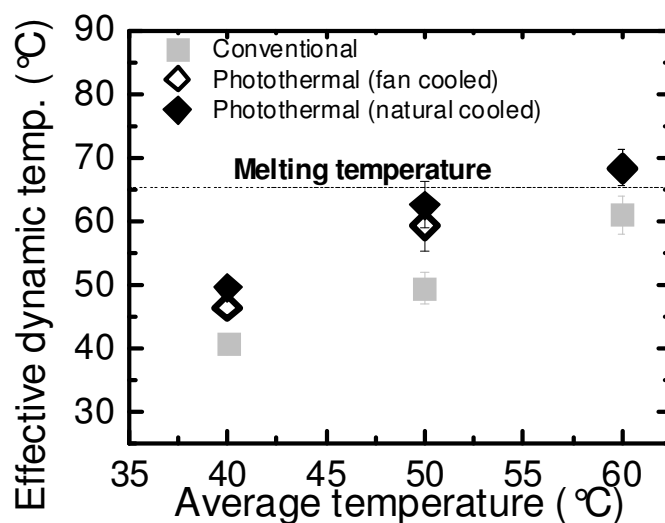


Figure 5. 7 Effective dynamic temperature for AuNP: PEO nanofibers annealed at average temperature.

Figure 5.7 shows the effective dynamic temperature obtained from time-temperature superposition analysis. Average temperature in conventionally annealed samples is indicative of the temperature experienced by the entire the bulk of the sample (shown in grey squares), whereas for photothermal annealing, it is indicative of the average temperature in the vicinity of the nanoparticle measured from the fluorescence of perylene. While photothermally annealed samples (both fan cooled and naturally cooled) showed similar barrier values (~35kcal/mol), a higher barrier was observed in conventionally annealed samples (~40 kcal/mol). The background (or average) temperature experienced by the samples when annealed photothermally is not the same as the effective temperature, due to the heterogenous temperature distribution in the vicinity of the gold nanoparticles, which is responsible for the

rapid increase in maximum crystallinity in these systems as compared to conventionally annealed ones. At every given temperature, the effective temperature in photothermally annealed systems is at least 7-10 °C higher than the bulk overall temperature in conventionally annealed samples. This higher effective temperature is of special significance at higher annealing temperatures especially near the melt temperature. For example, while the global temperature experienced by the samples in photothermal annealing is 50 °C, the trends for crystallinity reflect the presence of a much higher effective temperature (almost 65 °C) while still maintaining the nanofibrous morphology without showing any visible signs of melting. This effect is more pronounced at 60 °C wherein conventional annealing reaches ~70 % crystallinity in ~ 8 minutes of annealing but loses its nanofibrous morphology whereas photothermally annealed samples achieve similar crystallinity values in half the time without the loss of fibrous morphology as shown in Figure 5.2. This is made possible only due to the presence of thermal hot spots in the vicinity of the gold nanoparticles which causes a higher effective temperature to be achieved. Clearly photothermal annealing enables the difference between annealing and overt melting to be more distinguished and enables maximization of annealing effects before recrystallization, and at the same time preserving the fibrous morphology of the mat.

5.3. 5 Annealing in nanocomposite films vs. nanofibers

Having demonstrated the efficacy of photothermal annealing in fibrous media, it is pertinent to compare conventional and photothermal modalities in different geometries (ie fibers vis-à-

vis films) based on previous studies done by authors.²⁸¹ Figure 5.8 presents the effect of annealing duration on total crystallinity in nanofibers (shown in solid filled squares) as compared to that in films (denoted by open squares) via conventional annealing and photothermal annealing at 60 °C.

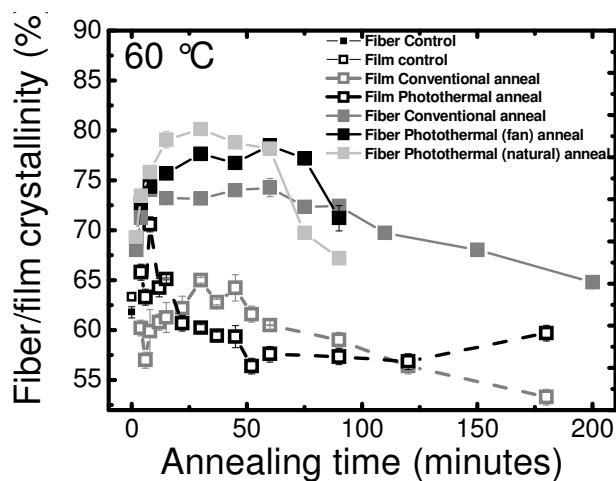


Figure 5. 8 Crystallinity as a function of annealing time in nanofibers (indicated by solid lines) as compared to solution crystallized spun cast films (shown by dotted lines) when annealed by conventional and photothermal heating

The fibrous samples achieve greater overall crystallinity than the film samples. We postulate that this is due to the different crystal morphology in the fibrous structures (row nucleated crystals) vs. the spherulitic morphology observed in films, where the row nucleated structure promotes further crystallization during annealing^{180, 291}. This can be explained by the fact that thermal annealing in nanofibers causes merging of crystallites on a nano scale, causing the

crystallites to transition from a fibrillar structure to a nanogranular structure by the merging and growth of smaller crystallites.¹⁸⁰ The difference in the activation energy barriers to crystallization, quantified by using an Arrhenius equation (Eq. 5.1 above) to fit the time temperature superposition data, is shown in Table 5.2 below. It is important to note that the overall crystallinity used to TTS for the fibers was 70%, which is greater than that used in the films (~64%), Therefore, the energy barriers to crystallization are greater in fiber samples as compared to films. In both the systems (nanofibers and films), it is noteworthy to point out that photothermal annealing results in increased crystallinity over shorter annealing times when compared to conventional annealing.

Table 5. 2Effective activation energy (average barrier height) in fibers and films annealed under conventional and photothermal heating conditions

Annealing condition	E_a (kcal/mol)		
	Nanofibers	Films	
		Solution cast	Melt cast
Conventional	40	19	14
Photothermal(fan cooled)	35	19	15
Photothermal(natural cooled)	35	n/a	n/a

**CHAPTER 6: ANNEALING OF POLYMER
NANOCOMPOSITE FILMS AND FIBERS BY
PHOTOTHERMAL HEATING OF GOLD NANORODS**

Chapter 6: Annealing of polymer nanocomposite films and fibers by photothermal heating of gold nanorods

Having studied the photothermal effect of gold nanospheres in film and fiber media, we explored utilizing the photothermal effect for different particle geometries (such as gold nanorods). Gold nanorods show a widely tunable longitudinal surface plasmon resonance (LSPR) apart from the transverse surface plasmon resonance (TSPR). The polarization specificity of gold nanorods allows light to be absorbed by LSPR only if the linear polarization direction overlaps the longer axis of the nanorod. When incorporated into electrospun nanofibers, the nanorods align along the fiber axis as against aqueous solutions wherein they are randomly oriented. This direction and polarization specific photothermal effect by using nanorods offers tremendous scope to manipulate the crystallinity within nanocomposite systems by altering crystallinity and morphology by obtaining a heterogeneous temperature distribution by changing the aspect ratio of the nanorods.

In this section, the photothermal effect of gold nanorods has been studied in nanofibers and films and compared with conventional annealing. The gold nanorods used in this study were fabricated using a seed-mediated growth method²⁹², resulting in hexadecyltrimethylammonium bromide (CTAB)- capped gold nanorods. Gold nanorods with an aspect ratio of ~4 were used for studying the photothermal effect in fibers whereas for films, gold nanorods with an aspect ratio of ~3 were utilized. The peak extinction in solution due to the LSPR was at ~ 800 nm and that of the TSPR at ~ 520 nm, as shown in Figure 6.1.

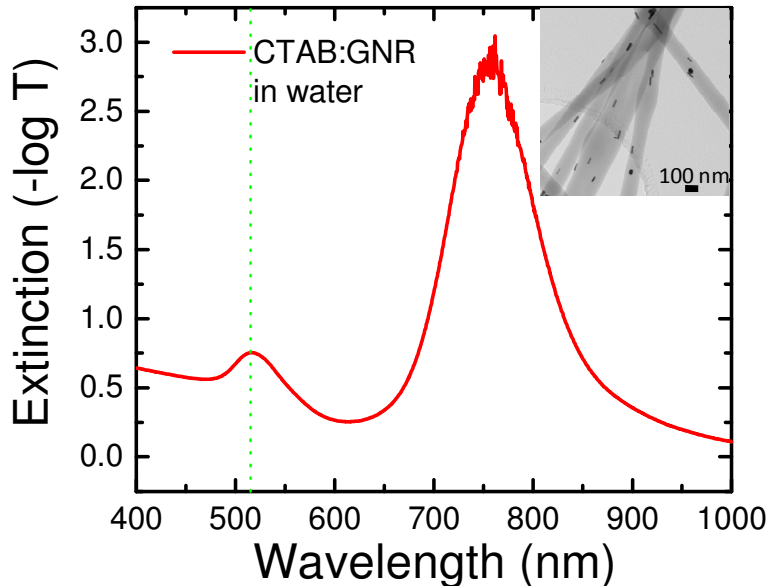


Figure 6. 1. Extinction spectra of CTAB capped gold nanorods in water; Inset showing the gold nanorods in electrospun nanofibers.

6. 1: AuNR:PEO nanocomposite films:

AuNR:PEO nanocomposite films were spun cast using AuNR particles with an aspect ratio of ~3.0 using the method described in the previous section. The mixture was magnetically stirred for 10 hours at room temperature and then spuncast (Laurell Technologies WS-650SZ-6NPP/lite) at 1000 revolutions per minute for 30 seconds on 2.5 cm × 2.5 cm glass slides (Fisherbrand, microscope cover glass 12-540B). Film thickness was measured by an alpha step profilometer (VeecoDektak Model 150) to be $11 \pm 2 \mu\text{m}$. Subsequently, the films were annealed by conventional and photothermal annealing at 40,50 and 60 °C.

Figure 6.2 shows the effect of different annealing types (conventional and photothermal) on the crystallinity of AuNR:PEO nanocomposite when annealed at 60 °C. In both conventional as well as photothermal annealing, the overall crystallinity was found to increase initially and then decrease at longer durations of annealing. Thermal annealing increases the crystallite size by partial melting and recrystallization process. This results in an increase in crystallinity when held at the annealing temperature, followed by a further marked increase during cooling at room temperature.^{293, 294} This trend is further supported in the polarizing microscopy images shown in Figure 6.3, wherein the size of spherulites is found to increase as compared to the control until an annealing time of 15 minutes. While the trends for thermal annealing induced crystallinity increase are similar in both conventional and photothermal cases, the fall in crystallinity in photothermal annealed samples is more rapid as compared to the conventional annealed samples. Correspondingly, in both systems, a decrease in spherulite size is observed at 30 minutes of annealing in Figure 6.3 (f) and (k) for conventionally and photothermally annealed systems. The rapid decrease in crystallinity in photothermally annealed systems as compared to conventionally annealed systems is suggestive of the presence of temperatures much higher than the melting temperatures in the vicinity of the plasmonically activated nanorods, which causes the spherulites in the vicinity of the rods to melt and recrystallize into smaller crystals, thereby causing a crystallinity drop which is more rapid than a conventional annealed system, which experiences a uniform global temperature, which experience a relatively slower recrystallization process.

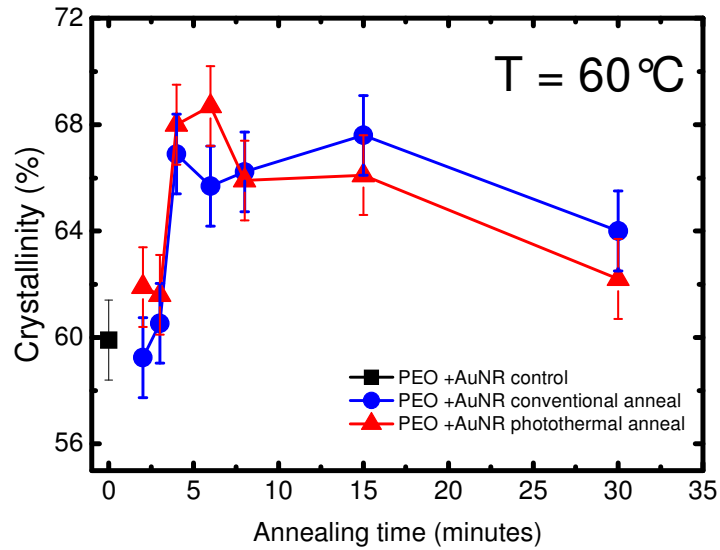


Figure 6. 2 Crystallinity as a function of annealing duration for AuNR:PEO nanocomposite films post-processed via conventional and photothermal heating at 60 °C.

At an annealing temperature of 50 °C as shown in Figure 6.4 , samples subjected to conventional and photothermal annealing show similar trends for crystallinity, with the crystallinity values increasing initially upto 45 minutes of annealing followed by a rapid drop at longer annealing durations. It is important to note that the crystallinity values attained by photothermally annealed samples, for every annealing duration until 45 minutes, is higher than those attained by conventional annealing. The polarizing microscopy images for the annealed samples as shown in Figure 6.5 also show an increase in the size of the spherulites, suggesting thermal annealing induced perfection and growth of crystals followed by a reduced spherulite size due to heterogenous melting and recrystallization.

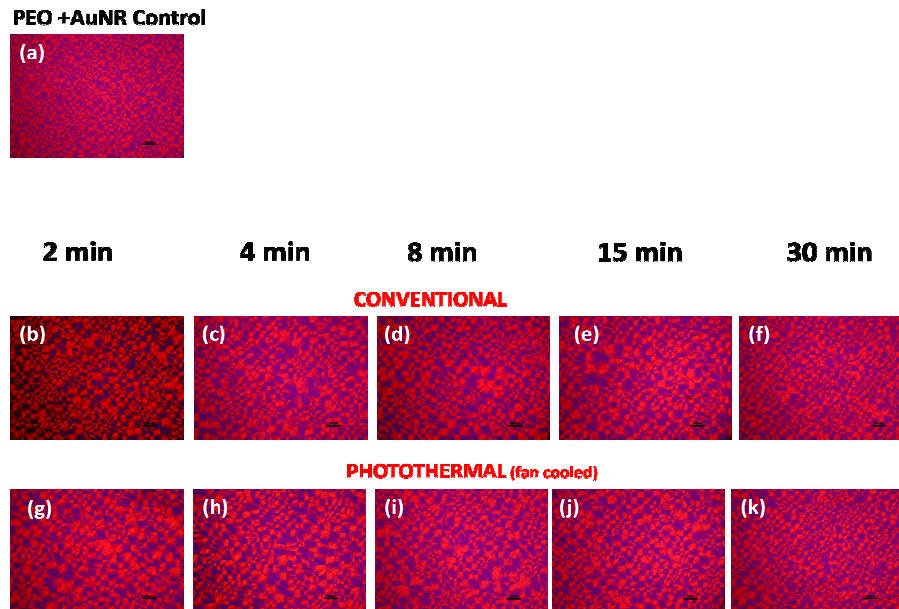


Figure 6. 3. Cross-polarized optical images of (a) solution crystallized AuNR:PEO film after conventional annealing at 60 °C for 2, 4, 8, 15 and 30 minutes conventionally (b), (c), (d), (e), (f) and photothermally (g), (h), (i), (j), (k) respectively.

The annealing behavior in the nanorods film samples is markedly different from that in the nanospheres film samples. Specifically, in the nanosphere samples, the photothermal annealing process resulted in faster annealing (shorter times to maximum crystallinity) at all temperatures studied, whereas in the nanorod samples, there is no real difference crystallinity development between the photothermal and conventional processes. This could indicate that the barrier to crystallization is lower for the nanorod samples.

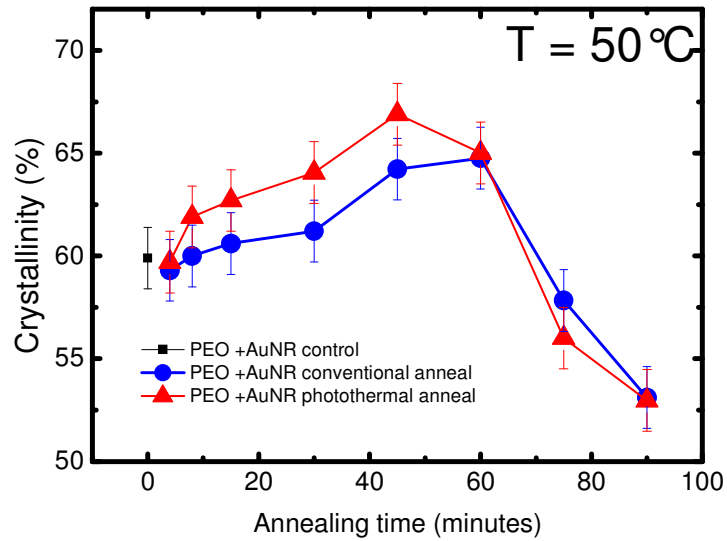


Figure 6. 4. Crystallinity as a function of annealing duration for AuNR:PEO nanocomposite films post-processed via conventional and photothermal heating at 50 °C.

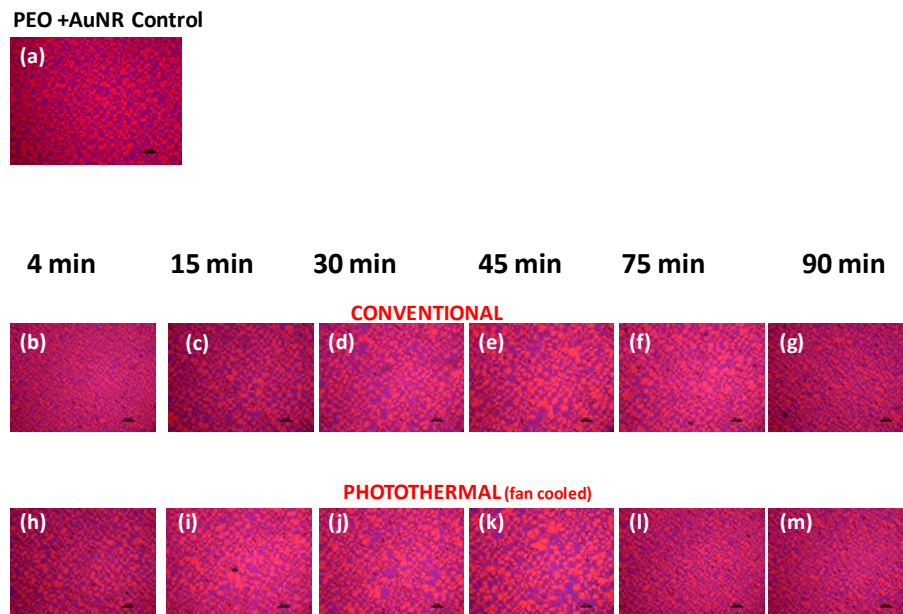


Figure 6. 5. Cross-polarized optical images of (a) solution crystallized AuNR:PEO film after conventional annealing at 50 °C for 4, 15, 30, 45, 75 and 60 minutes conventionally (b), (c), (d), (e), (f) and photothermally (g), (h), (i), (j), (k) respectively.

The difference between conventional and photothermal annealing is clearly most evident at lowest temperature studied, 40 °C, as shown in Figure 6.6. At every annealing duration at 40 °C photothermal annealing outperforms conventional annealing in obtaining higher crystallinity values. While it takes almost 240 minutes to obtain the highest crystallinity (~70 %) in conventionally annealed samples, photothermally annealed samples reach peak crystallinity value (~72%) in 120 minutes of annealing . This peak crystallinity attained at 120 minutes of photothermal annealing at 40 °C (~72 %) has not been obtained in either 60 or 50 °C, wherein the maximum crystallinity obtained is ~68%in both conventional and photothermal modalities. This is further exemplified in the polarized microscopy images shown in Figure 6.7, wherein the spherulite sizes obtained by photothermal annealing beyond 170 minutes is significantly larger than those obtained by any other annealing condition (including annealing at higher temperatures or longer times by both methods). Based on this behavior at 40 °C, the facile annealing realized in the nanorod systems at 50 and 60 °C, is no longer present (presumably due to less thermal energy available in the system). At the lower temperature, the advantage of the photothermal annealing process is evident. Based on earlier studies on nanoparticles in polymeric films systems ²⁸¹; it has been shown that the effective dynamic temperature in photothermally annealed systems enables a faster thermodynamic response to occur within the polymeric system (Chapters 4 and 5), thereby facilitating a more rapid crystallinity increase as compared to a conventionally annealed system. The presence of a higher effective dynamic annealing temperature (due to heterogeneous annealing) during photothermal annealing by nanorods is evidenced by the higher crystallinity values and large spherulite sizes which are clearly absent in a

conventionally annealed system annealed at 40 °C, which shows absolutely no change in morphology at shorter annealing times due to the bulk temperature being too low for thermodynamic changes be experienced by the sample. However, at longer annealing times beyond 200 minutes, the conventionally annealed samples do show an increase in spherulite size, though they are still significantly smaller than the samples annealed photothermally under similar conditions.

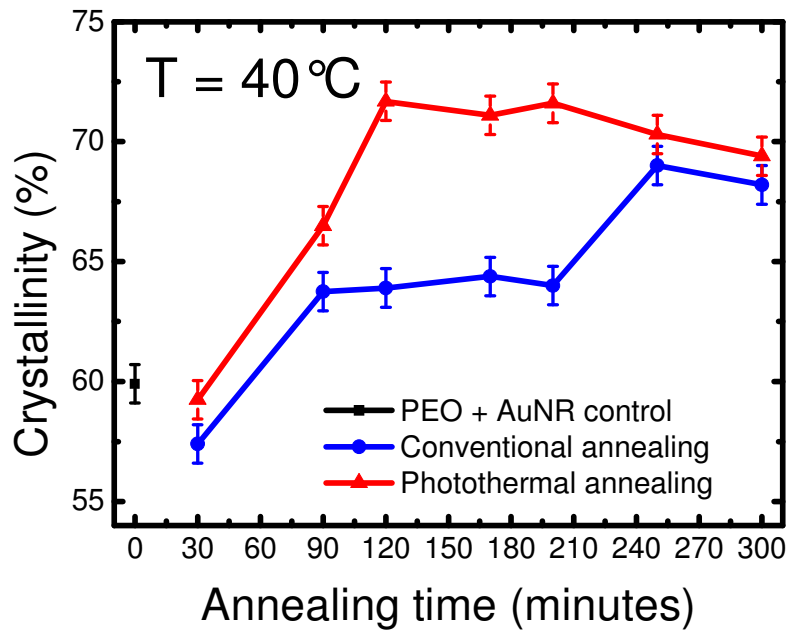


Figure 6. 6. Crystallinity as a function of annealing duration for AuNR:PEO nanocomposite films post-processed via conventional and photothermal heating at 40 °C.

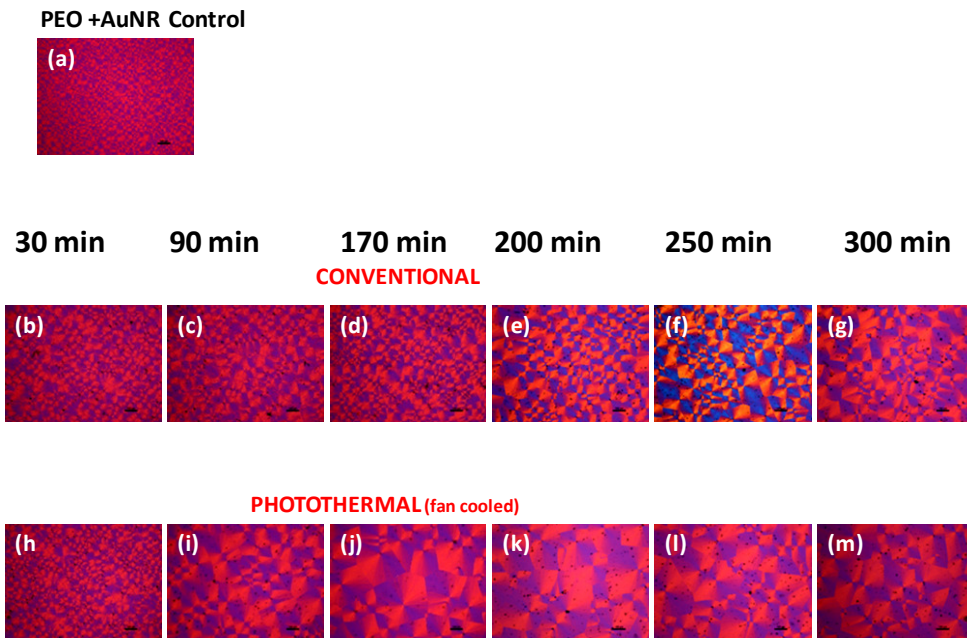


Figure 6. 7. Cross-polarized optical images of (a) solution crystallized AuNR:PEO film after conventional annealing at 40 °C for 30, 90, 170, 200, 250 and 300 minutes conventionally (b), (c), (d), (e), (f), (g) and photothermally (h), (i), (j), (k), (l) and (m) respectively.

In photothermal annealing, the annealing temperature is measured by non contact temperature measurement using perylene which measures the overall average temperature attained by the sample. Calculations comparing previously used nanospheres systems suggest that for a similar 1.6 wt. % of gold nanoparticle solution, there are approximately thrice as many nanospheres present for the same weight percent as there are nanorods. This clearly suggests that with the same average temperature system being achieved in both nanospheres and nanorods containing systems, and there being lesser heat sources in a nanorod containing system, it can be automatically inferred that the heat produced by a nanorods is much higher

than that produced by a nanoparticle. This explains the accelerated effects in obtaining higher crystallinities at 40 °C (~25 °C below the melt temperature) in photothermal annealing experienced by the sample where relatively high dynamic temperature produces effects akin to annealing at higher temperatures. On the same lines, it can be hypothesized that annealing at higher temperatures with photothermal heating results in temperatures possibly higher than the melt temperature itself, thereby resulting in heterogenous melting and recrystallization, evidenced by crystallinity drops and smaller spherulite sizes. Usage of nanorods as annealing sources at higher temperatures (50, 60 °C) causes temperature dynamics to directly go into melting and crystallization, instead of passing through the much crucial annealing phase. From the above study, it can be inferred that the photothermal effect of nanorods can be best utilized at temperatures much below melt temperatures (~25 °C lower), than at higher temperatures, where the excessive heating produced by the nanorods results in melting and recrystallization effects rather than aiding crystal growth and perfection..

6. 2AuNR: PEO nanofibrous composites:

Poly(ethylene oxide) (PEO) (Sigma Aldrich; molecular weight 600, 000 g/mol) solutions in de-ionized water were mixed with the aqueous AuNR solution (with AuNRs having aspect ratio of ~4.0) and perylene powder to form a 6 wt% PEO solution, which ultimately resulted in a 1.6wt% (0.07% volume fraction) of AuNRs and 0.09 wt% (0.02% volume fraction) of perylene (Sigma Aldrich) in the solid nanofibrous sample after electrospinning. The final solution was magnetically stirred for 8–10 hours at room temperature before electrospinning.

Nanofibrous AuNR:PEO composites were electrospun using 1.6 wt% of AuNR using a traditional needle electrospinning set up. The AuNP:PEO solution was electrospun using a traditional needle electrospinning set up with an 18 gauge needle which was 5 cm long. A programmable syringe pump (New Era Pump Systems, Model NE 500) was used to extrude the polymer out of the syringe (with a volume of 12mL) and a high voltage power supply with a positive polarity was supplied by a Glassman High Voltage, Model No. FC60R2. Feed rate of 3 μ L/minute was used with an operating positive voltage of 11kV and a working distance of 12 cm was used. The grounded collector was covered with Aluminum foil to collect the randomly oriented nanofiber mat. The nanofibrous samples were electrospun for 1 hour to obtain mats with a thickness of $7 \pm 3 \mu\text{m}$ which was measured by an alpha step profilometer (VeecoDektak Model 150). These fibrous mats were then annealed at 60 °C by conventional and photothermal heating for 4-100 minutes.

AuNR:PEO nanofibers were able to be electrospun under the above mentioned conditioned, marked by the presence of distinct bead free nanofibers as shown in Figure 6.8 (a). The TEM of the nanorods in electrospun nanofibers shown in Figure 6.1 (inset) verifies that the nanorods were uniformly distributed within the fibers without any agglomeration. Conventional annealing at 60 °C was found to produce fused fibers at 30 minutes of annealing with distinct fiber- fiber bonding. At 60 minutes of conventional annealing, melt like morphology, with extensive fiber bonding and fusing apparent as shown in Figure 6.8(f).

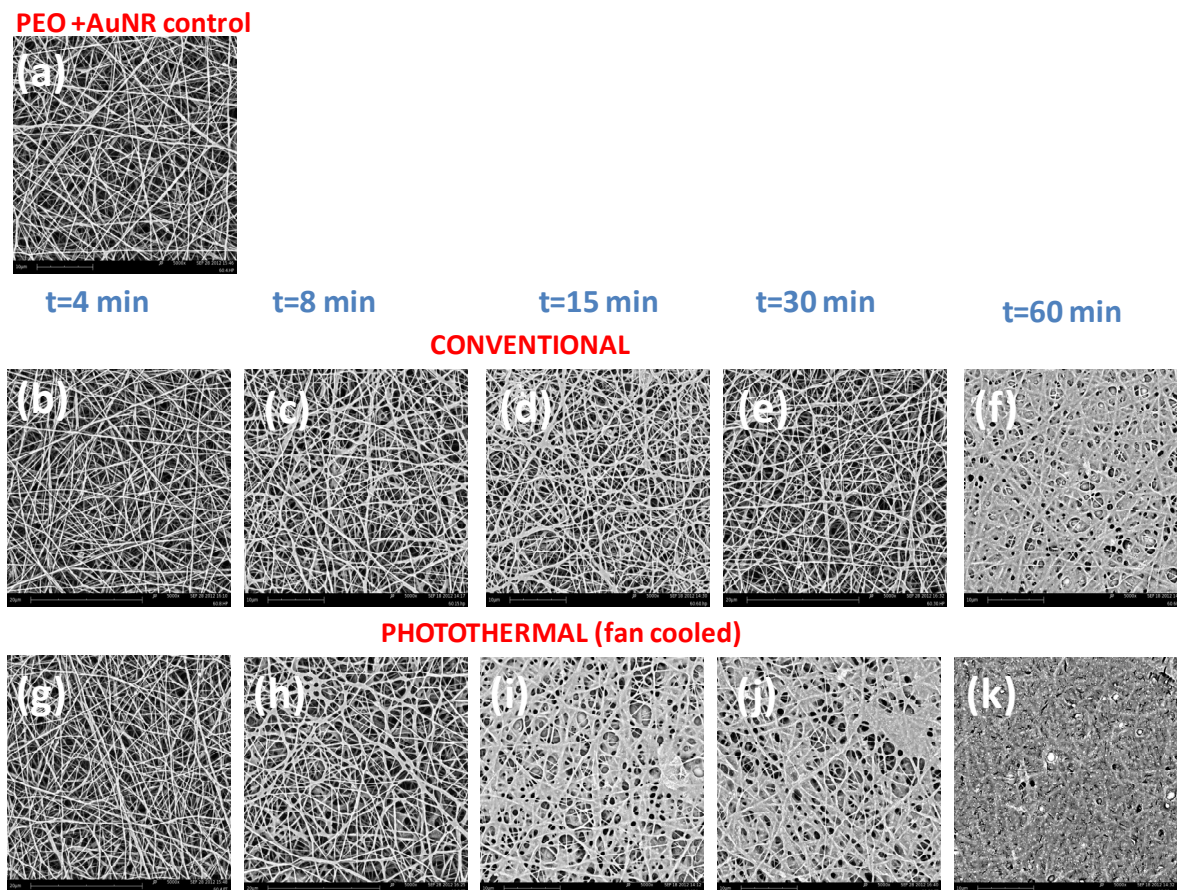


Figure 6. 8. SEM images of (a) AuNR:PEO nanofibers; and after annealing at 60 °C for 4, 8, 15,30 and 60 minutes conventionally (b), (c), (d), (e), (f) and photothermally with fan cooling (g), (h), (i), (j) and (k).

The effect of annealing on the morphology of nanofibers is more pronounced in photothermally annealed samples, with distinct onset of fiber-fiber bonding observed within 8 minutes of photothermal annealing (Figure 6.8(h)). At 30 minutes of annealing, wide spread molten zones with extensive fusion of fibers was observed as observed in Figure 6.8 (j),

finally resulting in a completely molten fibrous mat after 60 minutes of photothermal annealing.(Figure 6.8(k)). Clearly, the photothermal heating generates more heat over shorter times for these nanofibrous systems, with film-like morphologies (as a result of fiber melting and fusion) obtained faster than in conventionally annealed systems.

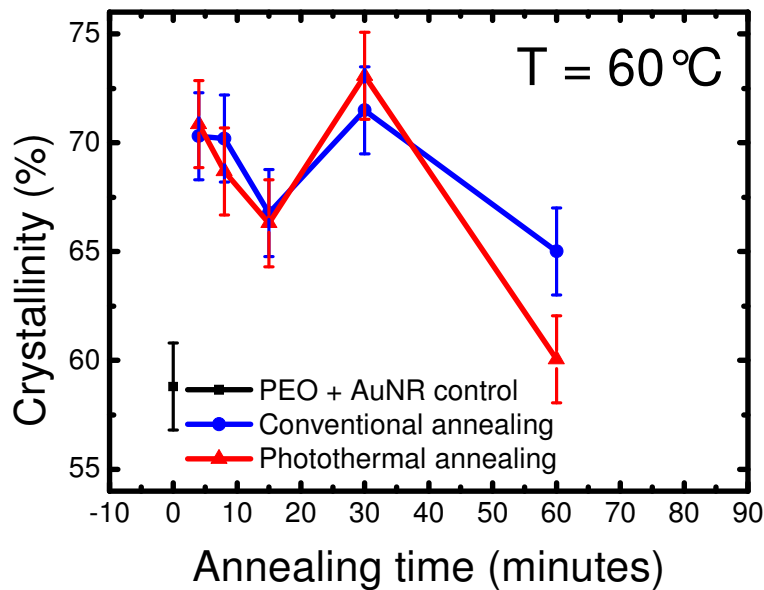


Figure 6. 9. Crystallinity as a function of annealing duration for AuNR:PEO nanofibers post-processed via conventional and photothermal heating at 60 °C..

Figure 6.9 shows the effect of post processing annealing on AuNR:PEO nanofibers at 60 °C on overall fiber crystallinity. While untreated nanofibers were found to have total crystallinity of ~59%, annealing was found to increase the crystallinity, with distinct time dependence. Both, conventional and photothermal heated samples demonstrated a sharp

increase in total crystallinity to ~70 % on annealing for 4-15 minutes. This can be attributed to the crystallization of lamellae present within the nanofibers. As previously discussed in literature pertaining to annealing of electrospun nanofibers,⁸⁴ annealing increases the size of the crystallites and causes the merging of larger crystallites. Significant reductions in fiber diameters observed in this study are in accordance with hypotheses from other studies that annealing caused the amorphous chains to rearrange and form more closely packed crystallites. Subsequently, longer annealing times (60 minutes) were found to reduce crystallinity in both conventional as well as photothermally annealed systems. While it can be observed that the crystallinities attained in photothermal annealing are similar to those obtained by conventional annealing, the shorter annealing times to attain higher crystallinities for photothermal annealing (as seen in our previous studies in nanoparticle containing electrospun fibers) has not been observed. This can be attributed to a lower barrier for crystallization during annealing for the nanorod nanofiber samples (as was seen for the nanorod film samples). Therefore, at higher temperatures, conventional annealing is just as effective as the photothermal annealing process. We postulate that the advantages of the photothermal annealing method will be realized at much lower temperatures (like 40 °C) as was seen in the nanorod film samples.

CHAPTER 7 : CONCLUSIONS AND RECOMMENDATIONS FOR FUTURE WORK

Chapter 7: Conclusions and future work

7. 1: Conclusions:

In the current work, a simple yet effective post processing thermal annealing technique to anneal polymer nanocomposite modalities has been presented. Clearly, gold nanoparticles can be made to act as localized heat sources within polymeric materials (both films as well as nanofibers) to manipulate crystallinity by using the photothermal effect that converts visible light into heat. The comparison of conventional annealing to photothermal annealing has proved to be an interesting test bed to test the efficacy of this approach. While annealing at same average temperature, a much faster increase in crystallinity is observed in systems annealed by photothermal annealing as against those annealed conventionally. This is of special significance at lower temperatures, where the time to reach maximum crystallinity in polymeric films is much lesser than those annealed conventionally. On the other hand, at temperatures closer to the melt temperatures, effects equivalent to heating the sample at much higher temperatures has been achieved without causing bulk melting of the sample.

Clearly, the presence of a heterogeneous temperature distribution in photothermal heating which produces higher temperature dynamics within the sample (which helps to grow and perfect polymer crystals) without global melting (which would occur if the entire sample experienced this temperature in conventional annealing) been demonstrated. The effective dynamic temperature experienced by the samples, arrived at by using time temperature superposition, can be significantly higher than the melting point, thereby aiding faster thermal response at even relatively lower annealing temperatures.

In case of nanofibrous systems, higher values of maximum crystallinity percentages have been achieved and in a much lesser time by photothermal annealing that clearly could not be achieved by conventional annealing. It is important to note that while achieving these elevated crystallinities, the complex nanostructured morphology of the nanofibrous mat has been maintained. Evaluation of mechanical properties of annealed samples also showed that samples annealed by photothermal heating possessed higher moduli than those annealed conventionally, clearly indicating the efficacy of photothermal annealing in improving crystal structure (crystallinity) and inter fiber bonding.

Study of the photothermal effect of nanorods in different polymeric media (fibers and films) reveals that the nanorods act as efficient heat sources when used for photothermal annealing at lower temperatures as compared to higher temperatures where they mimic conventional annealing. Higher crystallinity values and larger spherulitic structures obtained by photothermal annealing at 40 C (almost 25 C below the melt) as compared to conventional annealed samples, unequivocally demonstrates the presence of a heterogeneous temperature distribution which aids crystal perfection and growth.

7. 2 Recommendations for future work:

This study on the usage of gold nanoparticles as effective heat sources within a polymer system presents unique advantages to process polymers by thermal activation and in situ polymer processing. Not only can structures be modified by usage of post processing annealing, unique morphologies can be obtained. Listed below are a few recommendations for future work that can be carried out based on the results obtained from this given study:

- **High strength uniaxially aligned ultrafine fibers:**

Unique properties can be obtained by placement of nanoparticles in spatially isolated sections of a polymeric structure. For example, core-shell filaments can be made with the usage of a gold nanoparticle in the core of a core-sheath morphology microfiber filament, with the sheath being a water soluble polymer. Since the gold nanoparticles can be activated optically, the selective annealing of the core would impart higher moduli and strength to the filament due to cross linking. The sheath can then be later dissolved with a water jet post treatment to produce ultra strong low diameter filaments/microfibers for applications like filtration etc.

- **Thermally responsive shape memory meshes/stents**

Shape memory polymers (SMPs) are smart materials that can remember a primary shape and can return to this primary shape from a deformed secondary shape when given an appropriate stimulus. When heat is used as a stimulus to activate the shape memory effect (SME), the class of polymeric materials is referred to as thermally activated shape memory polymers. By usage of gold nanoparticles in a shape memory polymer based composite (example melt pressed film) the shape memory film can be made to harden/change shape in situ after incorporation into wound site, using the SPR (Surface Plasmon Resonance) properties of the AuNP (the heat generated can thermally activate the shape memory polymer). This can be used for a variety of application, right from internal wound closure to controlled drug delivery.

REFERENCES

1. Maity, S.; Downen, L. N.; Bochinski, J. R.; Clarke, L. I. *Polymer* **2011**, *7*, 1674-1685.
2. Link, S.; El-Sayed, M. A. *International Reviews in Physical Chemistry* **2000**, *3*, 409-453.
3. Koerner, H.; Price, G.; Pearce, N. A.; Alexander, M.; Vaia, R. A. *Nature Materials* **2004**, *2*, 115-120.
4. Zhang, H.; Xia, H.; Zhao, Y. *Journal of Materials Chemistry* **2012**, *3*, 845-849.
5. Hribar, K. C.; Metter, R. B.; Ifkovits, J. L.; Troxler, T.; Burdick, J. A. *Small* **2009**, *16*, 1830-1834.
6. Xu, H.; Xu, J.; Jiang, X.; Zhu, Z.; Rao, J.; Yin, J.; Wu, T.; Liu, H.; Liu, S. *Chemistry of Materials* **2007**, *10*, 2489-2494.
7. Delhalle, J.; Riga, J.; Denis, J. P.; Deleuze, M.; Dosière, M. *Chemical Physics Letters* **1993**, *1-3*, 21-24.
8. Odian, g. *Principles of Polymerization*; John Wiley and Sons: 2004; .
9. Yoon, D. Y.; Flory, P. J. *Polymer* **1977**, *5*, 509-513.
10. Chan, C. M.; Li, L. *Intrinsic Molecular Mobility and Toughness of Polymers Ii* **2005**, 1-41.

11. Keith, H. D.; Padden, F. J.; Vadimsky, R. G. *Journal of Polymer Science Part A-2-Polymer Physics* **1966**.
12. Takayanagi, M.; Nitta, K. *Macromolecular Theory and Simulations* **1997**, *1*, 181-195.
13. Takayanagi, M.; Imada, K.; Kajiyama, T. *Journal of Polymer Science Part C: Polymer Symposia* **1967**, *1*, 263-281.
14. PETERLIN, A. *J. Mater. Sci.* **1971**, *6*, 490.
15. Breese, D. R.; Beaucage, G. *Current Opinion in Solid State & Materials Science* **2004**, *6*, 439-448.
16. Barham, P. J.; Arridge, R. G. C. *Journal of Polymer Science: Polymer Physics Edition* **1977**, *7*, 1177-1188.
17. Gibson, A. G.; Davies, G. R.; Ward, I. M. *Polymer* **1978**, *6*, 683-693.
18. Perkins, W. G.; Capiati, N. J.; Porter, R. S. *Polymer Engineering & Science* **1976**, *3*, 200-203.
19. Perego, G.; Cella, G. D.; Bastioli, C. *J Appl Polym Sci* **1996**, *1*, 37-43.
20. Cabradilla, K. E.; Zeronian, S. H. *J Appl Polym Sci* **1975**, *2*, 503-517.
21. Testa, G.; Sardella, A.; Rossi, E.; Bozzi, C.; Seves, A. *Acta Polymerica* **1994**, *1*, 47-49.

22. ZERONIAN, S.; KAWABATA, H.; ALGER, K. *Text. Res. J.* **1990**, 3, 179-183.
23. Gassan, J.; Bledzki, A. K. *J Appl Polym Sci* **1999**, 4, 623-629.
24. Kreze, T.; Malej, S. *Text. Res. J.* **2003**, 8, 675-684.
25. Krässig, H.; Schurz, J.; Steadman, R. G.; Schliefer, K.; Albrecht, W. Cellulose. In *Ullmann's Encyclopedia of Industrial Chemistry*; Wiley-VCH Verlag GmbH & Co. KGaA: 2000; .
26. Gupta, V. B. *J Appl Polym Sci* **2002**, 3, 586-609.
27. Joojode, A. Behavior and Properties of Self-nucleated poly (ethylene terephthalate) (PET). North Carolina State university, 2011.
28. Godshall, D. Investigations of structure-property relationships in semicrystalline thermoplastic polymer:blown polyethylene films and polyacrylonitrile copolymers, Virginia Polytechnic Institute, 2002.
29. Huang, J. .; Chu, P. P.; Chang, F. -. *Polymer* **2000**, 5, 1741-1748.
30. Heffelfinger, C. J.; Schmidt, P. G. *J Appl Polym Sci* **1965**, 8, 2661-2680.
31. Arvidson, S. Molecular Orientation and Fine Structure Development in Polymer Fiber Formation. North Carolina State University, 2011.
32. Young, R. J.; Eichhorn, S. J. *Polymer* **2007**, 1, 2-18.

33. Kip, B. J.; Van Eijk, M. C. P.; Meier, R. J. *Journal of Polymer Science Part B: Polymer Physics* **1991**, *1*, 99-108.
34. Nakamae, K.; Nishino, T.; Shimizu, Y.; Matsumoto, T. *Polym. J.* **1987**, *5*, 451-459.
35. Prasad, K.; Grubb, D. T. *Journal of Polymer Science Part B: Polymer Physics* **1990**, *12*, 2199-2212.
36. Zhang, H.; Shao, H.; Hu, X. *J Appl Polym Sci* **2006**, *3*, 1738-1743.
37. Hong, J. K.; Madihally, S. V. *Tissue Engineering Part B-Reviews* **2011**, *2*, 125-142.
38. Demir, M. M.; Yilgor, I.; Yilgor, E.; Erman, B. *Polymer* **2002**, *11*, 3303-3309.
39. Huang, Z.; Zhang, Y. -.; Kotaki, M.; Ramakrishna, S. *Composites Sci. Technol.* **2003**, *15*, 2223-2253.
40. Greiner, A.; Wendorff, J. *Angewandte Chemie International Edition* **2007**, *30*, 5670-5703.
41. Formhals, A. United States Patent , 1934.
42. Baumgart.PK *J. Colloid Interface Sci.* **1971**, *1*, 71-&.
43. Taylor, G. *Proceedings of the Royal Society of London Series A-Mathematical and Physical Sciences* **1969**, *1515*, 453-&.

44. Taylor, G. *Proceedings of the Royal Society of London Series A-Mathematical and Physical Sciences* **1964**, 1380, 383-+.
45. Reneker, D. H.; Yarin, A. L.; Zussman, E.; Xu, H. *Advances in Applied Mechanics, Vol 41* **2007**, 43-195.
46. Deitzel, J. M.; Kleinmeyer, J.; Harris, D.; Beck Tan, N. C. *Polymer* **2001**, 1, 261-272.
47. Theron, S. A.; Zussman, E.; Yarin, A. L. *Polymer* **2004**, 6, 2017-2030.
48. McKee, M. G.; Wilkes, G. L.; Colby, R. H.; Long, T. E. *Macromolecules* **2004**, 5, 1760-1767.
49. Jarusuwannapoom, T.; Hongroijanawiwat, W.; Jitjaicham, S.; Wannatong, L.; Nithitanakul, M.; Pattamaprom, C.; Koombhongse, P.; Rangkupan, R.; Supaphol, P. *European Polymer Journal* **2005**, 3, 409-421.
50. Li, D.; Xia, Y. *Adv Mater* **2004**, 14, 1151-1170.
51. Shin, Y. M.; Hohman, M. M.; Brenner, M. P.; Rutledge, G. C. *Polymer* **2001**, 25, 09955-09967.
52. D. Li, W. Wang and Y. Xia - *Nano Letters* , - 8, - 1167.
53. - Li, D.; Wang, Y.; Xia, Y. - *Advanced Materials* - **2004**, - 4, - 361-- 366.

54. Matthews, J. A.; Wnek, G. E.; Simpson, D. G.; Bowlin, G. L. *Biomacromolecules* **2002**, *2*, 232-238.
55. Bhattarai, N.; Edmondson, D.; Veiseh, O.; Matsen, F. A.; Zhang, M. *Biomaterials* **2005**, *31*, 6176-6184.
56. Sundaray, B.; Subramanian, V.; Natarajan, T. S.; Rong-Zheng Xiang, T. S.; Chia-Cheng Chang; Wun-Shain Fann *Appl. Phys. Lett.* **2004**, *7*, 1222-1224.
57. Dalton, P. D.; Klee, D.; Möller, M. *Polymer* **2005**, *3*, 611-614.
58. Zhang, Y.; Huang, Z.; Xu, X.; Lim, C.; Ramakrishna, S. *Chem. Mat.* **2004**, *18*, 3406-3409.
59. Sun, Z.; Zussman, E.; Yarin, A.; Wendorff, J.; Greiner, A. *Adv Mater* **2003**, *22*, 1929-+.
60. Bognitzki, M.; Hou, H. Q.; Ishaque, M.; Frese, T.; Hellwig, M.; Schwarte, C.; Schaper, A.; Wendorff, J. H.; Greiner, A. *Adv Mater* **2000**, *9*, 637-+.
61. Wei, M.; Lee, J.; Kang, B.; Mead, J. *Macromolecular Rapid Communications* **2005**, *14*, 1127-1132.
62. Xie, Y.; Qiao, Z.; Chen, M.; Liu, X.; Qian, Y. *Adv Mater* **1999**, *18*, 1512-1515.
63. Morales, A.; Lieber, C. *Science* **1998**, *5348*, 208-211.
64. Lauhon, L.; Gudixsen, M.; Wang, C.; Lieber, C. *Nature* **2002**, *6911*, 57-61.

65. Zhang, Y.; Suenaga, K.; Colliex, C.; Iijima, S. *Science* **1998**, 5379, 973-975.
66. Moghe, A. K.; Gupta, B. S. *Polymer Reviews* **2008**, 2, 353-377.
67. Wei, M.; Lee, J.; Kang, B. W.; Mead, J. *Macromolecular Rapid Communications* **2005**, 14, 1127-1132.
68. Li, D.; Xia, Y. N. *Nano Letters* **2004**, 5, 933-938.
69. Dror, Y.; Salalha, W.; Avrahami, R.; Zussman, E.; Yarin, A. L.; Dersch, R.; Greiner, A.; Wendorff, J. H. *Small* **2007**, 6, 1064-1073.
70. Jiang, H. L.; Hu, Y. Q.; Li, Y.; Zhao, P. C.; Zhu, K. J.; Chen, W. L. *J. Controlled Release* **2005**, 2-3, 237-243.
71. Li, D.; McCann, J. T.; Xia, Y. N. *Small* **2005**, 1, 83-86.
72. Kai, D.; Prabhakaran, M. P.; Jin, G.; Ramakrishna, S. *Journal of Biomedical Materials Research Part B: Applied Biomaterials* **2011**, 2, 379-386.
73. Torres, F. G.; Troncoso, O. P.; Grande, C. G.; Díaz, D. A. *Materials Science and Engineering: C* **2011**, 8, 1737-1740.
74. Bhang, S. H.; Jeong, S. I.; Lee, T.; Jun, I.; Lee, Y. B.; Kim, B.; Shin, H. *Macromolecular Bioscience* **2011**, n/a-n/a.

75. Martins, A.; Alves da Silva, M. L.; Faria, S.; Marques, A. P.; Reis, R. L.; Neves, N. M. *Macromolecular Bioscience* **2011**, *7*, 978-987.
76. Nangrejo, M.; Bragman, F.; Ahmad, Z.; Stride, E.; Edirisinghe, M. *Mater Lett* **2012**, , 482-485.
77. Seyednejad, H.; Ji, W.; Schuurman, W.; Dhert, W. J. A.; Malda, J.; Yang, F.; Jansen, J. A.; van Nostrum, C.; Vermonden, T.; Hennink, W. E. *Macromolecular Bioscience* **2011**, *12*, 1684-1692.
78. Thomopoulos, S.; Hattersley, G.; Rosen, V.; Mertens, M.; Galatz, L.; Williams, G. R.; Soslowky, L. J. *Journal of Orthopaedic Research* **2002**, *3*, 454-463.
79. Thomas, V.; Jose, M. V.; Chowdhury, S.; Sullivan, J. F.; Dean, D. R.; Vohra, Y. K. *Journal of Biomaterials Science -- Polymer Edition* **2006**, *9*, 969-984.
80. W E Teo and, S. R. *Nanotechnology* **2006**, *14*, R89.
81. Xu, C. Y.; Inai, R.; Kotaki, M.; Ramakrishna, S. *Biomaterials* **2004**, *5*, 877-886.
82. Sundararaghavan, H. G.; Burdick, J. A. *Biomacromolecules* **2011**, *6*, 2344-2350.
83. Yang, Y.; Li, X.; Cheng, L.; He, S.; Zou, J.; Chen, F.; Zhang, Z. *Acta Biomaterialia* **2011**, *6*, 2533-2543.
84. Lim, C. T.; Tan, E. P. S.; Ng, S. Y. *Appl. Phys. Lett.* **2008**, *14*, 141908.

85. Inai, R.; Kotaki, M.; Ramakrishna, S. *Nanotechnology* **2005**, *2*, 208-213.
86. Arinstein, A.; Burman, M.; Gendelman, O.; Zussman, E. *Nature Nanotechnology* **2007**, *1*, 59-62.
87. Zussman, E.; Burman, M.; Yarin, A. L.; Khalfin, R.; Cohen, Y. *Journal of Polymer Science Part B: Polymer Physics* **2006**, *10*, 1482-1489.
88. Liu, Y.; Cui, L.; Guan, F.; Gao, Y.; Hedin, N. E.; Zhu, L.; Fong, H. *Macromolecules* **2007**, *17*, 6283-6290.
89. Baji, A.; Mai, Y.; Wong, S.; Abtahi, M.; Chen, P. *Composites Sci. Technol.* **2010**, *5*, 703-718.
90. Wong, S.; Baji, A.; Leng, S. *Polymer* **2008**, *21*, 4713-4722.
91. Baji, A.; Mai, Y.; Wong, S.; Abtahi, M.; Du, X. *Composites Sci. Technol.* **2010**, *9*, 1401-1409.
92. Zong, X. H.; Kim, K.; Fang, D. F.; Ran, S. F.; Hsiao, B. S.; Chu, B. *Polymer* **2002**, *16*, 4403-4412.
93. Wu, X.; Dzenis, Y. A. *J. Appl. Phys.* **2007**, *4*, 044306.
94. Kongklang, T.; Tashiro, K.; Kotaki, M.; Chirachanchai, S. *J. Am. Chem. Soc.* **2008**, *46*, 15460-15466.

95. Yee, W. A.; Nguyen, A. C.; Lee, P. S.; Kotaki, M.; Liu, Y.; Tan, B. T.; Mhaisalkar, S.; Lu, X. *Polymer* **2008**, *19*, 4196-4203.
96. Huang, C.; Chen, S.; Reneker, D. ?.; Lai, C.; Hou, H. *Adv Mater* **2006**, *5*, 668-671.
97. Mathew, G.; Hong, J. P.; Rhee, J. M.; Lee, H. S.; Nah, C. *Polym. Test.* **2005**, *6*, 712-717.
98. Katta, P.; Alessandro, M.; Ramsier, R. D.; Chase, G. G. *Nano Letters* **2004**, *11*, 2215-2218.
99. Dersch, R.; Liu, T.; Schaper, A. K.; Greiner, A.; Wendorff, J. H. *Journal of Polymer Science Part A: Polymer Chemistry* **2003**, *4*, 545-553.
100. Ma, Z. W.; Kotaki, M.; Inai, R.; Ramakrishna, S. *Tissue Eng.* **2005**, *1-2*, 101-109.
101. Svoboda, P.; Zeng, C.; Wang, H.; Lee, L. J.; Tomasko, D. L. *J Appl Polym Sci* **2002**, *7*, 1562-1570.
102. Hosseiny, N. Morphology and properties of polymer/carbon nanotube nanocomposite foams prepared by supercritical carbondioxide, Florida State university College of Engineering, 2010.
103. Bai, J.; Li, Y.; Yang, S.; Du, J.; Wang, S.; Zheng, J.; Wang, Y.; Yang, Q.; Chen, X.; Jing, X. *Solid State Commun.* **2007**, *5*, 292-295.

104. Yang, Q. B.; Li, D. M.; Hong, Y. L.; Li, Z. Y.; Wang, C.; Qiu, S. L.; Wei, Y. *Synth. Met.* **2003**, 1–3, 973-974.
105. He, C.; Gong, J. *Polym. Degrad. Stab.* **2003**, 1, 117-124.
106. http://www.iccmcentral.org/Proceedings/ICCM16proceedings/contents/pdf/FriA/FrAM1-05ge_yangh224650p.pdf.
107. Lee, J.; Isobe, T.; Senna, M. *J. Colloid Interface Sci.* **1996**, 2, 490-494.
108. Ioannis S., *C. J. Mater. Process. Technol.* **2005**, 2–3, 283-293.
109. Yarin, A. L.; Koombhongse, S.; Reneker, D. H. *J. Appl. Phys.* **2001**, 9, 4836-4846.
110. Rutherglen, C.; Burke, P. *Nano Letters* **2007**, 11, 3296-3299.
111. Dettlaff-Weglikowska, U.; Yoshida, J.; Sato, N.; Roth, S. *J. Electrochem. Soc.* **2011**, 2, A174-A179.
112. Ko, F.; Gogotsi, Y.; Ali, A.; Naguib, N.; Ye, H.; Yang, G. L.; Li, C.; Willis, P. *Adv Mater* **2003**, 14, 1161-1165.
113. Ji, X. L.; Hampsey, J. E.; Hu, Q. Y.; He, J. B.; Yang, Z. Z.; Lu, Y. F. *Chemistry of Materials* **2003**, 19, 3656-3662.
114. Rong, J.; Yang, Z. *Macromolecular Materials and Engineering* **2002**, 1, 11-15.

115. Li, Y.; Yu, J.; Guo, Z. *J Appl Polym Sci* **2002**, *4*, 827-834.
116. Ou, Y.; Yang, F.; Yu, Z. *Journal of Polymer Science Part B: Polymer Physics* **1998**, *5*, 789-795.
117. Cole, K. C.; Denault, J.; Bureau, M. N. *Macromolecular Symposia* **2004**, *1*, 47-60.
118. Jeon, S. J.; Lee, J. J.; Kim, W.; Chang, T. S.; Koo, S. M. *Thin Solid Films* **2008**, *12*, 3904-3909.
119. Trapalis, C. C.; Keivanidis, P.; Kordas, G.; Zaharescu, M.; Crisan, M.; Szatvanyi, A.; Gartner, M. *Thin Solid Films* **2003**, *1-2*, 186-190.
120. Qi, L. M.; Colfen, H.; Antonietti, M. *Nano Letters* **2001**, *2*, 61-65.
121. Murray, C. B.; Kagan, C. R.; Bawendi, M. G. *Annual Review of Materials Science* **2000**, 545-610.
122. Venta, J.; Pucci, A.; FernándezPinel, E.; García, M. .; Julián Fernandez, C.; Crespo, P.; Mazzoldi, P.; Ruggeri, G.; Hernando, A. *Adv Mater* **2007**, *6*, 875-877.
123. Duca, M.; Cucarella, M. O.; Rodriguez, P.; Koper, M. T. M. *J. Am. Chem. Soc.* **2010**, *51*, 18042-18044.
124. Crosby, A. J.; Lee, J. *Polymer Reviews* **2007**, *2*, 217-229.

125. Kim, G. -.; Lee, D. -.; Hoffmann, B.; Kressler, J.; Stöppelmann, G. *Polymer* **2001**, *3*, 1095-1100.
126. Creasy, T. S.; Kang, Y. S. *J. Thermoplast. Compos. Mater.* **2004**, *3*, 205-227.
127. Kim, G. M.; Lach, R.; Michler, G. H.; Potschke, P.; Albrecht, K. *Nanotechnology* **2006**, *4*, 963-972.
128. He, G.; Ginzburg, V. V.; Balazs, A. C. *Journal of Polymer Science Part B-Polymer Physics* **2006**, *17*, 2389-2403.
129. Lee, J.; Zhang, Q.; Emrick, T.; Crosby, A. J. *Macromolecules* **2006**, *21*, 7392-7396.
130. Jones, R. *Soft Condensed Matter*; Oxford University Press: New York, 2002; .
131. Naebe, M.; Lin, T.; Staiger, M. P.; Dai, L.; Wang, X. *Nanotechnology* **2008**, *30*, 305702.
132. Naebe, M.; Lin, T.; Tian, W.; Dai, L.; Wang, X. *Nanotechnology* **2007**, *22*, 225605.
133. Naebe, M. Carbon Nanotubes Reinforced Electrospun Polymer Nanofibres. In *Nanofibers*; Ashok Kumar, Ed.; Croatia, 2010; pp 310.
134. Saeed, K.; Park, S. *J Appl Polym Sci* **2007**, *6*, 3729-3735.
135. Sengupta, R.; Ganguly, A.; Sabharwal, S.; Chaki, T. K.; Bhowmick, A. K. *J. Mater. Sci.* **2007**, *3*, 923-934.

136. Ryan, K. P.; Cadek, M.; Nicolosi, V.; Blond, D.; Ruether, M.; Armstrong, G.; Swan, H.; Fonseca, A.; Nagy, J. B.; Maser, W. K.; Blau, W. J.; Coleman, J. N. *Composites Sci. Technol.* **2007**, 7–8, 1640-1649.
137. Keren, K.; Berman, R. S.; Buchstab, E.; Sivan, U.; Braun, E. *Science* **2003**, 5649, 1380-1382.
138. Barraza, H. J.; Pompeo, F.; O'Rear, E. A.; Resasco, D. E. *Nano Letters* **2002**, 8, 797-802.
139. Paul, D. R.; Robeson, L. M. *Polymer* **2008**, 15, 3187-3204.
140. Bilotti, E.; Fischer, H. R.; Peijs, T. *J Appl Polym Sci* **2008**, 2, 1116-1123.
141. Xu, D.; Wang, Z. *Polymer* **2008**, 1, 330-338.
142. Petrovi?, Z. S.; Javni, I.; Waddon, A.; Bánhegyi, G. *J Appl Polym Sci* **2000**, 2, 133-151.
143. Bhimaraj, P.; Yang, H.; Siegel, R. W.; Schadler, L. S. *J Appl Polym Sci* **2007**, 6, 4233-4240.
144. Yang, H.; Bhimaraj, P.; Yang, L.; Siegel, R. W.; Schadler, L. S. *Journal of Polymer Science Part B-Polymer Physics* **2007**, 7, 747-757.
145. Zheng, J.; Siegel, R. W.; Toney, C. G. *Journal of Polymer Science Part B: Polymer Physics* **2003**, 10, 1033-1050.

146. Liu, X.; Wu, Q.; Zhang, Q.; Mo, Z. *Journal of Polymer Science Part B: Polymer Physics* **2003**, *1*, 63-67.
147. Park, C.; Rosa, C. D.; Lotz, B.; Fetters, L. J.; Thomas, E. L. *Macromolecular Chemistry and Physics* **2003**, *12*, 1514-1523.
148. Vesely, D.; Ronca, G. *J. Microsc.* **2001**, *2*, 137-143.
149. Okamoto, M.; Shinoda, Y.; Okuyama, T.; Yamaguchi, A.; Sekura, T. *J. Mater. Sci. Lett.* **1996**, *13*, 1178-1179.
150. Wan, T.; Chen, L.; Chua, Y. C.; Lu, X. *J Appl Polym Sci* **2004**, *4*, 1381-1388.
151. S.C., T. *Materials Science and Engineering: R: Reports* **2006**, *3-4*, 73-197.
152. Thostenson, E. T.; Ren, Z. F.; Chou, T. W. *Composites Sci. Technol.* **2001**, *13*, 1899-1912.
153. Gojny, F. H.; Nastalczyk, J.; Roslaniec, Z.; Schulte, K. *Chemical Physics Letters* **2003**, *5-6*, 820-824.
154. McCullen, S. D.; Stano, K. L.; Stevens, D. R.; Roberts, W. A.; Monteiro-Riviere, N. A.; Clarke, L. I.; Gorga, R. E. *J Appl Polym Sci* **2007**, *3*, 1668-1678.
155. McCullen, S. D.; Stevens, D. R.; Roberts, W. A.; Ojha, S. S.; Clarke, L. I.; Gorga, R. E. *Macromolecules* **2007**, *4*, 997-1003.

156. Bao, J. Effect of Annealing on Mechanical and Electrical Properties for Electrospun Polyethylene Oxide Web Incorporated with Multiwall Carbon Nanotubes. NCSU, 2011.
157. Akita, H.; Hattori, T. *Journal of Polymer Science Part B: Polymer Physics* **1999**, 3, 189-197.
158. Zavyalov, S. A.; Pivkina, A. N.; Schoonman, J. *Solid State Ionics* **2002**, 3-4, 415-419.
159. Magaraphan, R.; Lilayuthalert, W.; Sirivat, A.; Schwank, J. W. *Composites Sci. Technol.* **2001**, 9, 1253-1264.
160. Xia, H. S.; Song, M. *Journal of Materials Chemistry* **2006**, 19, 1843-1851.
161. Pattanayak, A.; Jana, S. C. *Polymer* **2005**, 10, 3394-3406.
162. Knite, M.; Tupureina, V.; Fuith, A.; ZavickiS, J.; Teteris, V. *Materials Science & Engineering C-Biomimetic and Supramolecular Systems* **2007**, 5-8, 1125-1128.
163. Grady, B. P.; Pompeo, F.; Shambaugh, R. L.; Resasco, D. E. *J Phys Chem B* **2002**, 23, 5852-5858.
164. Statton, W.; Geil, P. *J Appl Polym Sci* **1960**, 9, 357-361.
165. Nakagawa, K.; Ishida, Y. *Journal of Polymer Science: Polymer Physics Edition* **1973**, 11, 2153-2171.
166. Zia, Q.; Ingolic, E.; Androsch, R. *Colloid Polym. Sci.* **2010**, 7, 819-825.

167. Kawai, T. *Kolloid-Zeitschrift und Zeitschrift für Polymere* **1965**, 2, 104-111.
168. Cheng, S. Z.; Zhang, A.; Barley, J. S.; Chen, J.; Habenschuss, A.; Zschack, P. R. *Macromolecules* **1991**, 13, 3937-3944.
169. Cheng, S. Z.; Barley, J. S.; Giusti, P. A. *Polymer* **1990**, 5, 845-849.
170. Price, F. P.; Kilb, R. W. *Journal of Polymer Science* **1962**, 165, 395-403.
171. Chen, E.; Jing, A. J.; Weng, X.; Huang, P.; Lee, S.; Cheng, S. Z.; Hsiao, B. S.; Yeh, F. *Polymer* **2003**, 19, 6051-6058.
172. Massa, M. V.; Dalnoki-Veress, K.; Forrest, J. *The European Physical Journal E* **2003**, 2, 191-198.
173. Murthy, N. S.; Bray, R. G.; Correale, S. T.; Moore, R. A. F. *Polymer* **1995**, 20, 3863-3873.
174. Gupta, V. B.; Kumar, S. *J Appl Polym Sci* **1981**, 6, 1897-1905.
175. Gupta, V. B.; Kumar, S. *J Appl Polym Sci* **1981**, 6, 1865-1876.
176. Choi, S.; Lee, S.; Joo, C.; Im, S.; Kim, S. *J. Mater. Sci.* **2004**, 4, 1511-1513.
177. Mikos, A.; Bao, Y.; Cima, L.; Ingber, D.; Vacanti, J.; Langer, R. *J. Biomed. Mater. Res.* **1993**, 2, 183-189.

178. You, Y.; Lee, S.; Lee, S.; Park, W. *Mater Lett* **2006**, *11*, 1331-1333.
179. BABATOPE, B.; ISAAC, D. *Polymer* **1992**, *8*, 1664-1668.
180. Tan, E.; Lim, C. *Nanotechnology* **2006**, *10*, 2649-2654.
181. Zong, X.; Ran, S.; Fang, D.; Hsiao, B.; Chu, B. *Polymer* **2003**, *17*, 4959-4967.
182. Deitzel, J. M.; Kleinmeyer, J. D.; Hirvonen, J. K.; Beck Tan, N. C. *Polymer* **2001**, *19*, 8163-8170.
183. Ravandi, S. A. H.; Sadrjahani, M. *J Appl Polym Sci* **2011**.
184. Fennessey, S. F.; Farris, R. J. *Polymer* **2004**, *12*, 4217-4225.
185. Zussman, E.; Chen, X.; Ding, W.; Calabri, L.; Dikin, D. A.; Quintana, J. P.; Ruoff, R. S. *Carbon* **2005**, *10*, 2175-2185.
186. Choi, S.; Lee, Y. S.; Joo, C. W.; Lee, S. G.; Park, J. K.; Han, K. *Electrochim. Acta* **2004**, *2-3*, 339-343.
187. Lee, S. J.; Oh, S. H.; Liu, J.; Soker, S.; Atala, A.; Yoo, J. J. *Biomaterials* **2008**, *10*, 1422-1430.
188. Ramaswamy, S.; Clarke, L. I.; Gorga, R. E. *Polymer* **2011**, *14*, 3183-3189.

189. Kelil, S *Nanophotonics for 21st century: From fabrication to application*, Addis Ababa University, June 2010.
190. Novotny, L. **Near-Field optical excitation and detection of surface plasmons**. *Springer Series in Optical Sciences*; 2007; pp 139-153.
191. Karpinski, P.; Miniewicz, A. *Plasmonics* **2011**, 3, 541-546.
192. Takahara, J.; Yamagishi, S.; Taki, H.; Morimoto, A.; Kobayashi, T. *Opt. Lett.* **1997**, 7, 475-477.
193. Haes, A. J.; Hall, W. P.; Chang, L.; Klein, W. L.; Van Duyne, R. P. *Nano Letters* **2004**, 6, 1029-1034.
194. Nikolajsen, T.; Leosson, K.; Bozhevolnyi, S. I. *Appl. Phys. Lett.* **2004**, 24, 5833-5835.
195. Zia, R.; Schuller, J. A.; Chandran, A.; Brongersma, M. L. *Materials Today* **2006**, 7-8, 20-27.
196. <http://blogs.nature.com> .
197. Perner, M.; Bost, P.; Lemmer, U.; vonPlessen, G.; Feldmann, J.; Becker, U.; Mennig, M.; Schmitt, M.; Schmidt, H. *Phys. Rev. Lett.* **1997**, 11, 2192-2195.
198. Link, S.; El-Sayed, M. A. *J Phys Chem B* **1999**, 21, 4212-4217.

199. Hu, M.; Chen, J.; Li, Z.; Au, L.; Hartland, G. V.; Li, X.; Marquez, M.; Xia, Y. *Chem. Soc. Rev.* **2006**, *11*, 1084-1094.
200. Huang, X.; Jain, P. K.; El-Sayed, I. H.; El-Sayed, M. A. *Lasers in Medical Science* **2008**, *3*, 217-228.
201. Baffou, G.; Quidant, R.; Girard, C. *Appl. Phys. Lett.* **2009**, *15*, 153109.
202. Baffou, G.; Quidant, R.; Javier Garcia de Abajo, F. *Acs Nano* **2010**, *2*, 709-716.
203. Jain, P. K.; Huang, X.; El-Sayed, I. H.; El-Sayed, M. A. *Plasmonics* **2007**, *3*, 107-118.
204. Jain, P. K.; Huang, X.; El-Sayed, I. H.; El-Sayed, M. A. *Acc. Chem. Res.* **2008**, *12*, 1578-1586.
205. Storhoff, J. J.; Elghanian, R.; Mucic, R. C.; Mirkin, C. A.; Letsinger, R. L. *J. Am. Chem. Soc.* **1998**, *9*, 1959-1964.
206. Nath, N.; Chilkoti, A. *Anal. Chem.* **2002**, *3*, 504-509.
207. Huang, X. H.; El-Sayed, I. H.; Qian, W.; El-Sayed, M. A. *J. Am. Chem. Soc.* **2006**, *6*, 2115-2120.
208. Takahashi, H.; Niidome, T.; Nariai, A.; Niidome, Y.; Yamada, S. *Nanotechnology* **2006**, *17*, 4431-4435.

209. Chen, J. Y.; Wiley, B.; Li, Z. Y.; Campbell, D.; Saeki, F.; Cang, H.; Au, L.; Lee, J.; Li, X. D.; Xia, Y. N. *Adv Mater* **2005**, *18*, 2255-2261.
210. Svaasand, L. O.; Gomer, C. J.; Morinelli, E. *Lasers in Medical Science* **1990**, *2*, 121-128.
211. Richardson, H. H.; Thomas, A. C.; Carlson, M. T.; Kordesch, M. E.; Govorov, A. O. *J Electron Mater* **2007**, *12*, 1587-1593.
212. Sershen, S. R.; Westcott, S. L.; Halas, N. J.; West, J. L. *J. Biomed. Mater. Res.* **2000**, *3*, 293-298.
213. Radt, B.; Smith, T. ?.; Caruso, F. *Adv Mater* **2004**, *23-24*, 2184-2189.
214. Skirtach, A. G.; Antipov, A. A.; Shchukin, D. G.; Sukhorukov, G. B. *Langmuir* **2004**, *17*, 6988-6992.
215. Srivastava, S.; Haridas, M.; Basu, J. *Bull. Mater. Sci.* **2008**, *3*, 213-217.
216. Cong, H.; Radosz, M.; Towler, B. F.; Shen, Y. *Separation and Purification Technology* **2007**, *3*, 281-291.
217. Roy, M.; Nelson, J.; MacCrone, R.; Schadler, L.; Reed, C.; Keefe, R. *Dielectrics and Electrical Insulation, IEEE Transactions on* **2005**, *4*, 629-643.
218. Liu, J.; Guo, T.; Yang, Y. *J. Appl. Phys.* **2002**, *3*, 1595-1600.

219. Sershen, S. R.; Westcott, S. L.; Halas, N. J.; West, J. L. *J. Biomed. Mater. Res.* **2000**, *3*, 293-298.
220. Alsawafta, M.; Badilescu, S.; Paneri, A.; Truong, V.; Packirisamy, M. *Polymers* **2011**, *4*, 1833-1848.
221. Armentano, I.; Marinucci, L.; Dottori, M.; Balloni, S.; Fortunati, E.; Pennacchi, M.; Becchetti, E.; Locci, P.; Kenny, J. *Journal of Biomaterials Science, Polymer Edition* **2011**, *4-6*, 541-556.
222. Li, J.; Claude, J.; Norena-Franco, L. E.; Seok, S. I.; Wang, Q. *Chemistry of Materials* **2008**, *20*, 6304-6306.
223. Li, R.; Yao, D. *J Appl Polym Sci* **2008**, *5*, 2909-2916.
224. Buchner, S.; Wiswe, D.; Zachmann, H. G. *Polymer* **1989**, *3*, 480-488.
225. Jain, P. K.; Lee, K. S.; El-Sayed, I. H.; El-Sayed, M. A. *The Journal of Physical Chemistry B* **2006**, *14*, 7238-7248.
226. Wu, X.; Ming, T.; Wang, X.; Wang, P.; Wang, J.; Chen, J. *ACS nano* **2009**, *1*, 113-120.
227. Zhao, J.; Zhang, X.; Yonzon, C. R.; Haes, A. J.; Van Duyne, R. P. **2006**.
228. Wybourne, M.; Hutchison, J.; Clarke, L.; Brown, L.; Mooster, J. *Microelectronic engineering* **1999**, *1*, 55-57.

229. Wybourne, M. N.; Clarke, L.; Yan, M.; Cai, S. X.; Brown, L. O.; Hutchison, J.; Keana, J. F. *Japanese journal of applied physics* **1997**, part 1, 7796-7800.
230. Clarke, L.; Wybourne, M.; Yan, M.; Cai, S.; Brown, L.; Hutchison, J.; Keana, J. *Journal of Vacuum Science & Technology B: Microelectronics and Nanometer Structures* **1997**, 6, 2925-2929.
231. Berven, C.; Wybourne, M.; Clarke, L.; Longstreth, L.; Hutchison, J.; Mooster, J. J. *Appl. Phys.* **2002**, 8, 4513-4517.
232. Maier, S. A.; Atwater, H. A. *J. Appl. Phys.* **2005**, 1, 011101-011101-10.
233. Link, S.; El-Sayed, M. A. *International Reviews in Physical Chemistry* **2000**, 3, 409-453.
234. Rashidi-Huyeh, M.; Palpant, B. *J. Appl. Phys.* **2004**, 8, 4475-4482.
235. Liu, C.; Li, B. Q.; Mi, C. C. *NanoBioscience, IEEE Transactions on* **2009**, 3, 271-280.
236. S. Maity; Wei-Chen Wu; J. B. Tracy; J. R. Bochinski and L. I. Clarke *Phys Rev B, Rapid Comm* **2013**.
237. Link, S.; El-Sayed, M. *International Reviews in Physical Chemistry* **2000**, 3, 409-453.
238. Zharov, V.; Lapotko, D. *Ieee Journal of Selected Topics in Quantum Electronics* **2005**, 4, 733-751.

239. Boyer, D.; Tamarat, P.; Cognet, L.; Orrit, M.; Lounis, B. *Manipulation and Analysis of Biomolecules, Cells and Tissues* **2003**, 121-125.
240. Zharov, V.; Galitovsky, V.; Viegas, M. *Appl. Phys. Lett.* **2003**, 24, 4897-4899.
241. Boyer, D.; Tamarat, P.; Maali, A.; Lounis, B.; Orrit, M. *Science* **2002**, 5584, 1160-1163.
242. Lapotko, D. *Optics Express* **2009**, 4, 2538-2556.
243. Harris, N.; Ford, M.; Cortie, M. *J Phys Chem B* **2006**, 22, 10701-10707.
244. Sershen, S.; Westcott, S.; West, J.; Halas, N. *Applied Physics B* **2001**, 4, 379-381.
245. Takahashi, H.; Niidome, T.; Nariai, A.; Niidome, Y.; Yamada, S. *Chem. Lett.* **2006**, 5, 500-501.
246. Maity, S.; Downen, L. N.; Bochinski, J. R.; Clarke, L. I. *Polymer* **2011**, 7, 1674-1685.
247. Maity, S.; Bochinski, J. R.; Clarke, L. I. *Adv. Funct. Mater.* **2012**, 24, 5259-5270.
248. Maity, S.; Kozek, K. A.; Wu, W.; Tracy, J. B.; Bochinski, J. R.; Clarke, L. I. *Part. Part. Syst. Charact.* **2013**, 2, 193-202.
249. FRENS, G. *Nature-Physical Science* **1973**, 105, 20-22.
250. Bur, A. J.; Vangel, M. G.; Roth, S. *Appl. Spectrosc.* **2002**, 2, 174-181.

251. Strobl, G. R. *The physics of polymers: concepts for understanding their structures and behavior*; Springer: 2007; .
252. Chatterjee, A. M.; Price, F. P.; Newman, S. *Journal of Polymer Science: Polymer Physics Edition* **1975**, *12*, 2391-2400.
253. Stadlbauer, M.; Eder, G.; Janeschitz-Kriegl, H. *Polymer* **2001**, *8*, 3809-3816.
254. Tribout, C.; Monasse, B.; Haudin, J. *Colloid Polym. Sci.* **1996**, *3*, 197-208.
255. Wieczorek, W.; Such, K.; Florjanczyk, Z.; Stevens, J. *J. Phys. Chem.* **1994**, *27*, 6840-6850.
256. Kim, G.; Wutzler, A.; Radosch, H.; Michler, G. H.; Simon, P.; Sperling, R. A.; Parak, W. J. *Chemistry of materials* **2005**, *20*, 4949-4957.
257. Lin, H.; Freeman, B. D. *J. Membr. Sci.* **2004**, *1*, 105-117.
258. Coutts-Lendon, C.; Koenig, J. L. *Appl. Spectrosc.* **2005**, *8*, 976-985.
259. Roberts, R. *Polymer* **1969**, 117-125.
260. Yeh, G. S.; Hosemann, R.; Loboda-Čačković, J.; Čačković, H. *Polymer* **1976**, *4*, 309-318.
261. He, Y. Q.; Liu, S. P.; Kong, L.; Liu, Z. F. *Spectrochimica Acta Part A: Molecular and Biomolecular Spectroscopy* **2005**, *13*, 2861-2866.

262. Wang, H.; Keum, J. K.; Hiltner, A.; Baer, E.; Freeman, B.; Rozanski, A.; Galeski, A. *Science* **2009**, *5915*, 757-760.
263. Snétivy, D.; Vancso, G. J. *Polymer* **1992**, *2*, 432-433.
264. Sınmazçelik, T.; Yılmaz, T. *Mater Des* **2007**, *2*, 641-648.
265. Zhokhavets, U.; Erb, T.; Gobsch, G.; Al-Ibrahim, M.; Ambacher, O. *Chemical Physics Letters* **2006**, *4-6*, 347-350.
266. Painter, P. C.; Coleman, M. M. *Essentials of polymer science and engineering*; DEStech Publications, Inc: 2008; .
267. CHENG, S.; CHEN, J.; WU, S.; ZHANG, A.; YANDRASITS, M.; ZHUO, Q.; QUIRK, R. *Crystallization of Polymers* **1993**, 51-62.
268. Dreezen, G.; Koch, M. H. J.; Reynaers, H.; Groeninckx, G. *Polymer* **1999**, *23*, 6451-6463.
269. Pearce, R.; Vancso, G. *Macromolecules* **1997**, *19*, 5843-5848.
270. Liao, C.; Ye, W. *Electrochim. Acta* **2004**, *27*, 4993-4998.
271. Srithep, Y.; Nealey, P.; Turng, L. *Polym. Eng. Sci.* **2013**, *3*, 580-588.
272. Djokovic, V.; Dramicanin, M.; Kostoski, D.; Dudic, D. *Trends in Advanced Materials and Processes* **2000**, 195-200.

273. Saravanan, S.; Nethala, S.; Pattnaik, S.; Tripathi, A.; Moorthi, A.; Selvamurugan, N. *Int. J. Biol. Macromol.* **2011**, *2*, 188-193.
274. Sill, T. J.; von Recum, H. A. *Biomaterials* **2008**, *13*, 1989-2006.
275. Sawada, I.; Fachrul, R.; Ito, T.; Ohmukai, Y.; Maruyama, T.; Matsuyama, H. *J. Membr. Sci.* **2012**, 1-6.
276. Barhate, R.; Ramakrishna, S. *J. Membr. Sci.* **2007**, *1*, 1-8.
277. Thavasi, V.; Singh, G.; Ramakrishna, S. *Energy & Environmental Science* **2008**, *2*, 205-221.
278. Chen, X.; Xu, S.; Yao, N.; Shi, Y. *Nano letters* **2010**, *6*, 2133-2137.
279. Chen, C.; Wang, L.; Huang, Y. *Mater Lett* **2009**, *5*, 569-571.
280. Theron, J.; Knoetze, J.; Sanderson, R.; Hunter, R.; Mequanint, K.; Franz, T.; Zilla, P.; Bezuidenhout, D. *Acta Biomaterialia* **2010**, *7*, 2434-2447.
281. Viswanath V., Maity S., Bochinski J.R., Clarke L.I. and Gorga R.E. *Macromolecules* **2013**.
282. Barakat, N. A.; Woo, K.; Kanjwal, M. A.; Choi, K. E.; Khil, M. S.; Kim, H. Y. *Langmuir* **2008**, *20*, 11982-11987.

283. Wang, P.; Zhang, L.; Xia, Y.; Tong, L.; Xu, X.; Ying, Y. *Nano letters* **2012**, *6*, 3145-3150.
284. Seol, Y.; Carpenter, A. E.; Perkins, T. T. *Opt. Lett.* **2006**, *16*, 2429-2431.
285. Pustovalov, V.; Smetannikov, A.; Zharov, V. *Laser Physics Letters* **2008**, *11*, 775.
286. Bendix, P. M.; Reihani, S. N. S.; Oddershede, L. B. *ACS nano* **2010**, *4*, 2256-2262.
287. Maity, S.; Downen, L. N.; Bochinski, J. R.; Clarke, L. I. *Polymer* **2011**, *7*, 1674-1685.
288. Reneker, D. H.; Yarin, A. L.; Fong, H.; Koombhongse, S. *J. Appl. Phys.* **2000**, 4531.
289. Wu, H.; Wu, X.; Ge, M.; Zhang, G.; Wang, Y.; Jiang, J. *Composites Sci. Technol.* **2007**, *6*, 1116-1120.
290. Bortel, E.; Hodorowicz, S.; Lamot, R. *Die Makromolekulare Chemie* **1979**, *10*, 2491-2498.
291. Bai, H.; Deng, H.; Zhang, Q.; Wang, K.; Fu, Q.; Zhang, Z.; Men, Y. *Polym. Int.* **2012**, *2*, 252-258.
292. Nikoobakht, B.; El-Sayed, M. A. *Chemistry of Materials* **2003**, *10*, 1957-1962.
293. Gohil, R. M. *J Appl Polym Sci* **1993**, *9*, 1649-1664.
294. Park, S. D.; Todo, M.; Arakawa, K.; Koganemaru, M. *Polymer* **2006**, *4*, 1357-1363.